Study of early hydration mechanisms of cement by means of electron microscopy

PAR

Amélie BAZZONI

EPFL

ÉCOLE POLYTECHNIQUE
FÉDÉRALE DE LAUSANNE

Suisse
2014

Acknowledgements

I would like to express my gratitude to all the people who made this work possible:

- Prof. Karen Scrivener, my thesis director who gave me the opportunity to this work, for her guidance, and for the motivating and stimulating discussions. I also thank her for trusting me and giving me the opportunity to present my research in several international conferences.

- Dr Marco Cantoni, my thesis co-director, for his help, support and teaching for all the microscopy techniques.

- The members of my thesis Jury: Dr Paul Bowen, Dr Patrick Juilland and Dr Ellis Gartner for the time and effort they spent to read and review the thesis. Both the critical scrutiny and constructive advice are highly appreciated. I am also thankful to Dr Stefano Mischler who was the president of this Jury.

- Dr Cyrille Dunant for helping me with the numerical modeling. I also thank him fort the fruitful discussions and his corrections and advices for the writing of the manuscript.

- Dr Ruben Snellings for his contribution in the XRD analysis and the constructive discussions.

- Prof. Jorgen Skibsted, for acquiring the NMR spectra and for fruitful discussion of these results.

- Colette Vallotton, Danièle Laub and Fabienne Bobard for helping me with the TEM sample preparation.

- Vincent Fays, whose contribution as semester project can be found in this thesis.

- My colleges and friends from both laboratory LMC and CIME for the good atmosphere and great work. Special thank to John, Elise and Berta for all the interesting discussions about the C-S-H, to Quentin, Brian, Emad and Guillaume L. for the fun with the microscopes. I am grateful to Quentin, Pierre and Guillaume P. who I could rely on in any situation.

Acknowledgements

- My friends, for their encouragement and for always being there when I needed a break.

- My family, for always being there when I needed them, for trusting me to make my own decisions and for their unwavering support.

- Niels, for always being there, supporting me and encouraging me no matter what.

Abstract

Cementitious materials, typically OPC-based concrete, are the most used materials in the world. In this work, the hydration reaction of alite, the major component of ordinary Portland cement is studied. Despite much research vying to understand the mechanisms controlling the kinetics of hydration, controversies still remain regarding the limiting factors of the characteristic periods observed by calorimetry.

The mechanisms controlling the hydration reaction of alite are studied, benefiting from the latest development in microscopy techniques. Several alites with narrow particle size distributions and different chemical composition were synthesized in the laboratory. The samples underwent different treatments such as grinding and annealing and used in different mix preparations. Defect densities were investigated by TEM and correlated with the duration of the induction period. Morphological observations of the surface by means of high resolution SEM were carried out during the induction period and the acceleration period, to follow the nucleation and growth of C-S-H. STEM investigation of samples aged from few hours to one month allowed the characterization of growth modes of C-S-H. Further EDX, XRD and TGA analyses were used to characterize the hydrates content and chemical composition.

This work shows, first, that both changes in the defect density of alite in the saturation degree control the duration of the induction period, which confirms that the crystal dissolution theory recently applied to the alite dissolution explains the rapid slowdown in the hydration curve after the first dissolution. Second, C-S-H grows as needles outward from the anhydrous grains during the acceleration period. The slope of the acceleration period and height of the maximum heat are proportional to the number of C-S-H nuclei, ultimate length of the needles and availability and type of surface, demonstrating that the acceleration period is governed by the growth of C-S-H. The length of the needles is modified by the certain ions in the solution, such as zinc. At the maximum heat flow, the surfaces of the grains are completely covered by C-S-H and the lengthening of the needles slows drastically. At this stage, the formation of inner-product begins. This modification of the C-S-H growth mode leads to the deceleration period. Finally, it was shown that the chemical composition of C-S-H influences the thermo-dynamic equilibrium of the system.

Key words: Cement hydration, electron microscopy, SEM, TEM, C-S-H

Résumé

Les matériaux cimentaires, principalement le béton à base d'OPC, sont les matériaux les plus utilisés au monde. Cette thèse porte sur la réaction d'hydratation de l'alite, le constituant majeur du ciment Portland. Malgré de nombreuses recherches visant à comprendre les mécanismes contrôlant la cinétique de la réaction, il demeure toujours des controverses sur les facteurs limitants durant les périodes caractéristiques observées en calorimétrie.

Les mécanismes qui contrôlent la réaction d'hydratation de l'alite ont été étudiés au bénéfice des derniers développements en microscopie. Plusieurs alites ayant des distribution de tailles de particules réduites et de différentes compositions chimiques ont été synthétisées. Les échantillons ont subit différents traitements tels que le broyage ou le recuit et différentes préparations de mélange. La densité de défauts cristallins a été étudiée par MET et reliée à la durée de la période d'induction. La morphologie de la surface a été étudiée par MEB à haute résolution durant les périodes d'induction et d'accélération pour suivre la nucléation et la croissance du C-S-H. L'observation par MEBT d'échantillons ayant réagi durant des périodes variant de quelques heures à un mois, ont permis de caractériser la croissance du C-S-H. D'autres techniques telles que l'EDS, la DRX et l'ATG ont été utilisées pour déterminer le contenu en hydrates et leur composition.

Ce travail démontre premièrement que tant des changements de la densités de défauts dans l'alite que du degré de saturation contrôlent la durée de la période d'induction Ceci confirme la validité la théorie de la dissolution des cristaux pour expliquer le ralentissement de la réaction après la dissolution initiale. Deuxièmement, que le C-S-H croît sous forme d'aiguilles partant de la surface des grains durant la prériode d'accélération. La pente de la période d'accélération et la hauteur du pic principal de chaleur sont proportionnels au nombre de nucléus de C-S-H, la longueur finale de ses aiguilles et la disponibilité de surface : la période d'accélération est contrôlée par la croissance du C-S-H. La longueur des aiguilles est modifiée par certains ions en solution, tel que le zinc. Au pic de chaleur, la surface des grains est complètement recouverte de C-S-H et la croissance des aiguilles ralenti. A ce moment, la formation du produit intérieur du C-S-H commence. Cette modification du mode de croissance du C-S-H conduit à la période de décélération. Finalement, il a été observé que la composition chimique du C-S-H influence l'équilibre thermodynamique du système.

Mots clés : Hydratation du ciment, microscopie électronique, MEB, MET, C-S-H

Contents

Contents

List of Figures

List of Tables

Glossary

Abraviation	Definition
C	Calcium oxide CaO
S	Silicon dixide SiO_2
A	Aluminium oxide Al_2O_3
F	Iron oxide Fe_2O_3
H	Water H_2O
C_3S	Tricalcium silicate
C_2S	Dicalcium silicate
C_3A	Tricalcium aluminate
C_4AF	Calcium alumino-ferrite solid solution
OPC	Ordinary Portland cement
WPC	White Portland cement
L	Limestone
w/c - w/s	water to cement ratio - water to solid ratio
CH	Portlandite/ calcium hydroxide $Ca(OH)_2$
C-S-H	Calcium-silicate hydrates
Aft	Ettringite / trisulfoaluminate
Afm	Monsulfo aluminate
SEM	Scanning electron microscopy
SE	Secondary electrons
BSE	Backscaterred electrons
TEM	Transmission electron microscopy
STEM	Scanning transmission electron microscopy
EDS	Energy dispersive spectroscopy
XRD	X-ray diffraction
PSD	Particle size distribution
TGA	Thermogravimetric analysis
NMR	Nuclear magnetic raisonance

1 Introduction

Concrete is by far the most used material in the world (more than $1.5\,\text{m}^3$ being produced per person per year worldwide). Even if the associated specific CO_2 emissions are lower than alternative materials, they account for some 5-8 % of man-made CO_2 due to the huge volumes of cement produced. Furthermore, demand is forecast to double or treble by 2050, due to the growing world population and development. Improvements in sustainability must be made to reduce as much as possible the CO_2 emissions, while keeping buildings safe.

Concrete is a complex material, composed of cement, sand, aggregates and water. The hydration of cement gives rise to the properties of concrete, which are mostly understood on an empirical basis. Discovering fundamental mechanisms is a pre-requisite for the formulation of predictive models, which could then be used to design new materials reducing the need for time consuming empirical studies. It would further facilitates the development of low CO_2 binders.

Cement is made by heating limestone and clay at 1450°C. At this temperature, partial fusion occurs and nodules of clinker are produced[1]. Clinker is composed about 67% of CaO, 22% of SiO_2, 5% of Al_2O_3, 3% of Fe_2O_3 and 3% of other materials. It is important to emphasize that the cement chemistry has its own nomenclature. As cement is composed mainly of oxide materials, a letter stands for an oxide. For example, calcium oxide CaO is noted C, silicon dioxide SiO_2 is noted S and more complex oxides such as triclacium silicate Ca_3SiO_5 are noted C_3S. The oxides in clinker are distributed in four phases, 2 silicates: alite (impure C_3S) and belite (C_2S) and 2 aluminates: C_3A and C_4AF. The clinker is finely ground and mixed with gypsum (calcium sulfate) to produce the commonly known ordinary Portland cement (OPC).

The hydration of OPC is a complex reaction between clinker phases, calcium sulfate and water, resulting in the formation of hydrates and leading to setting and hardening[2]. The hydration of silicate phases leads to the formation of calcium silicate hydrate (C-S-H) and Portlandite or calcium hydroxide (CH) and the hydration of aluminate phases leads to the formation of ettringite or trisulfoaluminoferite hydrate (AFt) and monosulfoaluminoferite hydrate (AFm).

1

As the hydration reaction is exothermic, it can be followed by isothermal calorimetry. Figure 3.5 shows a typical calorimetry curve for the hydration of an OPC.
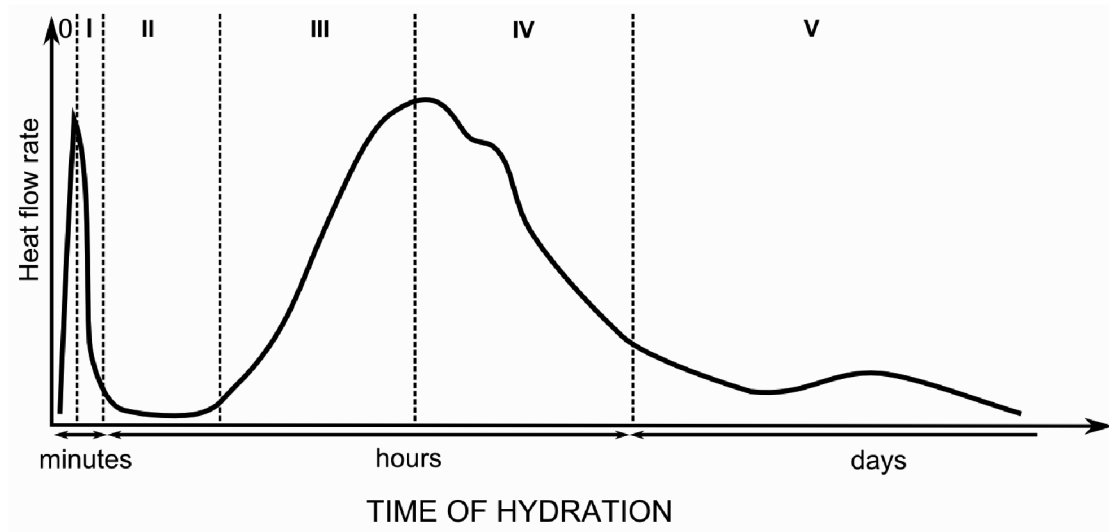
Figure 1.1: Schematic representation of a calorimetry curve of OPC.

At first (0), a fast dissolution of the anhydrous phases occurs. The presence of calcium sulfate controls the dissolution of C_3A and prevents setting[1]. Second, there is a sudden slowdown in the reaction (I), followed by a period of low chemical activity (II). Thirdly, there is the main hydration peak (III), resulting from the precipitation of C-S-H and CH, the hydration from C_3S and C_2S. After the main hydration peak there is a second deceleration (IV), where a second peak is observed, which corresponds to the rapid formation of ettringite, when all sulfates ions are consumed. Then, there is a period of low activity, where a third peak is observed (V), corresponding to the formation of Afm, which results from the reaction of ettringite with C_3A when gypsum is fully consumed[3].

Figure 1.2 shows a schematic representation of the microstructure development in OPC as proposed by Scrivener[4].
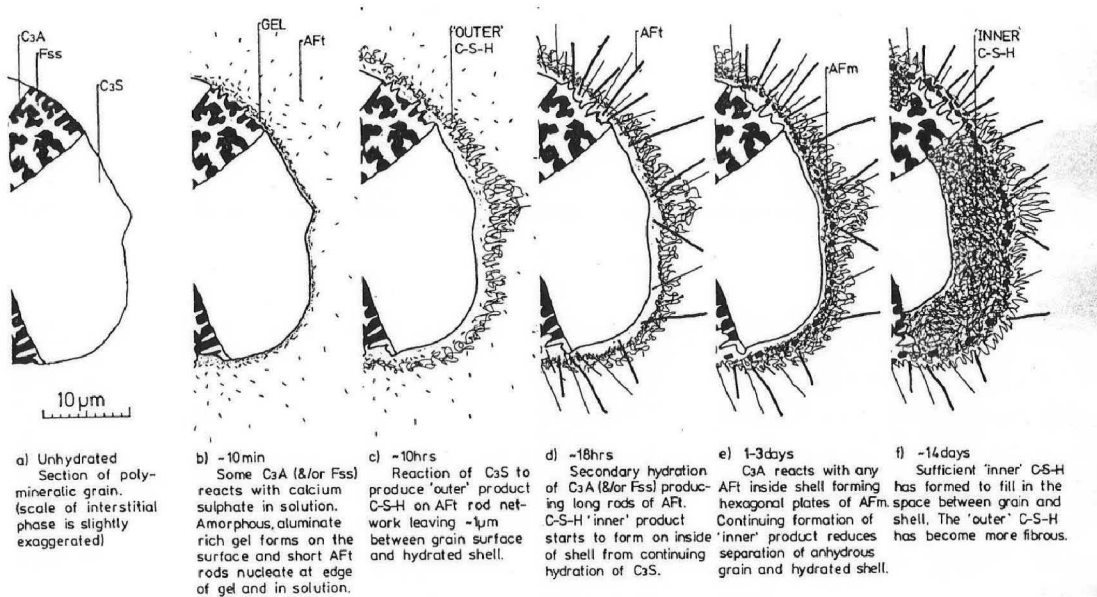
Figure 1.2: Schematic representation of the microstrucure devlopement of OPC, from Scrivener[4].

As tricalcium silicate is the most important constituent of OPC (50-70%), its hydration controls the kinetics at early age. Alite is an impure tricalcium silicate, which contains foreign ions such as aluminium, magnesium, iron, zinc or sodium. The hydration of alite consists of the reaction of C_3S with water resulting in the formation of calcium hydroxide (CH), also called Portlandite, and calcium silicate hydrates (C-S-H) with variable composition, according to the following equation 5.1:

$$C_3S + (3\text{-}x\text{-}n)H_2O \longrightarrow C_x\text{-}S\text{-}H_n + (3\text{-}x)CH \tag{1.1}$$

The heat evolution profile of C_3S hydration can be divided into 6 stages as proposed by Gartner et al.[2]. Each stage corresponds to a domain of time in the heat flow profile, and different phenomena govern the kinetics in each of these domains. The heat flow evolution compared to the calcium concentration in solution $[Ca^{2+}]$ with time is shown in Figure 1.3.

A general description of the mechanisms is presented in the next lines. Then, at the beginning of the chapters, a more detailed literature review about the individual periods is given.

Stage 0: The initial fast reaction: The first contact of the surface with water results in a fast release of ions in the solution. Ionic species such as Ca^{2+}, OH^-, $H_2SiO_4^{2-}$ pass rapidly into solution. The dissolution of C_3S is congruent and the reaction lasts only a few minutes.

3
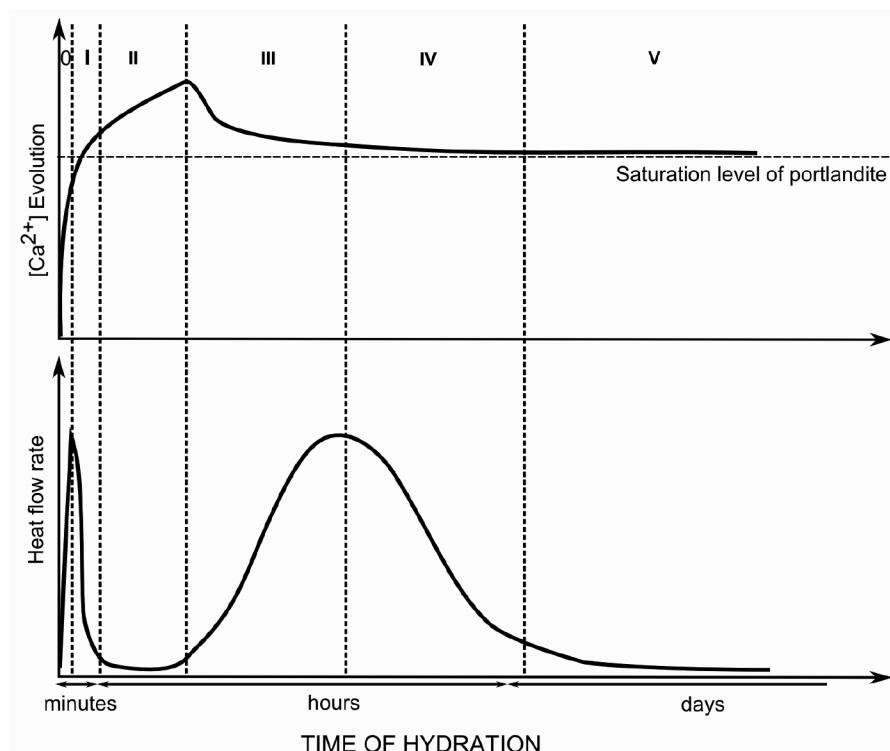
Figure 1.3: Solution phase analysis with the corresponding calorimetry curve, adapted from Gartner et al.[2].

Stage I and II: First deceleration and induction period: The transition from fast dissolution to slow dissolution[5]. The surface is altered in such a way that the dissolution rapidly slows down and progresses then very slowly. Concentration of calcium and silica in solution reach the critical solubility product to initiate nucleation of C-S-H. At the end of the induction period, the calcium ion concentration in solution exceeds the theoretical level of saturation for CH. Several theories have been proposed to explain the phenomena during these stages and is discussed in chapter 3.

Stage III: Acceleration period: When the calcium ion concentration reaches a maximum a massive precipitation of hydrates occurs. During this stage the hydrates growth controls the kinetics and the calcium ion concentration goes back to the saturation level. However, the mechanism of C-S-H growth is still not understood and again authors have proposed different theories and is further discussed in chapter 4.

Stage IV: Second deceleration period: The rate of reaction decreases again. The reason for this deceleration remains unclear and is further discussed in chapter 4.

Stage V: Slow reaction period: The reaction progresses very slowly resulting in the gradual densification of the microstructure.

1.1 Statement of the problem and objectives of the thesis

Several reviews on the early hydration kinetics have been published[6–9] demonstrating the importance the first 24 hours of hydration. However, the exact mechanisms governing the kinetics are still a subject of controversy. First, there are different theories in the literature trying to explain this rapid transition from a fast dissolution regime to a slow dissolution regime. Second, during the main hydration peak, the mechanisms that trigger the nucleation and growth of hydrates are debated and the growth modes of C-S-H is not well understood. The reason for the transition from the acceleration period to the deceleration is still not understood.

Despite considerable effort to develop theories to describe the different stages of hydration, none of them are fully accepted. Several studies in the literature show contradictory results. These unanswered questions are examined in the thesis:

- What is the distribution of defects in alite?

- What is the effect of a change in the defect density on the induction period?

- How does the surface of alite evolve during hydration?

- How do doping ions present as impurities in alite affect hydration?

- How is C-S-H growing?

- What is the hydrate distribution in space?

- What is causing the deceleration period?

- What is the effect of the dilution on the C-S-H growth and composition?

Benefiting from latest development in microscopy techniques, answers to these questions are tentatively given. Surface and sub-surfaces structures of anhydrous grains are studied by transmission electron microscopy. High resolution scanning electron microscopy is used to follow the evolution of the surface of the grains during the first hours. C-S-H growth, morphology and composition are characterized by scanning transmission electron microscopy coupled with energy dispersive spectroscopy. The evolution of the microstructure is compared with the hydration kinetics measured by isothermal calorimetry. Modifications of the microstructure is then correlated with changes in the calorimetry curves. Complementary analyses are done by X-Ray diffraction and thermogravimetric analysis to have the phases present and quantify the hydrates produced.

Numerical modeling is used, to support that C-S-H nucleation and growth is the rate-controlling parameter in the acceleration period of alite. Experimentally measured parameters of C-S-H nucleation and growth are used as inputs for μic hydration model.

1.2   Chapter overview

This thesis aims to better understand the mechanisms controlling the early hydration reaction of alite and is structured as follow:

Chapter 2 describes the different characterization methods and materials used in this study. A dedicated sample preparation for microscopy study adapted for cimentitious materials was developed during this work.

Chapter 3 focuses on the mechanisms and parameters controlling the induction period. The effects of grinding, annealing, water to cement ratio and doping ions in alite on the duration of the induction period are examined.

Chapter 4 is about the growth of hydrates during the main hydration peak. The effects of annealing, water to cement ratio, specific surface area, limestone and doping ions in alite on the growth rates and morphology of C-S-H are examined. These effects will be related the slope of the acceleration period and height of the maximum heat flow. The transition from the acceleration to deceleration period will be investigated. Furthermore, numerical modeling is done to correlate the experimental observations of C-S-H growth with the kinetics of the reaction.

Chapter 5 examines the evolution of the chemical composition and morphology of C-S-H and Portlandite content in pastes at later ages. Two systems with two different water to cement ratios and a third system a blend of C_3S with limestone is studied.

Chapter 6 gives the general conclusion of this research and the perspectives.

2 Materials and methods

In this chapter, first the different materials synthesis and preparation is described, then the methods used to characterize the materials.

Different samples of pure C_3S and alites were synthesized and other materials were provided. These materials were ground to different particles size distributions (PSD). Their chemical compositions were determined by X-Ray fluorescence (XRF) and their crystalline content by X-Ray diffraction (XRD). Hydration kinetics were followed by isothermal calorimetry of pastes and conductivity measurement of solutions. The microstructure development was studied by means of different electron microscopy techniques. These techniques includes scanning electron microscopy (SEM) and transmission electron microscopy (TEM). The sample preparation for this purpose was developed, to have images of hydrated samples at very early ages (from few hours to 28 days) and characterize their chemical composition.

2.1 Sample synthesis and preparation

In this study, pure tricalcium silicate (C_3S), different alites, clinker, cement and other materials are used. Before describing their protocols of preparation, the specificity of the crystal structure of tricalcium silicate is discussed.

Impure tricalcium silicate (C_3S) also called alite, is the major phase of ordinary Portland cement (OPC) and its hydration dominates the development of properties of OPC[1]. The most common impurities in alite are Na, Mg, Al, Fe, Zn, Cr[1]. When these ions are incorporated in C_3S, they can modify its crystalline structure. Pure tricalcium silicate (Ca_3SiO_5, C_3S) is known to undergo 7 polymorphic modifications between heating temperature and room temperature. These modifications are reported to occur following the sequence:

$$T_1 \xleftrightarrow{620\,°C} T_2 \xleftrightarrow{920\,°C} T_3 \xleftrightarrow{980\,°C} M_1 \xleftrightarrow{990\,°C} M_2 \xleftrightarrow{1060\,°C} M_3 \xleftrightarrow{1070\,°C} R$$
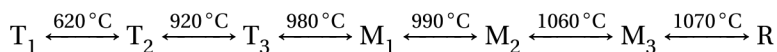
with T = triclinic, M = monoclinic and R = rhombohedral[1]. The high temperature rhombohedral structure of tricalcium silicate has the smallest unit cell and the highest symmetry. All the

other polymorphs (T1, T2, T3, M1, M2, and M3) have larger unit cells which are a distortion of the rhombohedral cell, due to displacements of the SiO_4 tetrahedra[10]. Full crystallographic data are available for all the polymorphs except M2. Certain polymorphs can be stabilized by introducing foreign ions, that block polymorphic transition during cooling[10–13].

Bigarré et al.[10] investigated the 7 polymorphs of tricalcium silicate, using in situ XRD. The modification of the XRD spectra was monitored during heating C_3S between room temperature and 1100°C and compared with the different polymorph stabilized with Zn. It was shown that a monoclinic C_3S M1 at 980°C and the M1 stabilized at room temperature with Zn have slight differences in their XRD spectra. Golovastikov et al.[14], determined the unit cell parameters of the room temperature triclinic C_3S. The unit cell was described by tetrahedra of silica and octahedra of calcium oxides, with different coordination numbers depending on the linkage with a tetrahedron or an octahedron. Then doped C_3S with different cations was studied, each cation present in the structure stabilizes the silica tetrahedra in a different position. The orientation of the tetrahedra defines the symmetry of the structure, which explains the relationship between rhombohedral true cell and the different superstructures of the polymorphs.

This distortion of the unit cell may not be identical in each unit cell, creating a modulation. It means that when a tetrahedron changes orientation, a slight displacement occurs within the cell. In some cases, a commensurable modulation is observed. After a few cells, the unit cell is identical to the first one, creating a measurable sequence. This phenomenon is only visible by high resolution TEM[15]. The triclinic T1 superstructure of single crystal of pure C_3S has a 1-D commensurable modulation perpendicular to the (122) with a modulation wave of 6 times the (122) spacing. Due to the presence of foreign cations a non-homogeneous distortion of the unit cell occurs in doped C_3S. In this case the structures are incommensurately modulated, meaning that there is no repetition of the unit cell. In doped C_3S with Zn at different concentration to have M1, M2 and M3 structures, only the M1 and M2 structure have a commensurate modulation[16]. No exact modulations of the M3 structure have been proposed, probably due to the complex effect of the foreign ion.

2.1.1 Tricalcium silicate

Pure tricalcium silicate (Ca_3SiO_5, C_3S) was synthesized from a 3:1 stoichiometric mixture of calcium carbonate ($CaCO_3$) and high purity quartz powder (SiO_2), both from Merck. The powders were homogenized for 24 hours in water and the blend dried at 100 °C for 24 hours. The dried material was then pressed into pellets and heated at 1600 °C for 8 hours. The heating ramp was 200 °C per hours, to insure a complete decarbonation of the material. The total heated time was 16 h. The pellets were quenched in air after heating and finally ground for 30 seconds in a disc mill. After grinding, the sample was gently tumbled in a Turbula blender for 8 hours. About 400 g of C_3S powder is produced in one batch.

(a)   (b)
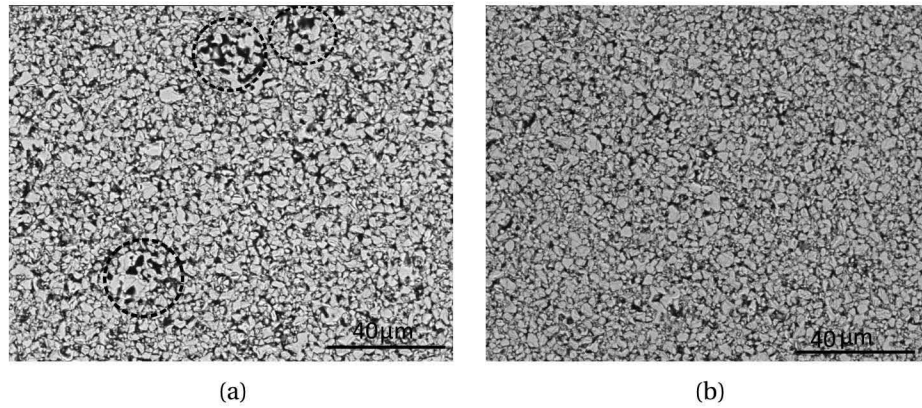
Figure 2.1: Effect of Turbula on the agglomeration of C_3S, before (a) and after (b) tumbling.

Figure 2.1 shows the particles before and after de-agglomeration for 8 hours in the Turbula. It can be seen that agglomerates (dashed circle in Figure 2.1 (a)) are removed by this process (Figure 2.1 (b)).

The quality of the resulting C_3S powder was characterized by XRD. Rietveld analysis revealed a triclinic C_3S with an amount of free lime below the detection limit (0.5 %). Two different batches were prepared, Figure 2.3 (a) shows their particles size distribution. A good reproducibility in reactivity was observed between C_3S batches, as shown by their calorimetry curves in Figure 2.2.
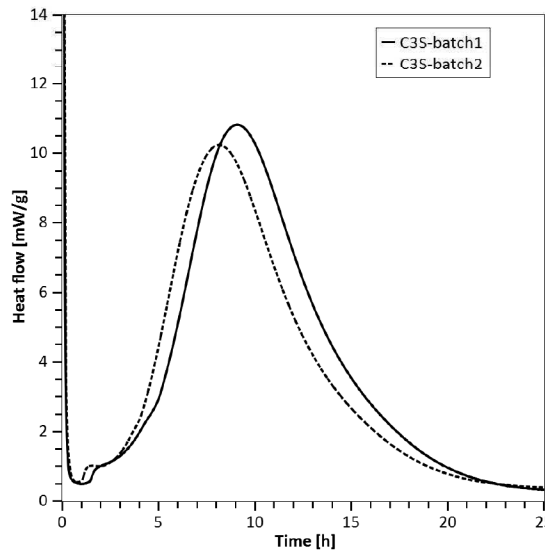
Figure 2.2: Calorimetry curves of the two different C_3S batches.

9

2.1.2 Fillers

A limestone, durcal 2 from Omya, was used as filler. This material was selected for its narrow particles size distribution and similar to the pure C_3S, as indicated by Figure 2.3 (b).

(a)   (b)
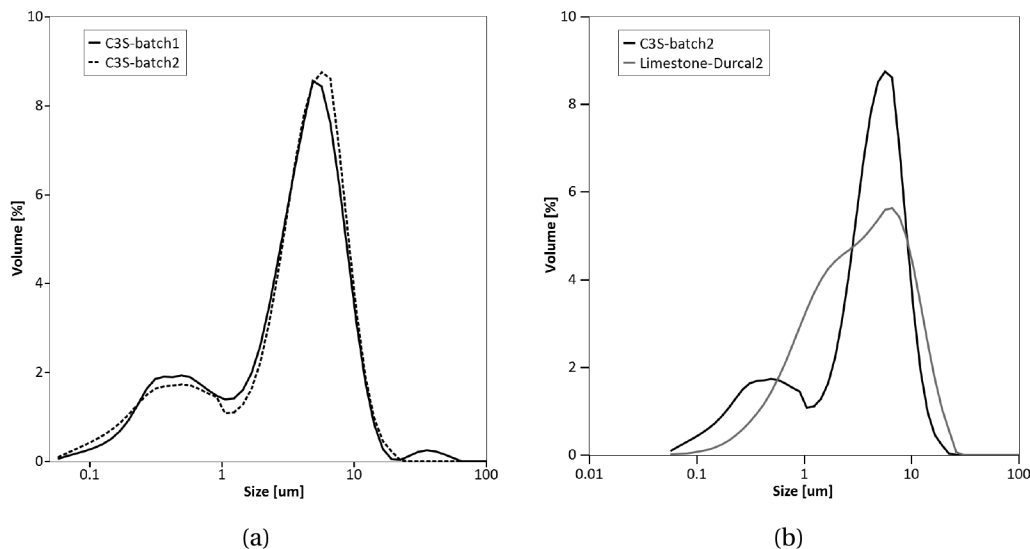
Figure 2.3: Particles size distribution of (a) the different C_3S batches, (b) the limestone Durcal 2 fillers.

2.1.3 Alites from China

In collaboration with a postdoctoral fellow from Nanjing Institute of Technology, different types of alites were prepared: pure C_3S, alite with magnesium and alite with zinc. Magnesium was chosen because of its common presence in alite of commercial cement clinker, whereas zinc was chosen because of its potential accelerating effect. Magnesium can stabilize the structure T3 if its content is below 1wt%[17;18] and M3 if it its content is higher than 1wt%. Zinc stabilizes T1 between 0 and 0.5wt%, then T2, M1 and M2 with increasing amounts of zinc addition. However, the reported limits for stabilization of the different polymorphs vary significantly between different studies, perhaps due to volatilization of zinc during synthesis as found below[10;16;19].

Pure C_3S was synthesized in the laboratory from a 3:1 stoichiometric mixture of calcium carbonate ($CaCO_3$) and high purity SiO_2 powder. The powders were dry homogenized for 3 hours. The homogenized powders were then pressed into pellets and heated at 1500 °C for 12 hours. After 6 hours, the heating process was interrupted and the sample was quenched in air, reground and recompacted before further heating. The pellets were quenched in air after heating and finally dry ground into powder. The alites were prepared by mixing $CaCO_3$, SiO_2, 1.5 and 2 wt% of MgO or 3 and 4 wt% of ZnO. The chemical composition in g, determined by XRF is given in Table 2.1.

Table 2.1: Chemical composition the alites sythetised in China.

	CaO	SiO$_2$	MgO	ZnO
Pure C$_3$S	72.80	24.47	0.00	0.23
Alite 1.5%wt Mg	70.98	24.68	1.38	0.08
Alite 2%wt Mg	70.58	24.62	1.78	0.00
Alite 3%wt Zn	72.27	24.46	0.00	0.98
Alite 4%wt Zn	71.57	24.62	0.00	1.16

Knowing the chemical composition of the alites, in the rest of the text alite with 1.5 wt % MgO is replaced by 1.38, alite with 2 wt % MgO is replaced by 1.78, alite with 3 wt % ZnO is replaced by 0.98 and alite with 4 wt % ZnO is replaced by 1.16.

To reduce the influence of particle size distribution on the hydration kinetics, the powders were sieved to obtain a narrow size distribution between 25 and 36 μm (Figure 2.4 (a)). About 10 g of sieved powder was obtained for each alite. Even though the different powders were sieved, the surface area was estimated from 2D images by the line intersection method[20]. A difference about 11 % was found between alite with zinc and alite with magnesium. To check that differences in PSD could not explain the differences in kinetics, 5 g of each raw alite was also wet ground in a Mc-Crone micronizer for 10 minutes in order to obtain a very fine powder (Figure 2.4 (b)).

(a)

(b)
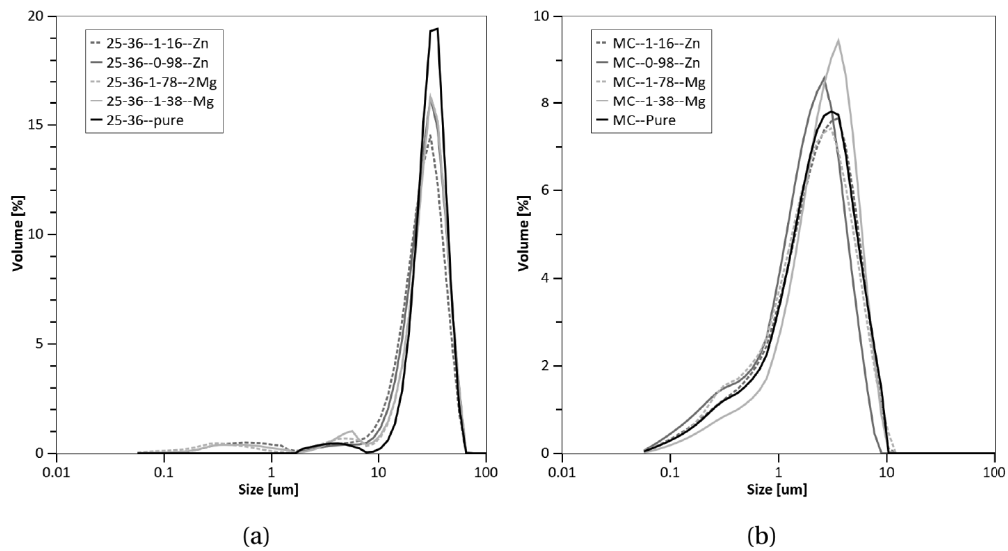
Figure 2.4: Particles size distribution of the alites from China (a) sieved between 25 and 36 μm and (b) after 10 minutes in Mc-Crone Micronizer.

Polymorph identification

The type of polymorph is identified from the presence of two or three peaks in the 32.3-33 ° and 51-52.5 ° angular windowand through a comparison with literature data of alite incorporating magnesium [12;21;22] and zinc [10;16;19]. From Figure 2.5, it can be observed that pure C_3S and alite doped with zinc are triclinic and alite doped with magnesium is monoclinic.
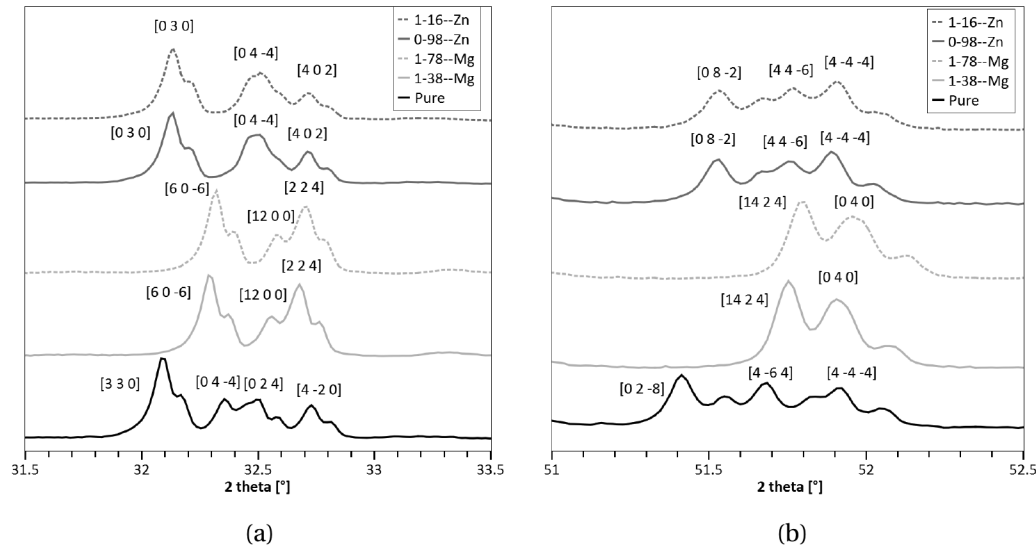
Figure 2.5: Angular range of the XRD pattern of alites (a) 31.5 to 33.5 °, (b) 51 to 52.5 °.

The diffractograms were refined for each existing structure of the polymorphs T1 [14], T2 [17], T3 [18], M1 [23], M3 [24] and R [25] and the best fit was selected. Rietveld analyses were done to determine the content of alite and the presence of residual free lime, periclase and zinc oxide. The pure C_3S is triclinic, T1, as expected and its free lime content is below the detection limit.

The two alites doped with magnesium have the M3 structure. The free lime and periclase contents of both alites doped with magnesium are below the detection limit.

The two alites doped with zinc are best fitted by the T2 structure. However, a T3 structure cannot be excluded. In the literature [10;16] large amounts of zinc incorporation are reported to stabilize stabilizes the polymorph M2, whereas T2 is usually found for lower zinc concentration. The XRF revealed a content of zinc of 0.98 wt% for the alite produced with 3 wt% of zinc and 1.16 wt% for the alite produced with 4 wt% of zinc. Most probably zinc evaporates during synthesis, as also observed by Urabe et al. [16]. No zinc oxide was detected in any sample, but small amounts of free lime were found: around 0.8 wt% for the alite with 0.98 wt% of zinc and around 0.4 wt% for the alite with 1.16 wt% of zinc.

Polymorph of pure C_3S, alite with 1.38 wt% of magnesium and alite with 1.16 wt% of zinc were further investigated by [29]Silicon nuclear magnetic resonance (^{29}Si NMR). Figure 2.6 shows the resulting spectra. The NMR analyses confirmed the absence of belite in the samples.

The analyses also confirmed that pure C_3S is triclinic T1 and alites with magnesium are monoclinic M3 compared with literature of ^{29}Si NMR spectra of pure C_3S and alite doped with magnesium[26;27]. In the case of zinc, a broadening of the peaks was observed and in consequence no precise identification of the polymorph was possible.
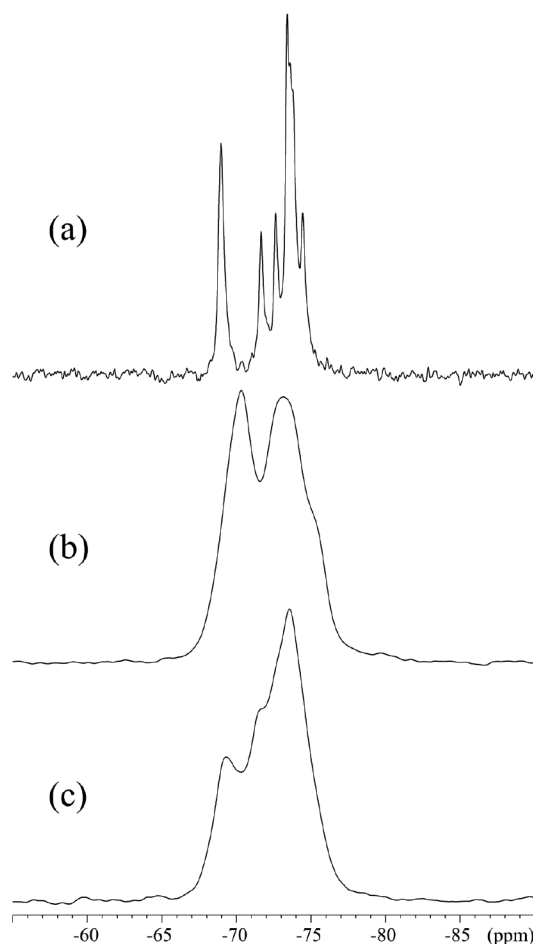
Figure 2.6: ^{29}Si NMR spectra of a) pure C3S, b) alite with 1.38 wt% of Mg and c) alite with 1.16 wt% of zinc.

The ^{29}Si chemical shift depends on the local order and the linewidths on the order on a longer scale. Thus, only the T1 polymorph is highly ordered from a structural point of view. If an artificial linebroadening is applied to the spectrum of the T1 polymorph, a spectrum which is similar to the spectrum for the alite doped with zinc is obtained, with only small differences in peak positions, similar to the NMR spectra of the M1 polymorph[27]. This result may indicate either that the local environments of the SiO_4 tetrahedra for the M1 polymorph are very similar to those of the T2/T3 polymorphs, or the spectrum for the alite doped with zinc is linebroadened by the incorporation of the Zn_2^+ ions in the structure in a manner that has not resulted in a polymorphic transformation from trigonal to monoclinic. Furthermore, ^{29}Si MAS NMR spectra of the T2 and T3 polymorphs have not been reported.

13

2.1.4 Alite

Alite with 2 wt% MgO and 1 wt% Al_2O_3 was synthesized in our laboratory. This composition has been chosen because of its similarity with the alite present in Portland cement, with respect to its chemical composition, particle size distribution and reactivity, as studied by Costoya[28]. The alite was synthesized following the same procedure as pure C_3S, from a 3:1 stoichiometric mixture of calcium carbonate ($CaCO_3$), high purity quartz (SiO_2) powders, doped with high purity MgO and Al_2O_3. The pellets were heated at 1450 °C for 14 hours for 3 cycles until no more free lime was detected, by Holcim, 5113 Holderbank. The pellets were quenched in air after heating.

Two separated batches were prepared. Rietveld analysis revealed a monoclinic alites M3, with an amount of free lime and periclase below the detection limit (0.5%). Table 2.2 gives the chemical composition obtained by XRF.

Table 2.2: Chemical composition of the two batches of alite synthetized in our laboratory.

	CaO	SiO_2	MgO	Al_2O_3
Alite batch 1	71.38	25.31	2.01	1.12
Alite batch 2	70.42	25.12	2.06	1.39

For alite, it is more difficult to obtain a good reproducibility 2 batches, as shown by their calorimetry curves in Figure 2.7. The two batches heated at 1450 °C during 14 hours for 3 cycles were compared with some alite was heated in our laboratory furnace at 1600 °C for 16 hours. The impact of the initial heating temperature on the reactivity revealed to be important.
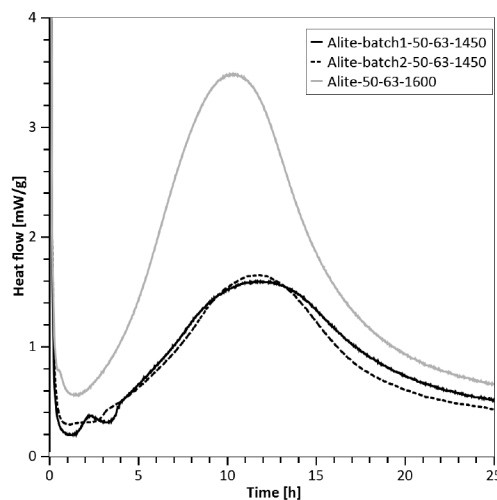
Figure 2.7: Calorimetry curves of the two batches of alites heated at 1450 °C compared with a batch heated at 1600 °C.

After the synthesis, the two batches followed different particles size selections. Batch 1 was ground for 30 seconds in a disc mill and separated in different particles size distribution by sieving. The obtained powders are shown in Figure 2.8 (a). About 50 g of powder was obtained after sieving.

Batch 2 was ground using two different grinding methods, vibratory disc milling and a Mc-Crone micronizer device. The powders obtained were sieved between 25 and 36 μm. Finally, a part of the sieved powder obtained by disc milling was cleaned in an ultrasonic bath of isopropanol, to remove small particles that adhere on the surface. Figure 2.8 (b) shows the resulting particles size distribution. About 10 g of powder was obtained for each treatment.

(a)   (b)
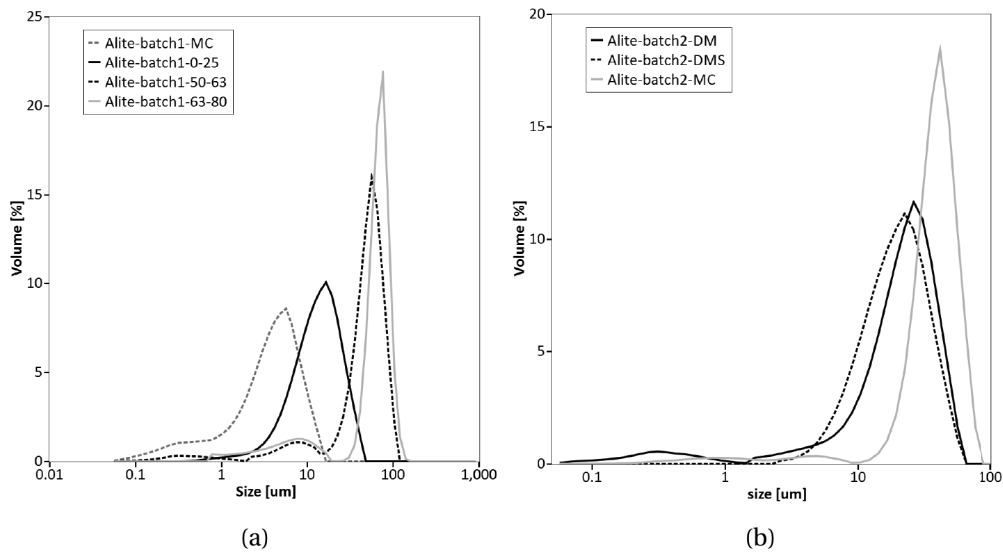
Figure 2.8: Particles size distribution of (a) the batch 1 of alite, (b) the batch 2 of alite.

2.1.5 Clinker

Fresh clinker nodules were obtained from Holcim, 1312 Eclepens. The chemical composition determined by XRF is given in Table 2.3.

Table 2.3: Chemical composition of the clinker

	CaO	SiO_2	Al_2O_3	Fe_2O_3	MgO	K_2O	SO_3	Na_2O	TiO_2	P_2O_5	Mn_2O_3
Clinker	65.21	21.39	5.43	3.40	2.33	0.94	0.50	0.31	0.31	0.19	0.09

The clinker was ground following the exact same procedure as described for the batch 2 of alite. For the hydration reaction, gypsum from Merck was added. Gypsum was sieved below 36 μm to have similar particle size distribution as clinker, as shown in Figure 2.9 (a).

2.1.6 Cement

Cement Normo4 was obtained from Holcim, 5113 Holderbank. Table 2.4 gives its chemical composition.

Table 2.4: Chemical composition of the cement.

	CaO	SiO_2	Al_2O_3	Fe_2O_3	MgO	K_2O	SO_3	Na_2O	TiO_2	P_2O_5	Mn_2O_3
Normo 4	64.94	20.66	4.50	3.12	1.86	0.96	3.06	0.05	0.34	0.23	0.05

The cement was sieved between 25 and 36 μm. A part of the sieved powder obtained was cleaned in an ultrasonic bath of isopropanol, to remove small particles that adhere to the surface. Figure 2.9 (b) shows the particle size distribution.
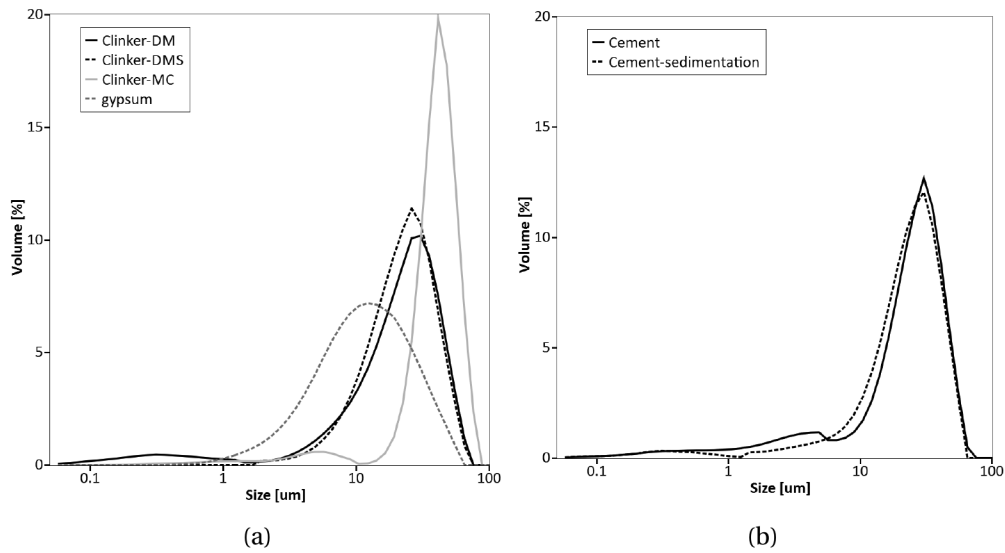
Figure 2.9: Particles size distribution of (a) the clinker and gypsum, (b) the cement.

2.1.7 Summary of the materials

The different powders used in this study are summarized in Table 2.5 with their specific surface area (SSA). Due to the limited amount of each sieved materials no measurement of their specific surface area was possible by nitrogen absorption (BET). The specific surface area was calculated from the particle size distribution assuming spherical particles and bulk densities (3150 kg/m^2 for alite and clinker). Due to this assumption, values indicated in Table 2.5 are estimated values and can only be compared within each other.

Table 2.5: Summary of the different powders prepared

	Grinding	Sieving	dv_{50} [μm]	SSA From PSD [cm^2/g]
C$_3$S batch1	30 s Disc mill	no	3.7	17799
C$_3$S batch2	30 s Disc mill	no	4.4	19077
Alite batch1	10 min micronizer	no	3.4	16323
Alite batch1	30 s Disc mill	< 25 μm	18.5	6271
Alite batch1	30 s Disc mill	50 - 63 μm	47.5	3172
Alite batch1	30 s Disc mill	63 - 80 μm	72.3	660
Alite batch2	30 s Disc mill	25 - 36 μm	15.4	8142
Alite batch2	30 s Disc mill + susp	25 - 36 μm	18.5	3993
Alite batch2	30 s micronizer	25 - 36 μm	35.9	1691
Clinker	30 s Disc mill	25 - 36 μm	21.2	6070
Clinker	30 s Disc mill + susp	25 - 36 μm	21.5	3806
Clinker	30 s micronizer	25 - 36 μm	38.2	1176
Gypsum	Powder	< 36 μm	10.8	2756
Cement	Ground	25 - 36 μm	23.5	4320
Cement	Ground + susp	25 - 36 μm	22.4	3898
C$_3$S China	30 s Disc mill	25 - 36 μm	28.7	873
Alite 1.5Mg China	30 s Disc mill	25 - 36 μm	26.9	3390
Alite 2Mg China	30 s Disc mill	25 - 36 μm	26.9	4781
Alite 3Zn China	30 s Disc mill	25 - 36 μm	26.8	935
Alite 4Zn China	30 s Disc mill	25 - 36 μm	24.1	3550
C$_3$S China	10 min micronizer	no	2.2	18749
Alite 1.5Mg China	10 min micronizer	no	2.5	15069
Alite 2Mg China	10 min micronizer	no	2.5	19010
Alite 3Zn China	10 min micronizer	no	2.0	23095
Alite 4Zn China	10 min micronizer	no	2.1	20101
Durcal 2	Powder	no	3.2	14600

2.2 Classical characterization methods for cementitious materials

2.2.1 Grinding

Different grinding devices were used to grind the synthesized materials. The first one was a vibratory disc mill from Siebtechnik, Mülheim. This is a dry grinding method, where attrition occurs due to impact of the particles with each other, which can introduce defects in the particles. The typical particle size after grinding is between 0.1 and $100\,\mu$m. With such a method, agglomeration of the finer particles may occur. After grinding, the sample with the finner particles were gently tumbled in a Turbula blender for 8 hours with zirconium balls, to break up any agglomerates.

A micronizer device from Mc-Crone was used for a wet grinding. Isopropanol was used as dispersing agent. It requires pre-ground material with particles below $500\,\mu$m. Particle size distribution then obtained ranged between 0.01 and $1\,\mu$m.

2.2.2 Particle size distribution

The particles size distribution (PSD) was measured by laser diffractometry in a Malvern MasterSizer S using isopropanol as dispersing agent.

The technique is based on the principle that particles passing through the laser beam will scatter the light at a certain angle depending on their size. The technique takes the assumption that particles are spherical.

This techniques has some limitation for measuring precisely the particles size distribution of cementitious materials. First of all because particles are not spherical at all. Second because different mathematical model can produce the particles size distribution from the laser diffraction. The specific surface area was calculated from the PSD.

2.2.3 X-Ray fluorescence

X-Ray fluorescence (XRF) was used to determine the composition of the raw materials. Elements are reported as their oxide forms to conform to the practices set forth in ISO 12677 Chemical analysis of refractory products by XRF – Fused cast bead method. The samples were dried at $105\,°$C for 24 hours and then ignited at $950\,°$C for 1 hour. The fusion made uses 1g of ignited sample + 8 g of Lithium Tetraborate ($Li_2B_4O_7$). The XRF analyses were performed on ARL Instrument calibrated for UniQuant in fused bead form. All the XRF measurement were done by APC-Solutions, Rte de Denges 36, CH-1027 Lonay.

2.2.4   X-Ray Diffraction

All alites were characterized by X-Ray Diffraction (XRD) and Rietveld refinement. The powder diffraction spectra were acquired in a X'Pert MPD PRO diffractometer with $CuK_{\alpha 1}$ radiation ($\lambda = 0.154$ nm). The X-ray tube worked at 45 kV and 40 mA. The optic configuration was a fixed divergence slit (1/2°), a fixed incident antiscatter slit (1°) and X'Celerator RTMS detector. The samples were prepared using the back-loading technique to avoid compaction of the powder. There is a surface with a random orientation of the particles, which limits the preferential orientation. Data were collected from 7° to 70° for 30 min.

The alite polymorph identification crystal structure refinement was done with the using software X'Pert High Score Plus Rietveld analysis software by evaluating the fit between literature structure models and the XRD pattern using the full range of data. The following parameters were fitted: Zero zero shift, background, scale factor, lattice parameters (constrained within a 1 % deviation from the literature data) and a Lorentzian peak shape broadening parameter. The concentration of minor and trace phases such as free lime (CaO) and periclase was determined using Rietveld quantitative phase analysis as detailed in[29].

2.2.5 ^{29}Si MAS nuclear magnetic resonance

Silicon nuclear magnetic resonance was also used to determine the polymorph of the different alites. The ^{29}Si MAS NMR analysis was done by Jorgen Skibsted of the University of Aarhus. The spectra were acquired at 9.39 T on a Varian INOVA-400 spectrometer, using a home-built CP/MAS NMR probe for 7 mm o.d. rotors. The experiments employed a spinning speed of 6.0 kHz, single-pulse excitation, a relaxation delay of 60 s, and 1024 scans.

2.2.6   Isothermal Calorimetry

As the hydration reaction of cement is exothermic, its kinetics can be followed by isothermal calorimetry. The resulting hydration kinetics curves describe the sum of all the contribution from each ongoing reaction. It is important to note that the peaks may be due to simultaneous reaction and do not necessary describe one process. The measurements were done in an isothermal calorimeter TAM air from Thermometric at 20.0 ± 0.1 °. To have an homogeneous paste, samples with a water to solid ratio of 0.4 (as a basis, if other values are used it is mentioned in the text) were mixed by hand for 2 min. Hand mixing was the most appropriate method due to the limited amount of sieved materials available. About 3 g of paste was added into the reaction vessel and transferred into the calorimeter. Data were recorded over a period of 2 days.

2.2.7 Conductivity

The dissolution of samples was followed by measuring the conductivity of the solution with a water to solid ratio range between 20 and 50 at $20\,^\circ$ (MonoCAD). Samples were mixed $30\,\text{s}$ by hand before introducing them in the cell. The conductivity is proportional to the concentration of ions in solution. As the concentration of silicate ions is low compared to the calcium concentration, the conductivity can be interpreted as the variation of $[Ca^{2+}]$ and $[OH^-]$ in solution. Since the system is diluted a greater quantity of material must dissolve to reach the same concentration and the hydration kinetics are slowed down[30].

2.2.8 Cure and hydration stop

For the study hydrate studies, powders were mixed with deionized water and about $1\,\text{g}$ of paste was sealed in a plastic container, for hydration durations less than 1 day. For longer hydration time, a few drops of saturated lime solution were added on the top of the paste and the container was sealed. Pastes were hydrated at $20\,^\circ$.

The hydration was stopped by two different means depending on the age of the samples[31]. For samples hydrated for less than 24 hours, the hydration was stopped by freeze-drying. The sample was immersed in liquid nitrogen ($-196\,^\circ$) for $15\,\text{min}$. Since small samples were cast, pore water is instantaneously frozen. The frozen water was removed by sublimation in a Telstar Cryodos freeze-dryer. For the samples hydrated for times longer than 1 day, the solvent exchange procedure was used[31]. The hydrated samples were immersed in a large volume of isopropanol for 7 days. The isopropanol progressively replaces water by diffusion. Isopropanol was replaced after one day to improve the efficiency. Then the samples were dried in a vacuum desiccator under silica gel for two days.

2.2.9 Thermogravimetric analysis

The amount of hydrates developed was determined by thermogravimetric analysis (TGA) on a Mettler Toledo TGA/SDTA 851e device. Dried samples were gently ground and $50\,\text{mg}$ of powder was introduced in the furnace crucibles (alumina). To avoid carbonation, samples were ground a minute before introduce them in the furnace. The samples were then heated, under a $30\,\text{ml/min}$ flow of N_2, from $30\,^\circ\text{C}$ to $900\,^\circ\text{C}$ with a $10\,^\circ\text{C/min}$ ramp and weight was continuously measured.

2.3 Electron microscopy

2.3.1 Scanning electron microscopy techniques

Two different imaging modes were used in the scanning electron microscope (SEM): secondary electron (SE) to study the topography of fractured surfaces and back-scattered electron (BSE) to characterize the microstructure of polished cross-sections. In addition, BSE observations were completed by a chemical analysis by X-ray energy-dispersive spectroscopy (X-EDS)[32].

To generate characteristic X-Rays, the energy of the incident beam should be around 2 times the ionization energy for the respective X-ray line of the atom. In cement the X-ray line with the highest energy is Fe-K$_\alpha$ (K$_{\alpha 1}$ 6.4 KeV), so the applied high tension selected should be > 12 KeV. The quantification of X-rays allows the determination of the chemical composition. However some precaution needs to be taken when doing quantification, because the X-Ray intensity generated for each element is proportional to the concentration of the considered element in the sample, the probability of X-ray production, the path length of the electrons in the specimen and the absorption of X-Rays in the sample. These so-called matrix effects vary with the sample composition. There are procedures implemented in the quantification software where the intensity for each element of the sample is compared with the intensity of a standard of the element and the effect of atomic number (Z), absorption (A) and fluorescence (F) are calculated and corrected in an iterative way. In this study, the so called "phi-rho-Z" method with standards was used to take into account matrix effect of the sample in the quantification process[32].

SEM-EDX results were compared with the results obtained from quantitative wavelength dispersive spectrometry (WDX). In this method, the energy of the characteristic X-Ray is identified by varying the angle at which Bragg's law is satisfied. The spectrometer scans through a range of angles and the X-ray intensities are collected. Then the quantification procedure is the same as for EDX analysis, i.e comparing the peak intensity of the element with the peak intensity of the standard sample and take into account the matrix effects.

2.3.2 Sample preparation for scanning electron microscopy

The anhydrous powders were dispersed on a carbon tape and a conductive carbon layer was deposited. Then samples were studied in SE mode in a FEI XLF30-FEG operating at 10 KeV.

The hydrated samples were gently crushed after drying, to study single grains. Powders of dried samples were also dispersed on a carbon tape and no conductive coating was applied to avoid artifacts. The hydrate morphology over the first 24 hours was observed in SE mode in a Zeiss Merlin operating at 2 KeV. Such a low voltage was applied to avoid the charging effects. This microscope is designed to operate at low probe current, in this case about 200 pA, and it possesses a high sensitivity detector which allows observations of beam-sensitive, non-conductive samples without damaging and charging effects.

For BSE images (mass density contrast), anhydrous and dried samples were impregnated in an epoxy resin and polished with diamond paste with a grain size down to 1 μm. Finally, a conductive carbon layer (around 10 nm thickness) was added.The microstructure on the polished cross-section was studied in BSE mode in a FEI Quanta 200 operating at 15 KeV. The microscope is also equipped with a Brucker AXS XFlash detector for EDX analysis.

WDX analysis was done at UNIL on a JEOL JXA 8200 microscope. The applied voltage was 15 KeV with a beam current of 20 nA and a take off angle of 40 °. For the study, standards were measured before the analysis. We used: wollastonite for calcium and silicon, periclase for magnesium and corundum for aluminum.

2.3.3 Transmission electron microscopy technique

Transmission electron microscopy allows very local observation of the sample. Details that cannot be captured in SEM can be studied in TEM, such as the morphology hydrates. However, due to the high magnification, the field of view is limited, and care is needed regarding the representativity of the observed area. Also, the high current density used in TEM techniques may destroy the sample by excessive heating.

Transmission electron microscopy is complex and involves a wide range of techniques. For this study two principal techniques were used, bright field (BF) and dark field (DF) imaging and scanning transmission electron microscopy (STEM). For the first one, the image is formed using the transmitted beam (BF) or one of the diffracted beams (DF). For the second one, the electron probe is focussed into a small probe and scanned over the sample and at any point of the specimen the signal generated is detected. In STEM mode, different detectors are used to detect the electrons that form the image. In this study, bright field (STEM-BF) and high angle annular dark field (HAADF) detectors were used. The first one picks up the transmitted electrons. The HAADF detectors detects electrons scattered to high angles, forming Z-contrast images[33]. The STEM mode is also used to control the beam position for EDX mapping.

In transmission electron microscopy EDX quantification is done using the standard-less Cliff-Lorimer method. This method stipulates that the intensity ratio between two peaks is proportional to their weight fraction as per equation 2.1:

$$\frac{C_A}{C_B} = k_{AB} \frac{I_A}{I_B} \tag{2.1}$$

$\frac{C_A}{C_B}$ is the weight fraction between to elements A and B, k_{AB} is a factor taking into account the microscope parameters and $\frac{I_A}{I_B}$ is the intensities ratio between 2 peaks of the two elements A and B

This assumes that the thickness is small and homogeneous through the whole sample. This way, absorption and fluorescence effects can be neglected if all elements in the sample are identified[33].

2.3.4 Sample preparation for transmission electron microscopy

The preparation of TEM lamellas of cementitious materials is difficult. There are two problems: first the anhydrous grains are extremely hard compared to the hydrates and the embedding resin, which makes homogenous polishing of the whole compound challenging; second, the hydrates are beam-sensitive, thus there is a risk of deterioration during preparation and observations.

First, the TEM lamellas were produced by focused ion beam (FIB) Zeiss, Nvision 40. In the FIB microscope two canons are used: electrons are used for imaging and ions for cutting, deposition of material and imaging. The dual beam type FIB allows a precise selection of the region of the lamella ($5x10\,\mu$m). The region was selected with the SEM and a carbon protective layer was deposited to preserve the surface (Figure 2.10 (a)). The sample was milled to produce a lamella for $5x10\,\mu$m in size and $1\,\mu$m in thickness. Then, the lamella was extracted with a piezo-controlled micro-manipulator (kleindieck) and welded on a copper support grid (Figure 2.10 (b)). Finally, the lamella was thinned down to electron transparency (about $100\,$nm) as required for the transmission electron microscopy (Figure 2.10 (c)). This method allows a precise selection of the region of interest. However, its drawback is the limited size of the lamella, especially for the particles, where only the edges and subsurface regions are of interest.

(a)

(b)

(c)
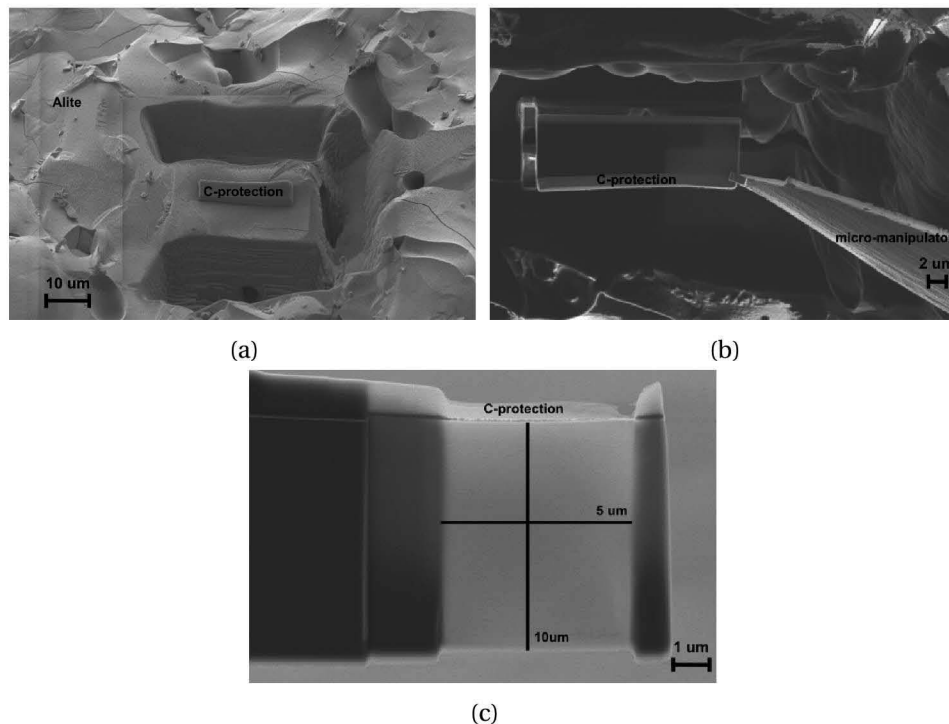
Figure 2.10: Production of a TEM lamella by FIB: (a) Selection of the area where the lamella is extracted. (b) Extraction of the lamella. (c) Thinning of the lamella, fixed on the copper grid.

The second preparation method was the conventional mechanical polishing followed by ion milling. With mechanical polishing several thin sections can be produced in one sample. The method is extremely time consuming due to the difficulty to thin down the hard sample and the region of interest cannot be precisely selected.

For the powder samples, a third method was developed. Firstly, the anhydrous powder was mixed with a G2 "hard polishing" resin. Semi-circular discs, 3 mm diameter, were cut from the blocks. The discs were mechanically polished on the two sides to reach a 20-50 μm thickness. Then some areas ("windows") containing the grain edges were thinned down by focused ion beam. This last method allows a precise selection of the grain, and several samples can be produced on one semi-disc. There is no need for transferring sample inside the FIB, which reduces the time for preparation. The hydrated samples were prepared by this method, with some adjustment. Small blocks (about 1 mm length) of dried samples were first impregnated in an epoxy resin in order to fill the pores to preserve the microstructure. The extra resin was removed and the mix paste-epoxy resin was mixed with the G2 hard resin (Figure 2.11 (a)). Then the same polishing method was used and thin areas were produced, selecting regions containing anhydrous grains and surrounding hydrates in the FIB microscope (Figure 2.11 (c)). The thin areas must be produced close to a side of the semi disc, in order to reduce the shadowing effect in EDX analysis due to the remaining walls (Figure 2.11 (b)). This procedure was chosen because the G2 hard resin was more rigid for the sample manipulation.

(a)   (b)

(c)
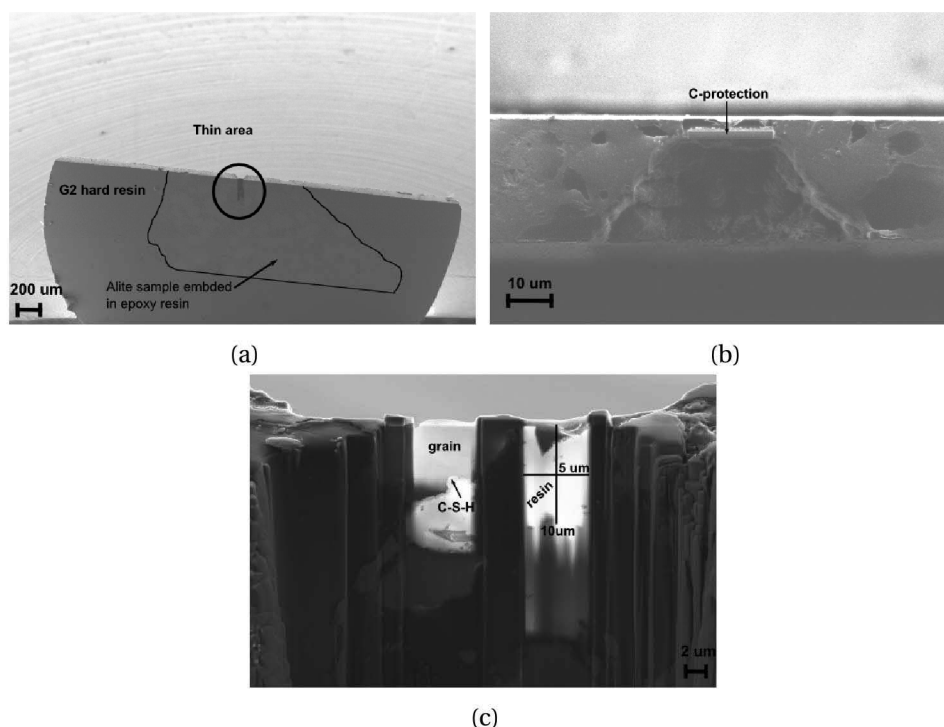
Figure 2.11: Production of a TEM lamella by mechanical polishing and FIB for the production of the thin areas: (a) Overall view of the semi disc, polished to 20-50 μm. (b) Selection of the windows with the FIB. (c) Thinning of the lamella.

A FEI Technai Osiris, with the field emission gun operating at 80 KeV and a Phillips CM12 (tungsten filament) operating at 120 KeV were used both in bright field mode to characterize the defect density in the samples. The FEI Technai Osiris was also used to study the hydrate's morphologies and chemical composition by STEM-EDX.

The FEI Technai Osiris has a Schottky type field emission gun, which has high brightness. The resulting beam has small spot size and a high beam current (300 nA) which means a higher electron density in STEM mode, compared to tungsten filament. The current value was reduced to 0.2 nA to limit heating damage; the total acquisition time for mapping was 15 min.

The chemical analysis was done on the same microscope with a Bruker Nano XFlash Detector. The microscope has been optimized for STEM-EDX analysis thank to large detectors areas, which allows a fast detection even at low currents. The EDX detector is composed by 4 quadrants distributed around the sample holder to maximize the detection of X-rays. In order to avoid shadowing of a detector by the sample and to increase the count number of X-rays, the sample holder was tilted 20 ° and 2 detectors were shut down, as illustrated in Figure 2.12.
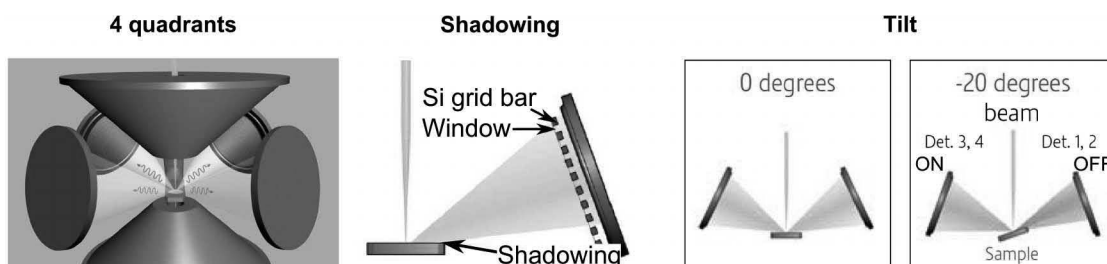
Figure 2.12: Configuration of the EDX detectors: disposition of the detector around the sample, shadowing effect of the sample, effect of the tilt on the shadowing. Adapted from notice of FEI Company[34].

2.3.5 Comparison between SEM-EDX, SEM-WDX and STEM-EDX techniques.

The alites obtained revealed Al-rich and Mg-rich regions inside grains, meaning that not all the added magnesium and aluminum were incorporated in the crystal structure as shown by Figure 2.13.
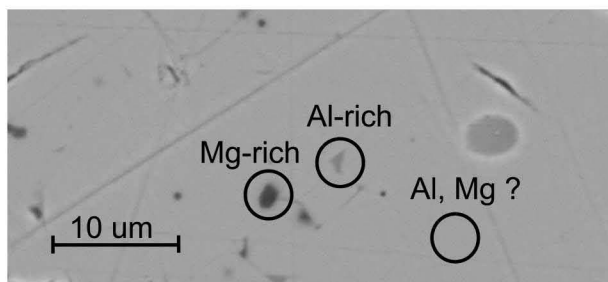
Figure 2.13: Alite grain with Mg-rich and Al-rich clusters

The amount of magnesium and aluminium incorporated in alite was determined by XRF, and compared with the results obtained by SEM-EDX, SEM-WDX and STEM-EDX techniques. The XRF gives the total amount without differentiation between the amount in exsoluted region and incorporated. The microscopy techniques allow the selection of regions without clusters. With SEM techniques, the interaction volume can be large (5 μm in diameter) and it can take into account a cluster which is not visible from the surface. The STEM technique allows a localized analysis of the composition, since interaction volume is small due to the small thickness of the sample. Table 2.6 compares the results obtained with the different techniques to the calculated amount of each element from the synthesis recipe.

Table 2.6: Atomic composition of the alites, calculated and determined by XRF, SEM WDX, SEM EDX and STEM EDX

At %	Ca	Si	Mg	Al	O	C/S
Calculated from synthesis	**31.89**	**10.84**	**1.28**	**0.50**	**55.55**	**2.94**
XRF batch 1	29.28	9.85	1.17	0.51	51.46	**2.97**
XRF batch 2	29.44	9.78	1.19	0.64	51.10	**3.01**
SEM WDX batch 1	32.61	10.73	0.83	0.37	55.46	**3.04**
SEM EDX batch 1	27.92	9.36	0.98	0.48	60.99	**2.98**
SEM EDX batch 2	29.68	9.91	0.90	0.51	58.76	**3.00**
STEM EDX batch 1	31.65	11.20	1.12	0.64	55.38	**2.83**
STEM EDX batch 2	30.45	10.78	1.03	0.55	57.18	**2.82**

Since exsoluted regions are present, a lower amount of magnesium and aluminum than the calculated one is expected to be incorporated in the bulk structure. For such low amount of material (less than 1 at %) the measurement error becomes important. The peak intensity is very low and a good correction of the background is crucial for the accurate quantification of the element. The SEM-WDX technique uses standards accurate for the elements studied. The SEM-EDX method compares the results with a database. The STEM-EDX method is standard less and compares the intensity between two peaks of two elements of the sample. In this case, an accurate background correction is crucial.

As a conclusion, for the determination of low amounts of of an element (less than 1 at %), the SEM-WDX technique gives the better results, followed by STEM-EDX and SEM-EDX. SEM-WDS allows a relatively easy and short sample preparation compare to STEM-EDX. However SEM-WDX uses strong beam current which can damage the sample, especially hydrated samples are very sensitive. In this case, SEM-EDX technique gives a good compromise between quality of the analysis and beam damage. STEM-EDX techniques requires difficult a sample preparation, but it is useful for to study small region of interest, where the interaction volume in SEM is too large. STEM-EDX is particularly indicated to determine the composition of C-S-H in sample at only few hours of hydration, where the thickness of C-S-H rim is less than 1 μm.

3 Induction period

Part of the results of this chapter have been published as an article in the Journal of the American Ceramic society[35] and another part have been subtmited in the Journal of the American Ceramic society.

This chapter presents the effects of different parameters such as the water to cement ratio, the grinding procedure, the annealing of alite and the nature of doping ions in alite on the duration of the induction period. The duration of the induction period depends on the defect density of the sample and the composition of the solution. The crystalline defects present in pure C_3S and alite samples at different stages of their fabrication are studied by transmission electron microscopy. Grinding, annealing and foreign ions are used to change the defect density in C_3S and alite samples. The water to cement ratio is used to change the solution composition and thus the driving force for dissolution. The impact of changes in the crystal defects and solution composition are investigated and related to the hydration kinetics and microstructural development of the different samples.

3.1 Litterature review on the induction period

3.1.1 Theories about induction period

Protective membrane

One of the first theories proposed to explain the first deceleration and induction period was the formation of a protective membrane by Stein and Stevels[36]. An impermeable protective membrane was supposed to form around C_3S grains preventing further dissolution. To explain the end of the induction period, some authors argue that hydration resumes when the membrane converts into a layer more permeable to water[36;37]. Others argued that the membrane breaks due to osmotic pressure due to acceleration[38;39]. Gartner et al.[40], by reviewing the pore solution composition from several data, observed differences, whether measurements are done at early or later ages. Thus, they proposed that the formation of two different types

of C-S-H, with different solubilities. They attributed to the first C-S-H formed a metastable, protective characteristic. This C-S-H was assumed to form all around the C_3S grain and act as protective layer at the surface of the grain. Then, they assumed that this C-S-H underwent a solid-state transformation into a stable but permeable C-S-H layer, which causes the end of the induction period. Recently, Bellmann et al. studied C_3S hydration by NMR[41]. After 5 min of hydration, they observed the formation of monomeric silica that they attributed to a hydroxylated surface or a first hydrate with a different composition than C-S-H. They postulated that during the hydration of C_3S, two different products form, the first one called the intermediate phase, which acts as a protective membrane, which transforms into the second one called C-S-H. Their observations were confirmed by the analysis of the surface by X-Ray photoelectron spectroscopy[42], where the XPS analysis shows that 56% of the C_3S surface is covered by the intermediate phase after 30 min of hydration. Even if XPS[42;43] and NMR[41;44] studies shows the formation of a product, with different characteristics than the final C-S-H formed, no evidence of a continuous layer formation has been observed[45].

Nucleation and growth

Other theories to explain the induction period are that the nucleation and growth of hydrates CH and C-S-H control the kinetics[46;47]. Some authors relate the induction period to a poisoning of the CH nuclei by silicates[48–50]. The CH nuclei cannot grow until the end of the induction period, when supersaturation level is high enough. Thus seeding C_3S with CH nuclei should shorten the induction period. However, it was found that the seeding of CH nuclei has no impact on the length of the induction period[47]. Others authors claim that the induction period and the acceleration periods are completely controlled by the nucleation and growth of C-S-H[51–53]. Garrault and Nonat[51] developed a model, where the number of nuclei dictates the kinetics of the hydration of C_3S. Immediately after the immersion in water C-S-H starts to form. When they reach a critical number and size the nuclei start to grow leading to the acceleration period. Thus there is no real induction period, but a continuous development of C-S-H. Thomas et. al[53] could demonstrate by seeding C_3S with C-S-H nuclei that no induction period is present anymore. The nucleation of C-S-H theory has good arguments to explain the induction period. However, these theories explain with difficulty the rapid slow down before the induction period, where the crystal dissolution theory is needed.

Geochemical theory about dissolution

Juilland et. al[5] proposed a model to explain the mechanism of hydration at early age, based on the crystal dissolution theory developed by Lasaga et al.[54]. The composition of the solution controls the dissolution kinetics, and thus the dissolution proceeds by different mechanisms, according to the degree of undersaturation. Three types of features can form at the mineral surfaces depending of the degree of undersaturation[55]. For high levels of undersaturation, vacancy islands, small holes at the surface of mineral can nucleate without requiring defects. At intermediate undersaturation levels, etch pits nucleate at the intersection of a dislocation

or other defects with the surface of the mineral. Such sites have an excess of surface energy. For low levels of undersaturation, step retreat takes place at pre-existing roughness, either formed by etch pits, or general surface roughness. The existence of these features indicates that the processes at the surface of certain minerals controls the kinetics of dissolution and diffusion plays a secondary role. According to the model[5], the early mechanism of hydration of C_3S takes place in three steps. When C_3S is in first contact with water, there is a fast dissolution and hydroxylation of the surface due to the high undersaturation level. Vacancy island and etch pit formation starts. As the concentration of calcium ion in water increases, the undersaturation coefficient decreases. Second, there is a slow dissolution rate until the calcium ion concentration reaches a critical supersaturation with respect to Portlandite. There is no longer enough energy to nucleate etch pits and the dissolution proceeds by step retreat, the lateral propagation of step at any roughness of the surface (kinks). Finally, at the supersaturation level of Portlandite, there is a massive precipitation of hydrates. From this point, the growth of hydrates controls the rate of dissolution.

Figure 3.1 shows a schematic representation of dissolution rate of alite presented by Juilland et al.[5].
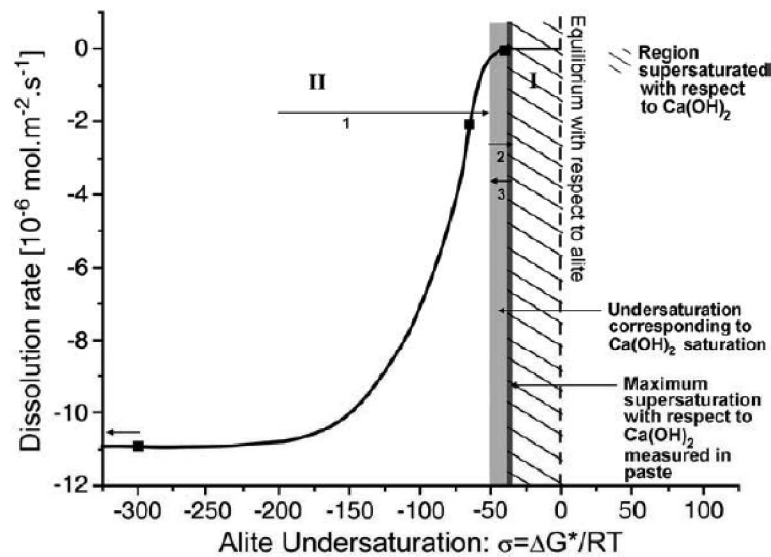
Figure 3.1: Schematic representation of the dissolution rate of alite, from Juilland et al.[5]. II indicates dissolution controlled by etch pits formation, I indicates dissolution rate controlled by step retreat propagation. The squares on the curve indicates measured value of the dissolution rate of alite.

The dissolution experiments from Nicoleau et al.[56] shows good agreements with the theory that alite dissolves with different dissolution rates according the solution concentration. Figure 3.2 shows the dissolution rate of alite in solution with different lime concentration, measured by Nicoleau et al.[56].
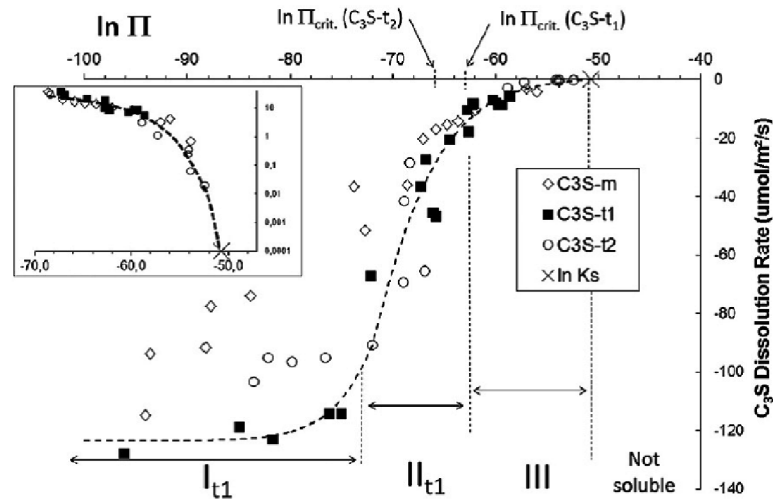
Figure 3.2: Dissolution rate of alite in solution with different lime concentration, measured by by Nicoleau et al.[56]. Domain III indicates dissolution controlled by step-waves propagation, domain II transition between step-wave propagation and etch pits formation and domain I corresponds to the etch pits formation.

In C_3S hydration, the relation between the duration of the induction period and defect density was already established[57]. Odler and Schüppstuhl[57] observed an increase of the induction period for slower cooling rates, for samples stored for one year, for samples having a smaller specific surface area and for higher water to cement ratios. They conclude to a modification of the defect density in the samples due to the different treatments, or a modification of the solution composition in the case of an increased water to cement ratio. Sakurai et al.[58] evoked the role of defects during the hydration of C_3S, without determining them. Groves and co-workers[59–61] studied the crystalline structure of cement phases by means of transmission electron microscopy. They observed twin bands[59] and planar defects[60] in alite.

The application of the crystal dissolution theory to hydration of C_3S to explain the induction period has been discussed by Gartner[62;63] and by Makar et al.[64;65]. Gartner[62] had concerns about the very large difference in the concentration of the solution when the dissolution rate slows down and the values of the solubility of C_3S calculated from bulk thermodynamics. The evaluation of the solubility of alite from bulk calculation may be very different from the real value as it doesn't take into account the surface. Lüttge[66] discussed the importance of considering the proper surface dissolving for calculating the dissolution rate. Makar et. al[64] suggested that the etch pits observed in the surface of alite are holes in the protective membrane. Instead of a change in the dissolution mechanism, they suggest the presence of a protective membrane, which inhibits the dissolution leading to the induction period. Juilland et. al[67] put forward the theory described above, by describing the dissolution into 2 processes. First, there is the detachment of atoms from the surface and second, their transport through the solvent phase (diffusion). When alite is in first contact with water, the solution is highly undersaturated and the reaction is controlled by transport of species through the solution.

When the undersaturation degree is reduced, surface reaction becomes the controlling process. As mixing has an influence on the gradient of ionic concentration, it would influence only the first minutes of hydration, when the reaction is controlled by transport[68].

3.1.2 Parameters influencing the dissolution rate

Arvidson and Luttge[69] compared the dissolution rates of albite crystal surfaces (001), with the same mineral pre-etched several hours in a disodium tetraborate buffer. Distinct dissolution profiles were measured on the two different samples. There was not enough energy to form etch pits on the fresh sample, whereas on the pre-treated sample, etch pits initially formed were propagated as step waves and were progressively diminished in depth, until their complete disappearance. As the energy was not sufficient to generate new etch pits, they grew in radius but did not continue to deepen. The transition from a fast to a slow dissolution varied for the two samples. Their experiment strongly suggest that the history of the mineral influences the absolute dissolution rate and the surface evolution for a same mineral. Figure 3.3 shows the transition from slow dissolution regime (rate I) and fast dissolution regime (rate II).
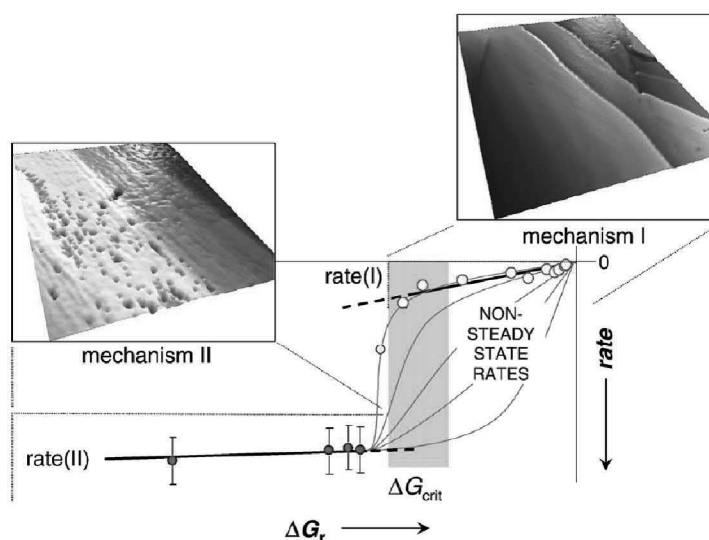
Figure 3.3: Dissolution pathways of albite mineral. Transition from rate I to rate II is dependent of the previous interaction between fluid and mineral. From Arvidson and Luttge[69].

As a consequence, the behaviour of the dissolution rate over time is also a function of sample pre-treatment and the initial surface roughness, in particular the availability of kinks[69;70].

A large number of studies reported a variation in the dissolution rate due to different sample preparations. These differences include the shape of the mineral, whether it is ground particles or a flat surface, the surface orientation and the surface morphology. Surface area normalized dissolution rates were shown to depend on crystal orientation[71] and powder fineness.

An enhancement of the dissolution rates was measured for powder materials compared to fractured surface[72;73] and the enhancement further increased for finer powder samples and shock loaded ones[74–76]. Finally, the surface state is one of the most important parameters that controll the dissolution rate. MacInnis and Brantley[77] measured different dissolution rates for four different calcite samples with different dislocation density and surface morphologies. Cleaved surfaces and the same surfaces abraded with a 22 μm grit were produced. Both sets of samples were strained and unstrained in a Brace type rig. The dissolution experiments showed an order of magnitude of difference in dissolution rates between cleaved unstrained and cleaved strained samples. The results also showed a significant increase of the dissolution rates for the abraded surface samples, compared with the cleaved surfaces. When the surface was rough, no differences in the dissolution rates were observed between the strained and unstrained samples. Also two types of pits were observed, one type nucleated at dislocations and the other type nucleated on the surface. This study suggested that dislocations induced by grinding have much more influence on the dissolution rates than shock loading. Grinding induces damage in the surface, which will enhance dissolution. Similar results were observed for dissolution experiments on damaged magnesium oxide surfaces[78]. MgO samples with (100), (110) and (111) surface were prepared and abraded with a grinding wheel. The dissolution rate decreased as soon as the damaged layer was removed. The damaged layer produced in MgO crystals consisted of two parts. The first one, thin, was a severely damaged layer, where cracks and dislocations developed. The second one, thick, was a plastically deformed layer, where slip bands developed.

In summary, previous work clearly demonstrated that surface roughness and damage and the particle size have an important effect on dissolution rates. Significant increase was observed when samples were as powder or when the surface was damaged by grinding or abraded. This indicates that the sample conditioning and grinding operations strongly affects the reactivity of cementitious materials. The different procedures that can affect the dissolution rate are described in the next sections.

Grinding procedure and particles morphology

Petrovich[79;80] reviewed the effect of grinding on the dissolution kinetics of quartz, oxides and silicates under laboratory conditions. Particles after dry grinding were characterized in terms of surface chemistry, grain shapes and microrelief, grain size distribution and mutual adhesion of fragments and sub-surface damage. It was observed that microfragments of particles of 0.01-0.1 μm diameter stuck on the surface of bigger particles, even after ultrasonic cleaning. The lattice strain and amorphous content increased after grinding. The amorphous content was defined as regions containing an extremely high density of dislocations. The amount of microfragments and amorphous content were much reduced by grinding materials with a liquid grinding agent. The presence of these micro-fragment largely contributed to the enhanced dissolution rates.

Tromans and Meech[81–84] studied mechanical transformations occurring during the grinding

procedure, and pointed out two mains mechanism. First, fracture occurs due to tensile stresses developed at crack tips and produces angular fragments with little subsurface damage as described by the classical crack propagation theory established by Griffith in the 1920s[85]. The initial fracture and size reduction of minerals occurs by the propagation of larger cracks present in the particle at a relatively low strain. As particle sizes decrease during grinding initial crack tip lengths do so too. Consequently, the loading stress must be increased in order to reduce further the particle size. Eventually, a limiting particle diameter is reached below which it is not possible to reduce size. Second, local stress can be sufficient to promote shape changes due to plastic deformation via dislocation propagation and results in significant subsurface damage. In terms of energy, particles with more plastic deformation (i.e. the smallest ones) have a higher molar free energy due to an increase in the stored energy due to dislocations. The development of a large number of dislocations may result in a decrease of the long range lattice order. This destruction of the lattice can be seen in XRD as the formation of an amorphous region.

Few studies focus on the effect of grinding procedure of cementitious materials and its consequent impact on hydration kinetics. Mori et al.[86] reported that a prolonged milling of tricalcium silicate rendered part of the material amorphous, resulting in a shortened induction period. As extreme damage of the structure may appear as an amortization of the materials in the XRD pattern, these results are in good agreement with the amorphisation of the damaged layer formed at the surface due to milling.

Thermal treatment

Annealing may allow removal of defects created during grinding. The effect would be a reduction of the dissolution rate. Cygan and co-workers[87] investigated the dissolution kinetics of deformed and annealed silicate minerals. Samples of labradorite mineral were shock loaded and some annealed at different temperatures. The shocked samples exhibited slightly higher dissolution rates, while the shocked and annealed samples exhibited lower dissolution rates.

Fierens and co-workers[88;89] reported modifications in the thermoluminescence spectra of C_3S after thermal treatment between 800 °C and 1600 °C and an extension of the induction period, which they related to a reduction in defect density. Juilland[5] showed a drastic extension of the length of the induction period for alite with a narrow size distribution after annealing for 6 hours at 650 °C, but did not look directly at the defect density. A similar phenomenon was reported by Bellmann[90] on thermally treated pure C_3S.

Thompson et al.[91] studied the effect of annealing on the crystal structure of alite doped with magnesium. A reduction of MgO in solid solution was observed after annealing. An increase of the duration of the induction period of the annealed alites were reported.

Doping ions

In cement, alite contains various foreign ions, which will changes its reactivity. These foreign ions can change the crystal structure of C_3S, as described in chapter 2. The mechanism by which ions influence the reactivity of alite is not well understood. The presence of the ions in the crystal lattice can induce defects such as vacancies. Changes in reactivity are often attributed to the polymorph, but the presence of foreign ions in the solution could also influence the nucleation or growth of hydrates.

Odler and Schüppstuhl[57] observed an increase of the duration of the induction period in the presence of aluminium. However, it was not mentioned how aluminium was acting. Begarin et al.[92] showed that the nucleation of C-S-H is retarded in the presence of aluminium. They conclude that the length of the induction period correspond to this delay. Fierens and co-workers[93;94] measured different density of surface defects when C_3S samples were doped with different foreign ions.

3.2 Systems studied

The different batches and sample preparation are described in Chapter 2.

Pure C_3S batch 1 and alite batch 1 were annealed in a tubular furnace, with the temperature and duration indicated in Table 3.1. After annealing, the samples were quenched in air. The annealing of C_3S was repeated in a chamber furnace for 1h at 650 °C. This furnace allows a precise measurement of the temperature inside the chamber at the actual temperature was 630 °C, while no measurement of the exact temperature in the tubular furnace was allowed. The temperature 650 °C was selected according to results from Juilland[5], and 850 °C was selected to gain insight into the effect of the temperature.

Table 3.1: Temperatures and durations of annealing

	T [°C]	duration
C_3S batch 1	650	10 min, 1h, 6h
C_3S batch 1	850	1h
C_3S batch 1	650	1h
Alite batch 1 < 25	650	1h
Alite batch 1 50-63	650	10 min, 1h, 6h
Alite batch 1 63-80	850	1h, 6h

To study the impact of grinding, alite batch 2 and clinker were ground using two different grinding methods, vibratory disc milling and a Mc-Crone micronizer device. Disc mill grinding was used as a dry grinding method. For each disc-mill grinding cycle, 100 g of raw material was ground during 30 seconds.

To study the impact of the specific surface area, alite batch 1 was ground by disc mill for 30s and then the particles were separated by sieving in different sizes. In order to have a very fine powder, some of the powder was further ground 10 minutes in the Mc-Crone micronizer device.

Mc-Crone grinding was used as a wet grinding method. This method is recognized to induce fewer defects in the materials[95]. Mc-Crone grinding requires pre-ground material between $100\,\mu$m and $500\,\mu$m. 5 g of pre-ground powder was mixed with 4 ml of isopropanol and ground for 30 seconds. This procedure was repeated until a sufficient quantity of material of the desired size fraction was obtained (in this study about $10\,$g). After grinding, the powder was dried $12\,$h in an oven at $60\,°$C in order to evaporate the isopropanol grinding liquid. This step induced aggregation of the particles and a slight post hand grinding was necessary to disaggregate the powder before the sieving.

The powders obtained were sieved between 25 and $36\,\mu$m. Finally, a part of the sieved powder obtained by disc milling was cleaned in an ultrasonic bath of isopropanol, in order to remove small particles that adhere on the surface. The washing was done by suspending 25 g of powder in 100 ml of isopropanol during 3 min in an ultrasonic bath. The suspension was taken out of the ultrasonic bath and left for sedimentation for about 15 min. After sedimentation, the supernatant was discarded and the whole cycle was repeated. At least 5 cycles of suspension/sedimentation were done for each treated sample. After sedimentation, the slurry was dried $12\,$h in an oven at $60\,\mu$m in order to evaporate the isopropanol.

For alite batch 2 and clinker, the three grinding procedures used are summerized in Table 3.2.

Table 3.2: Grinding procedure and nomenclature for alite batch2 and clinker.

	Disc mill	Disc mill + sedimentation	Mc-Crone micronizer
Alite	ADM	ADMS	AMC
Clinker	CDM	CDMS	CMC

Table 3.3 shows the spread in the particle size distribution for the different grinding procedures.

Table 3.3: Spread in the particles size distribution

	dv_{10} [μm]	dv_{50} [μm]	dv_{90} [μm]	Span
ADM	2.2	15.4	32.9	2.00
ADMS	7.4	18.5	34.1	1.44
AMC	20.1	35.9	53.6	0.93
CDM	5.1	21.2	41.0	1.69
CDMS	8.2	21.5	39.1	1.44
CMC	22.1	38.2	55.5	0.87

Figure 3.4 shows the resulting particle size distribution.
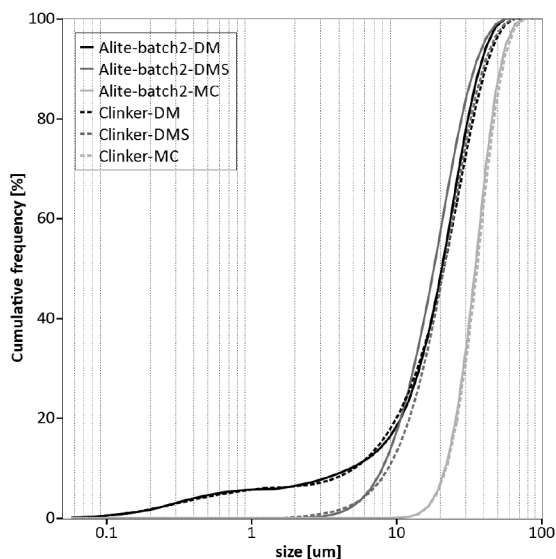
Figure 3.4: Particle size distribution of alites and clinker.

Cumulative frequency was used to emphasize the portion of small particles present after the grinding procedure. Disc mill grinding gives the largest spread in the particle size distribution for both alite and clinker as indicated by Span in Table 3.3. This grinding technique gives a higher amount of small particles. Small particles are removed after the sedimentation. Mc-Crone micronizer grinding gives a much narrower particle size distribution and no small particles. However, the mean size of the particles was larger than that of the materials ground by the disc mill. Due to the limited amount of each powder prepared, no measurement of their specific surface areas by BET was possible.

3.3 Parameters influencing the induction period

3.3.1 Particles shape

The particles shapes were compared and related to the duration of the induction period for alite and clinker. In the case of clinker, 5 wt% of gypsum was added prior to mixing the sample with water.

Calorimetry was done on both clinker and cement, to compare laboratory produced sample with industrially produced ones (Figure 3.5). The effect of the sedimentation is the same on industrial cement as on clinker and alite.

Figure 3.5: Calorimetry curves of cement, with and without sedimentation (a) calcorimetry curve (b) Induction period.

The impact of the grinding procedure on early hydration of alite and clinker is shown by Figure 3.6 and 3.7 respectively.

The sample ground by disc milling has the shortest induction period. When small particles are removed, the induction period is extended and the heat released during induction period is lowered. When the sample is wet ground, the length of the induction period further increases in the case of alite, but the heat released during the induction period is at the same height than the samples ground by disc mill followed by sedimentation.

The conductivity measurement clearly shows three different dissolution rates for the three grinding procedures for both alite and clinker (Figure 3.6 and 3.7). At first, there is an increase in conductivity, corresponding to the dissolution of alite and probably also some precipitation of C-S-H. The conductivity reaches a maximum, followed by a sharp drop, which corresponds to the precipitation of Portlandite. After the sharp drop, there is a gradual decrease in the conductivity towards the equilibrium saturation of Portlandite. There are two modifications of the conductivity curve due to the grinding procedure. First, for the samples without debris, the rate of increase in conductivity in the dissolution curve is lower indicating a slower dissolution rate. Second, the maximum conductivity is slightly reduced, suggesting a reduction in the critical supersaturation for Portlandite precipitation. These observations are consistent with the observations from isothermal calorimetry.
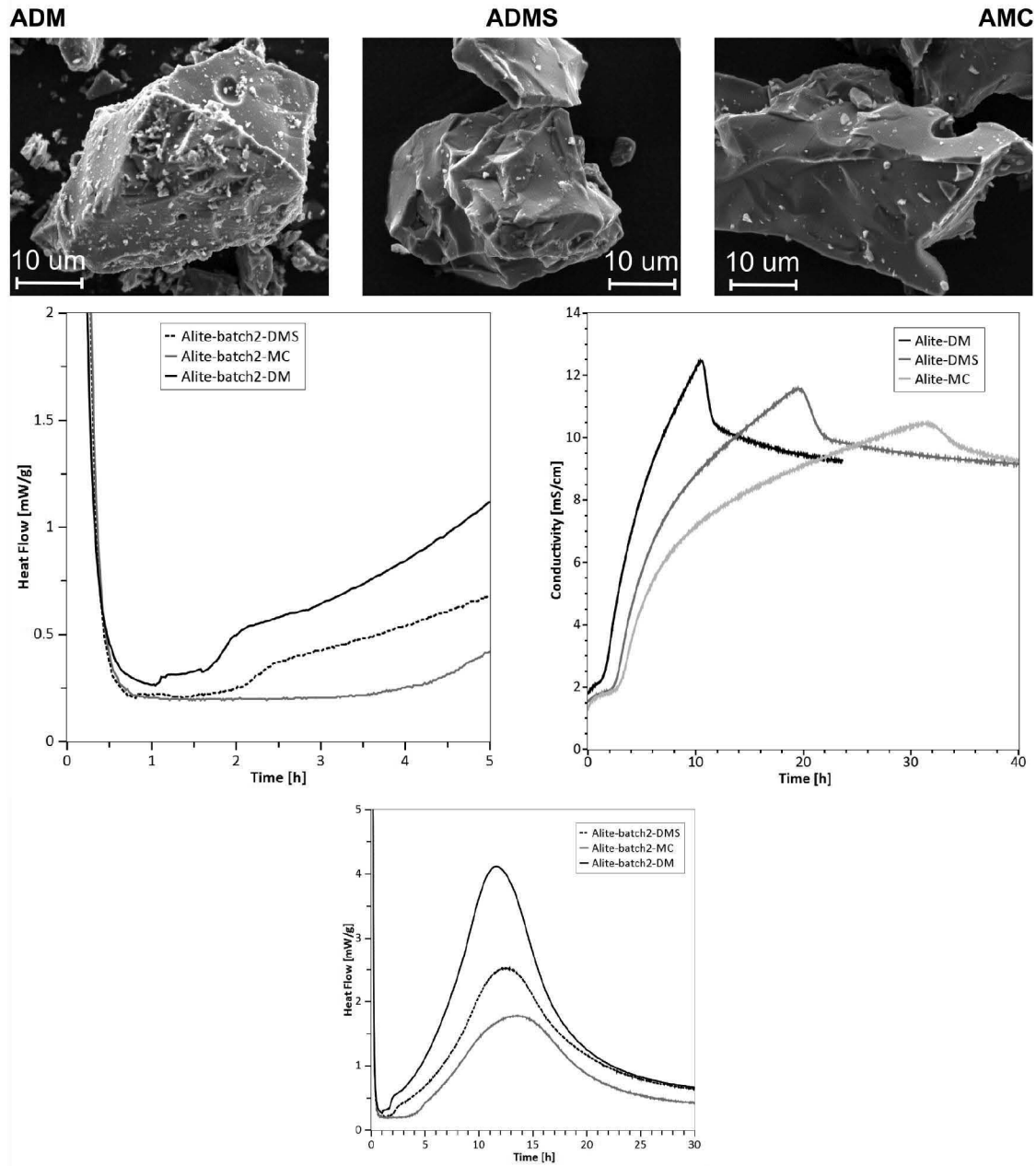
Figure 3.6: Effect of the grinding procedure on the particles shape and the duration of the induction period of alite. SEM images in secondary electron mode of alite ground by disc mill (ADM), disc mill and sedimentation (ADMS) and Mc-Crone micronizer grinding (AMC). Calorimetry curves of alite showing the effect of grinding procedure. Conductivity measurements of alites after the different grinding procedures at w/c = 20.
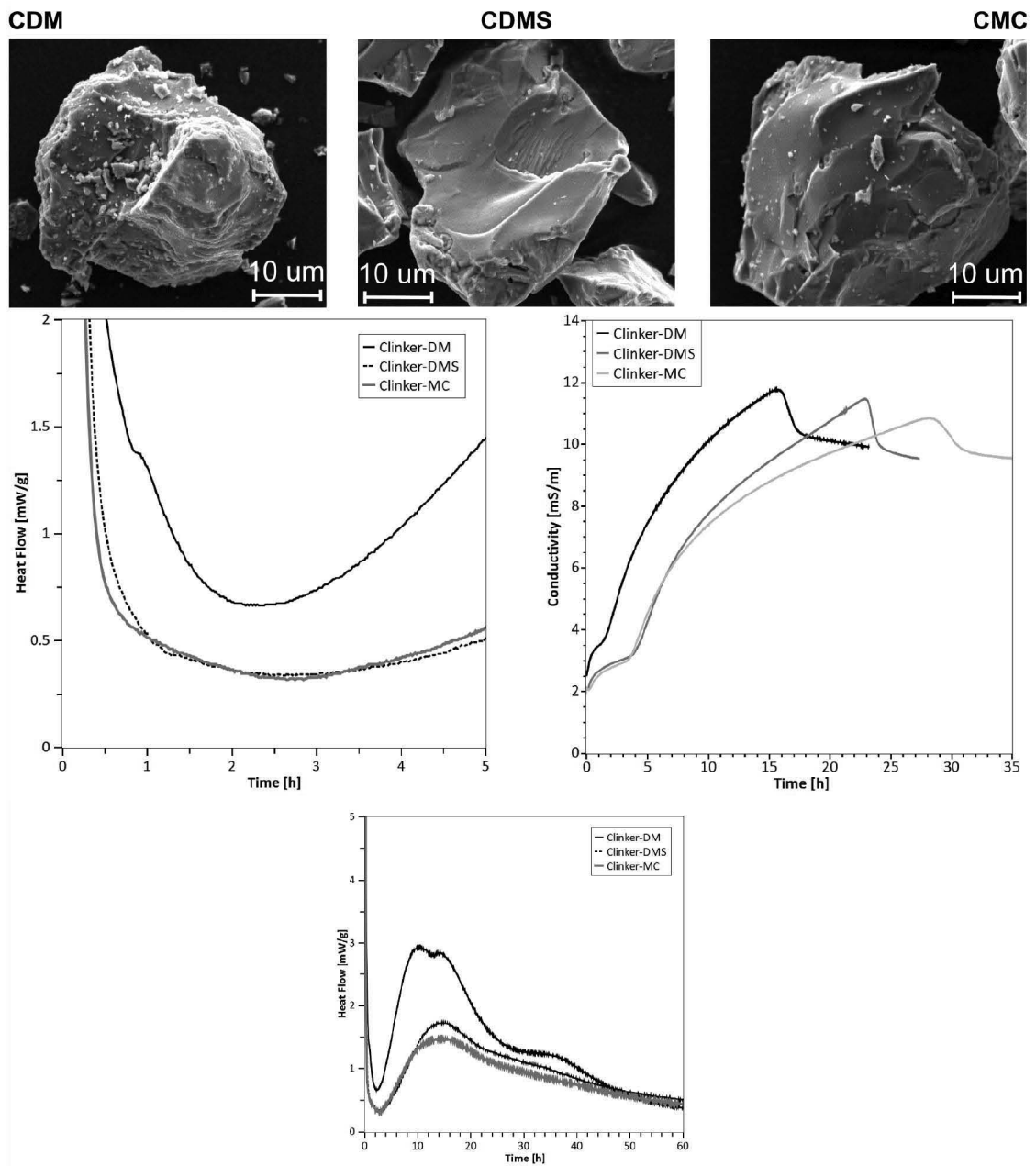
Figure 3.7: Effect of the grinding procedure on the particles shape and the duration of the induction period of clinker. SEM images in secondary electron mode of clinker ground by disc mill (CDM), disc mill and sedimentation (CDMS) and Mc-Crone micronizer grinding (CMC). Calorimetry curves of clinker showing the effect of grinding procedure. Conductivity measurements of clinkers after the different grinding procedures at w/c = 20.

The SEM images in Figure 3.6 and 3.7 illustrate the state of the surface of the different powders. In general, the different grinding procedures have the same impact on both alite and clinker. Disc milling grinding results in more rounded particles with a lot of asperities, facets, kink and steps (microrelief) on the surface. Particles of intermediate size are observed for the disc mill grinding. For the powder ground by disc mill, small particles adhere to the surface of larger particles. The removal of these small particles by the sedimentation is evident. Particles ground by Mc-Crone micronizer tend to show an elongated aspect, which may explain the apparently larger size of particles measured by the laser diffraction technique. Fewer small particles are observed adhering to the surface compared to the disc mill samples. The Mc-Crone micronizer samples show fresh fractured surfaces, with large flat areas with sharp edges.

The subsurface properties of alite were studied in TEM thin sections. Figure 3.8 shows TEM images in bright field mode of alite grains ground by disc mill and by the Mc-Crone micronizer mill. The particles showed a highly deformed zone close to the surface, which is more pronounced for alites ground by disc mill. This deformed zone is not continuous all along the surface and has a variable thickness. The thickness of the deformed layers was estimated from all the images obtained and on average there is no significant difference between the two milling procedures. However, the deformed layer was encountered much more frequently in alite ground by disc mill, than in alite ground by Mc-Crone micronizer. Stacking faults are observed in the middle of the grains, which are more present in alite ground by disc mill.

Small debris was also examined, and for both grinding methods, all small debris observed are clearly more damaged that the bigger particles, as indicated by Figure 3.8.

Attemp was done to study by XRD if an amophisation of the power was induced by the grinding procedure. Since the quantification of the amourhous content by XRD is dependent of the particles size distribution[29], it was not possible to compare results because the samples had different specific surface areas.
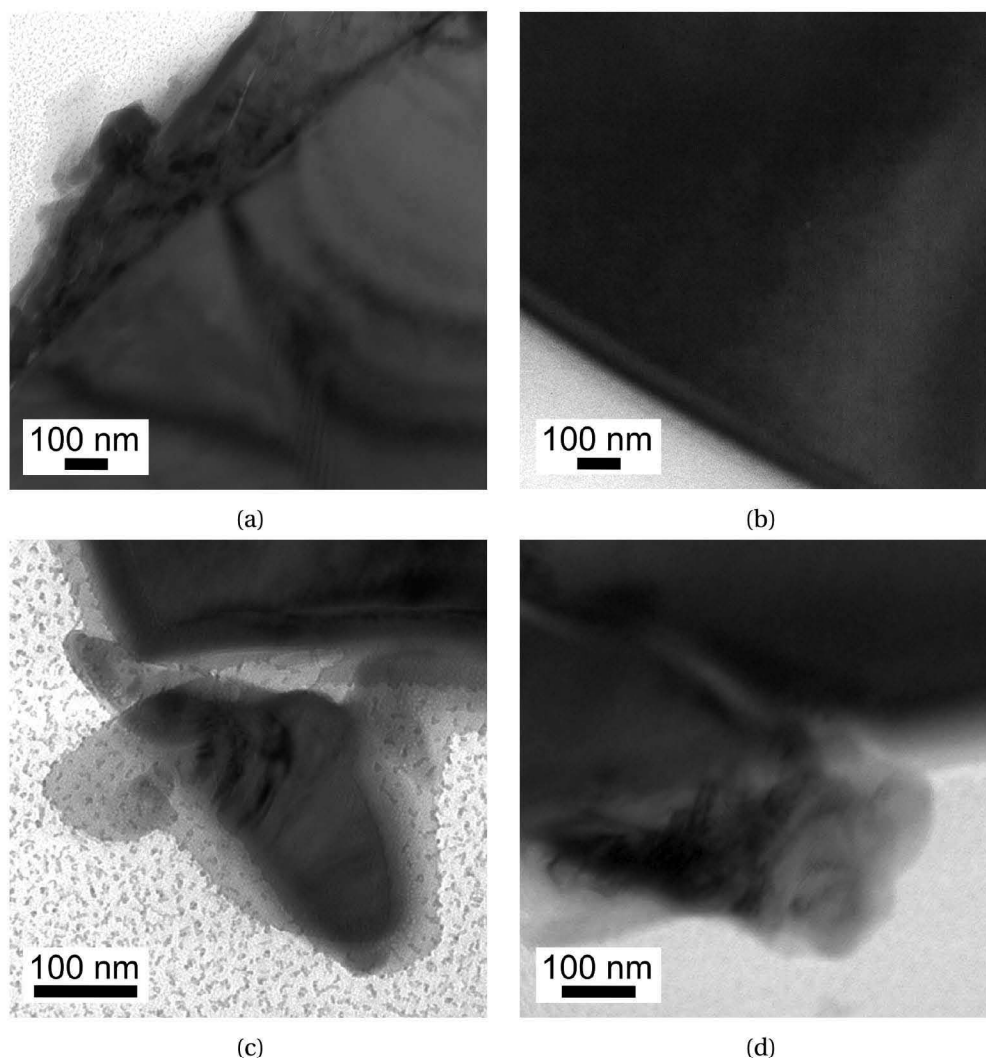
Figure 3.8: TEM BF images of alites after (a) disc mill, (b) Mc-Crone micronizer grinding. TEM BF images of small debris produced (c) disc mill, (d) Mc-Crone micronizer grinding

3.3.2 Annealing

The effect of annealing duration and temperature on the crystalline structure of pure C_3S is shown in the X-ray diffractograms in Figure 3.9. No significant structural modification of the C_3S could be observed, neither for the duration nor the temperature of annealing. However the treated samples exhibit slightly sharper peaks, which can be attributed to a reduction of the density of crystal defects.

In the case of alite, the XRD results show a modification of the monoclinic peak after annealing. The peaks begin to enlarge and split and the effect is more marked for longer duration of thermal treatment and higher temperature Figure 3.10. It seems that a transition from monoclinic M3 to the monoclinic M1 began. There is no complete transformation and most probably
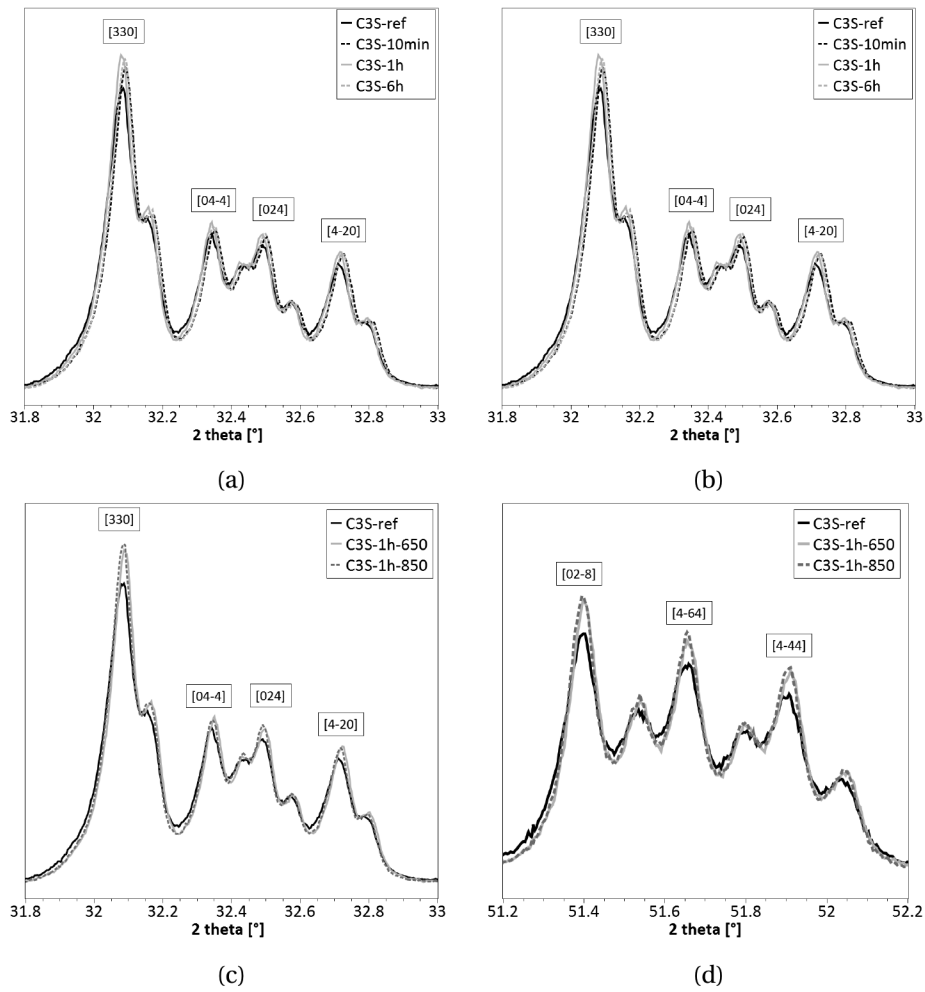
Figure 3.9: Effect of the annealing on the crystal structure of C_3S, (a) and (b) for the duration at 650 °C, (c) and (d) for 1 h at 650 °C and 1 h at 850 °C

the peaks express a combination of the two polymorphs. This transition can be explained be the migration of the foreign ions during annealing and the monoclinic polymorph M3 is not stabilized anymore. For longer duration of thermal treatment, a complete transition of the monoclinic to triclinic is possible[91].

Rietveld refinement of the different alites show a diminution of the alite content and an increase in periclase content with duration of thermal treatment (Figure3.11), which confirms a reduction of the magnesium incorporated in alite. Attempts were done to quantify the amount of M3 polymorph transformed to M1 polymorph with thermal treatment duration, but no clear tendency was observed. This difficulty to quantify the two polymorphs is due to the complexity of doing Rietveld analysis on these structures.

To confirm the observed structural changes in the annealed samples, [29]Si MAS nuclear magnetic resonance (NMR) spectra were acquired on the annealed at 650 °C C_3S. Generally, no
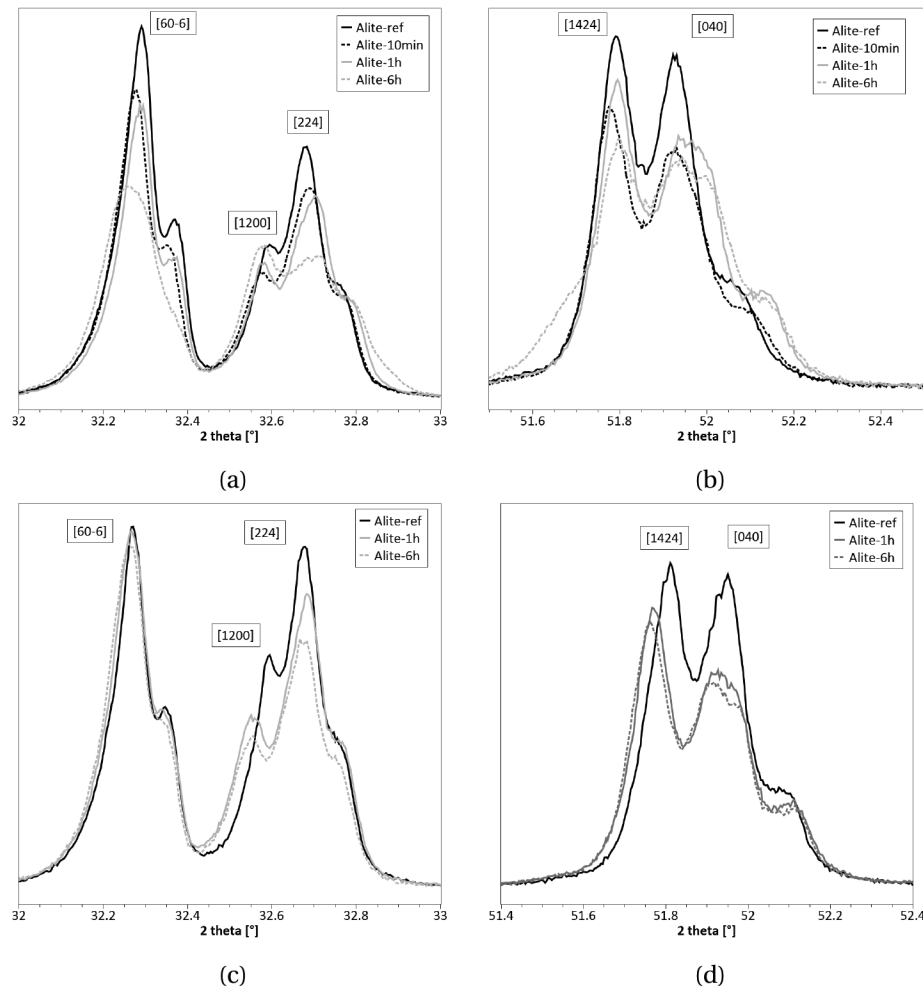
Figure 3.10: Effect of the annealing on the crystal structure of alite, (a) and (b) for the duration at 650 °C, (c) and (d) for the duration at 850 °C.

change in peak position (chemical shift) for the different C_3S samples are observed, instead some variations in line width. A clear decrease in line width is observed, going from the reference sample to the annealed samples, reflecting an improvement in the degree of crystallinity (structural order) caused by the annealing process. However, no difference between the three annealed samples C_3S is observed in the spectra. A line-narrowing effect is also observed for the alite samples where it is possible to differentiate between the different annealed samples in the spectra. The decrease in intensity of the peak at -71 ppm relative to the -74 ppm peak reflects a partly transformation from the monoclinic M3 form into the M1 form. The more pronounced differences in the spectra of the annealed alite samples may reflect effects from the ionic impurities and potentially that a reorganization/ordering of these occurred, which also induced the phase transformation.
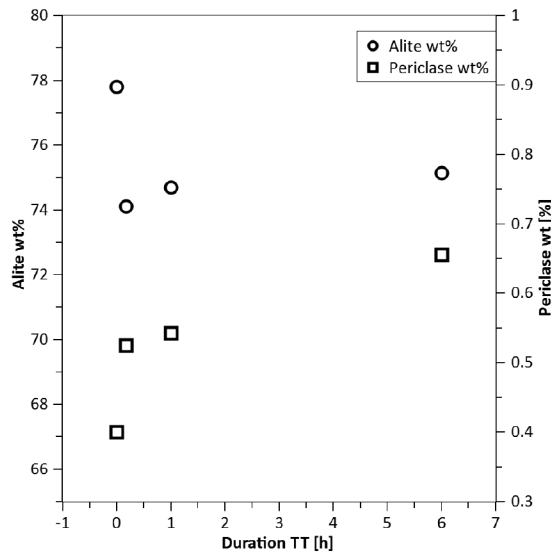
Figure 3.11: Periclase content in the alites before and after thermal treatment at 650 °C.

TEM lamellas of C_3S and alite samples were prepared to study the distribution of defects after synthesis, after grinding and after the annealing. After the first heating and quenching, there are already a lot of defects in the structure as can be seen in Figure 3.12.

Different types of defects are visible, indicated by numbered arrows. Arrows numbered 1 indicate grain boundaries, identified by the very different grey levels either side (different crystallographic orientations). Number 2 indicates twin boundaries, occurring as pairs of lines with strong fringes. Number 3 indicates antiphase boundaries (which is a type of stacking fault): there are always several fringes surrounding them and they can change direction. Number 4 indicates phase transformation dislocations – which appear when there is a mismatch in the lattice. The identification of the different defects follows Williams and Carter[33] and Amelinckx[96]. The defect types identified above result from displacive transformations, which are typical for samples undergoing polymorphic transitions[96]. On quenching from 1600°C to room temperature, C_3S undergoes 7 polymorphic transformations.

After grinding (Figure 3.13 and Figure 3.14) the same types of defects are observed inside the grains. In addition, at the grain edges, there is a region about 50 to 200 nm thick where the many different grey levels indicate a high density of defects, but these could not be characterized further. This layer forms due to impacts between particles during the grinding procedure. Alite only undergoes one polymorphic transformation, due to the presence of ions, thus less lattice defects are expected. However the presence of ions induces lattice strains due to the substitution of calcium and silicon by magnesium and aluminium respectively. As already observed in Figure 3.8, the damaged layer at the grain edge is not continuous all over the grains.
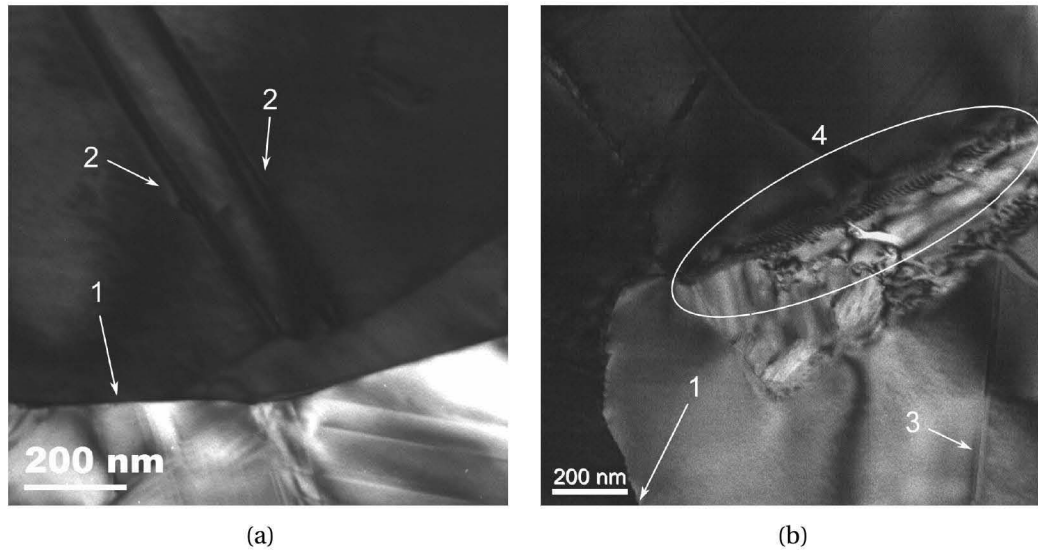
Figure 3.12: TEM images of C_3S, (a) and (b) after synthesis.

After annealing, a reduction of the defect density is observed. The damaged layer at the surface has largely disappeared. Defects are still present in the inner part of the grain, but at a lower density. In the case of alite, a recrystallization is observed (Figure 3.14). Further EDX analyses were done to observe any change in the dopant distribution, which revealed no drop in the ions concentration in alite sample after annealing, nor ions accumulation at the grain boundaries. Even if a polymorph modification is observed, the difference of ions content in alite is far below the detection limit of TEM and precise quantification of the variation is impossible by EDX.

Annealing brings about several modifications. First, the induction period is extended and this effect is more pronounced for a longer duration of the annealing and for higher temperatures. Second, the rate of heat evolution during the induction period is lower, with the same dependence on the duration and temperature of annealing. The longer induction period and the lower heat release can be attributed to lower dissolution rate during the slow dissolution regime. This would be expected if the annealing has the effect of reducing the defect density on the surface of C_3S grains.

Figure 3.13: Effect of the annealing on the defect density of C_3S and the duration of the induction period. Calorimetry curves of C_3S and annealed C_3S showing the effect of the duration of annealing and effect of the annealing temperature. TEM images of C_3S after grinding and after annealing 1 h at 850 °C.
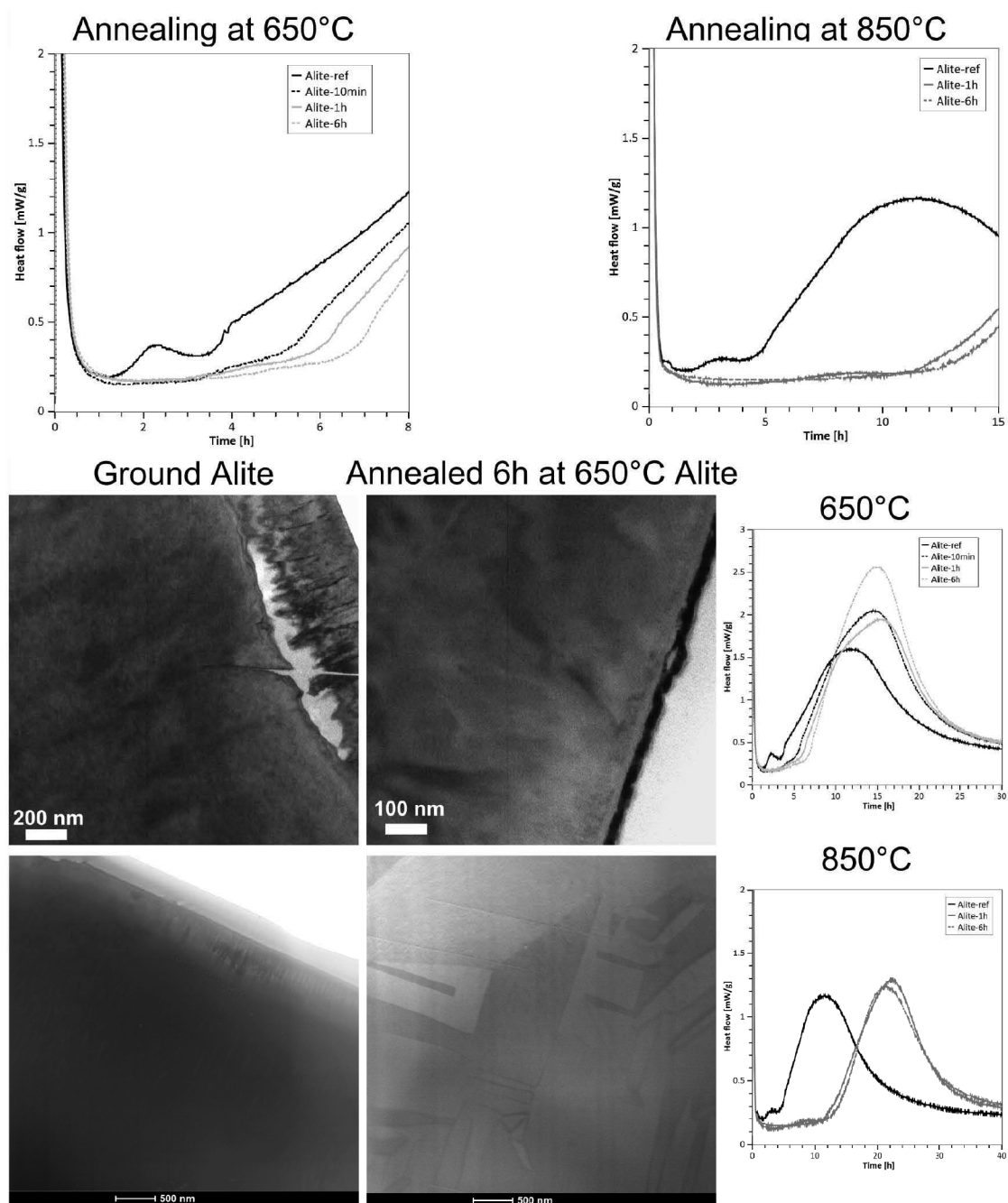
Figure 3.14: Effect of the annealing on the defect density of alite and the duration of the induction period. Calorimetry curves of alite and annealed alite showing the effect of the duration of annealing at 650 °C and 850 °C. TEM and STEM images of alite after grinding and after annealing 6 h at 650 °C.

Figure 3.15 shows the conductivity measurement of C_3S and thermally treated C_3S 1 hour at 650 °C.
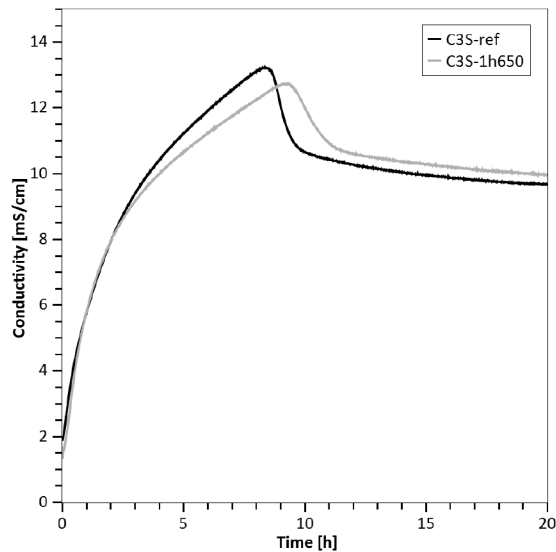
Figure 3.15: Conductivity measurement of C_3S and annealed C_3S 1 hour at 650 °C. w/c =50.

At first, there is an increase in conductivity, corresponding to the dissolution of C_3S and probably also some precipitation of C-S-H. The conductivity reaches a maximum, followed by a sharp drop, which corresponds to the precipitation of Portlandite. Measurements of the actual calcium ion concentration 37 mmol/l for pure C_3S indicated that the precipitation of Portlandite occurs at a saturation index of about 0.4, which is in good agreement with values found by Brown[97]. After the sharp drop, there is a gradual decrease in the conductivity towards the equilibrium saturation of Portlandite. There are two modifications of the conductivity curve. First, after annealing, the rate of increase in conductivity in the dissolution curve is lower indicating a slower dissolution rate. Second, the maximum conductivity is slightly reduced, suggesting a reduction in the critical supersaturation for Portlandite precipitation. These observations are consistent with the observations from isothermal calorimetry.

The repetition of the thermal treatment (1h at 650 °C) of C_3S in a chamber furnace is shown in Figure 3.16. The hydration was done in water and saturated lime solution. First, it can be observed that the hydration in a saturated lime solution has no effect on the reference sample regarding the duration of the induction period. In water, after 5 minutes of hydration the solution already reached saturation with respect to Portlandite[97]. The solution needs to reach supersaturation with respect to Portlandite precipitation to enter in the acceleration period. Since this process is limiting the reaction, the time necessary to reach the supersaturation with respect to Portlandite precipitation controls the duration of the induction period. Second, the annealed sample hydrated in the saturated lime solution exhibits a longer induction period, compared with hydration in water. Ultimately, in water, the length of the induction period is more extended than for the same annealing (1 h at 650 °C) in a tubular furnace (Figure 3.13).
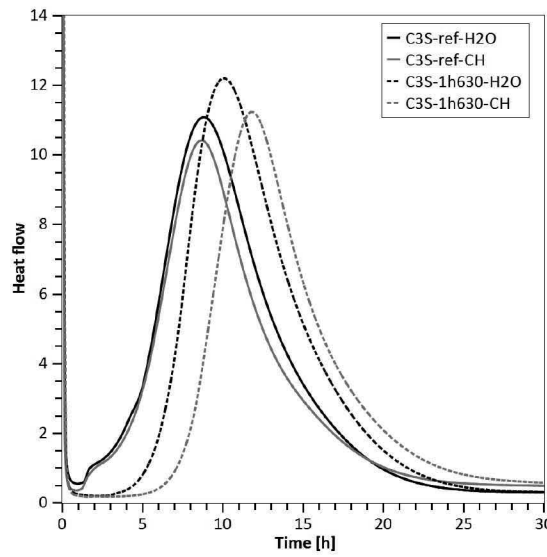
Figure 3.16: Calorimetry curves of C_3S and annealed C_3S 1 hour at 630 °C hydrated in water and in saturated lime solution

These differences shows that, even if there is a good correlation of the duration of the induction period with the duration and temperature of annealing, some differences may be observed for the same annealing in different model of furnace.

To investigate differences in microstructural development, the hydration was stopped during induction period for the pastes of C_3S after first heating, quenching and grinding (reference) and the same C_3S subsequently annealed 1h at 850 °C (annealed) as indicated in Figure 3.17.

At 1.5 hours, the reference sample is at the end of the induction period and the annealed one on the middle of the induction period. Small precipitates of C-S-H can be seen on the surface of the grains in both samples. It is also possible to see etch pits on the surface of the C_3S grains in both cases. The amounts of C-S-H and etch pits are very variable within each samples so it was not possible to draw any conclusion regarding possible differences between the samples; nevertheless the samples are broadly similar.

After 3 hours the reference sample has entered the acceleration period, while the thermally treated sample is just at the end of the induction period. The difference in the degree of hydration is clear in the micrographs. The annealed sample has not significantly changed from that at 1.5 hours. In the reference samples, on the other hand, there has been extensive growth of C-S-H, although the pitted surface of the C_3S is still visible in places.
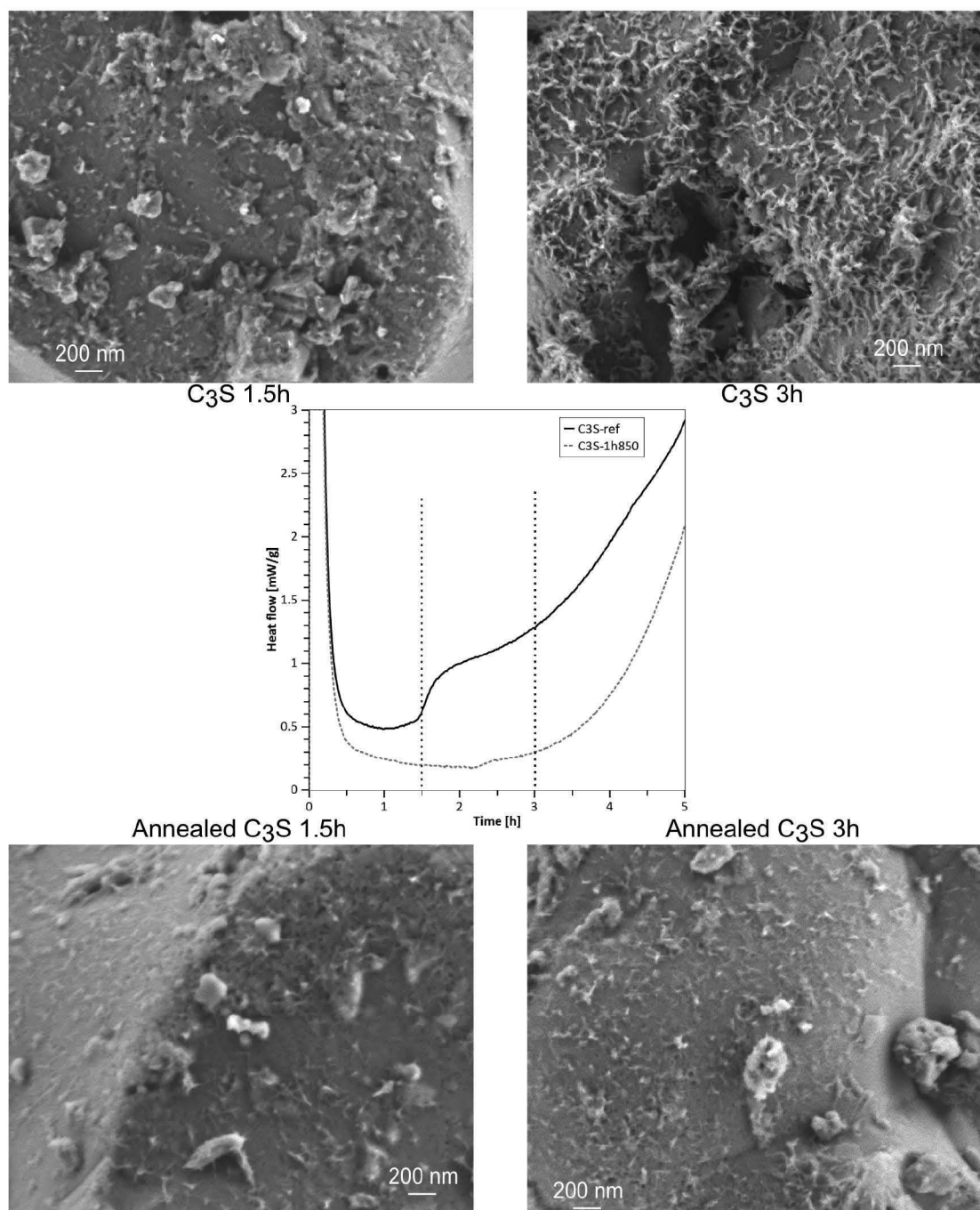
Figure 3.17: Selected hydration stops for reference C$_3$S and annealed 1 hour at 850 °C according to the calorimetry curve. SEM images in secondary electron mode of reference C$_3$S and annealed 1 h at 850 °C after 1h30 and 3h of hydration.

3.3.3 Water to cement ratio

An increase in water to cement ratio extends the duration of the induction period as shown by Figure 3.18.

w/c = 0.4   w/c = 0.8
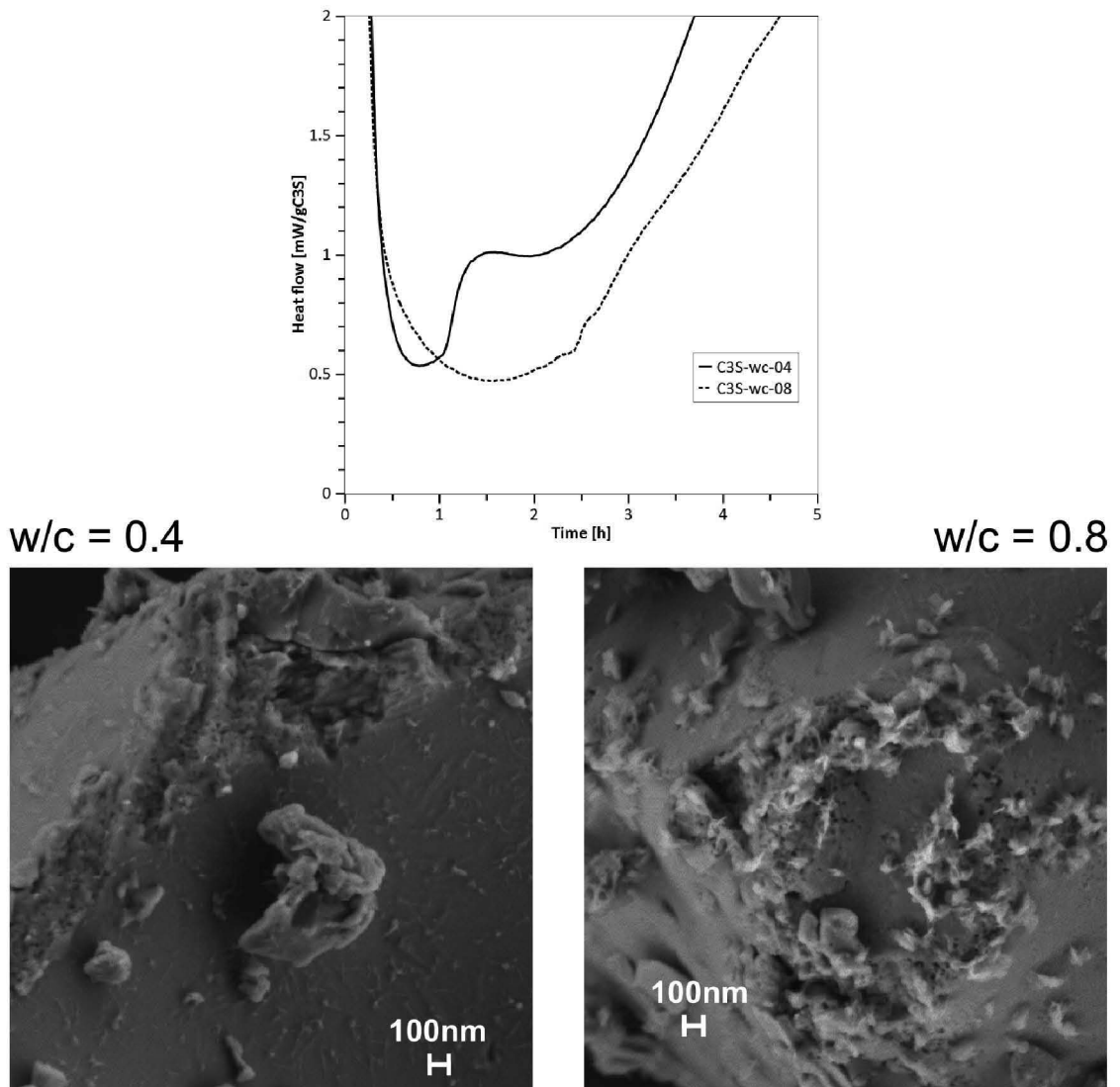
Figure 3.18: Effect of the water to cement ration on the duration of the induction period, the formation of etch pits and nucleation of C-S-H. Calorimetry curve of C_3S with a w/c of 0.4 and 0.8. SEM images in secondary electron mode of the etch pits formation and C-S-H nuclei on C_3S surfaces.

A progressive transition is observed at the beginning of the induction period. This would indicate that more time is necessary to saturate the solution and initiate the slow dissolution regime. A longer induction period is expected for more diluted system, since a larger amount of water needs to be saturated before initiating the precipitation of Portlandite. Also a larger amount of etch pits on the surface of C_3S are observed for more diluted system.

The SEM images show different nucleation rate of C-S-H for both systems. Bigger C-S-H clumps form on the surface of C_3S in the more dilute system. They seems more homogeneously distributed on the surface of the less diluted system (w/c = 0.4).

3.3.4   Doping ions

The doping ions in alite play a role in the dissolution rates of alite but also in the C-S-H formation. Figure 3.19 shows the calorimetry curves, the conductivity measurements and SEM images at 2 hours of hydration of pure C_3S, alite doped with magnesium and alite doped with zinc.

The doping ions have only a slight impact on the duration of the induction period. Magnesium increases it, while doping with zinc slightly shortens it for the lower content and has no effect for the higher content.

The conductivity measurements of the different alites show their dissolution rates. The alites doped with magnesium show fairly similar rates of increase in conductivity to the pure C_3S, perhaps slightly slower at the beginning and faster later. However, for the alites doped with zinc the dissolution is clearly more rapid. The presence of these ions in the crystal structure may change its surface energy with water and thus impact the dissolution rate. The maximum conductivity is higher in the presence of both ions, suggesting an increase in the critical supersaturation for Portlandite precipitation.

To better understand how zinc and magnesium influence the nucleation of C-S-H, SEM images were acquired at 2 hours of hydration on alites with 1.78wt% of magnesium and 1.16wt% zinc, and compared with pure C_3S. In the SEM images small clumps of C-S-H (indicated by arrows) are observed, which may originate from a single nuclei. There are also some Portlandite crystals indicated by circles. The presence of CH crystals is most probably due to the method used to stop the hydration, in this case freeze drying. For comparison, one sample was stopped by solvent exchange and much less CH crystals were observed. The nucleation density seems not to be influenced by the presence of zinc, but is affected by the presence of magnesium. In the presence of magnesium less nuclei form, but they seem to be bigger after 2 hours. The etch pit formation seems very similar in all images. Again, the number of etch pits are very variable within the surfaces from the same sample so it is not possible to draw any conclusion.
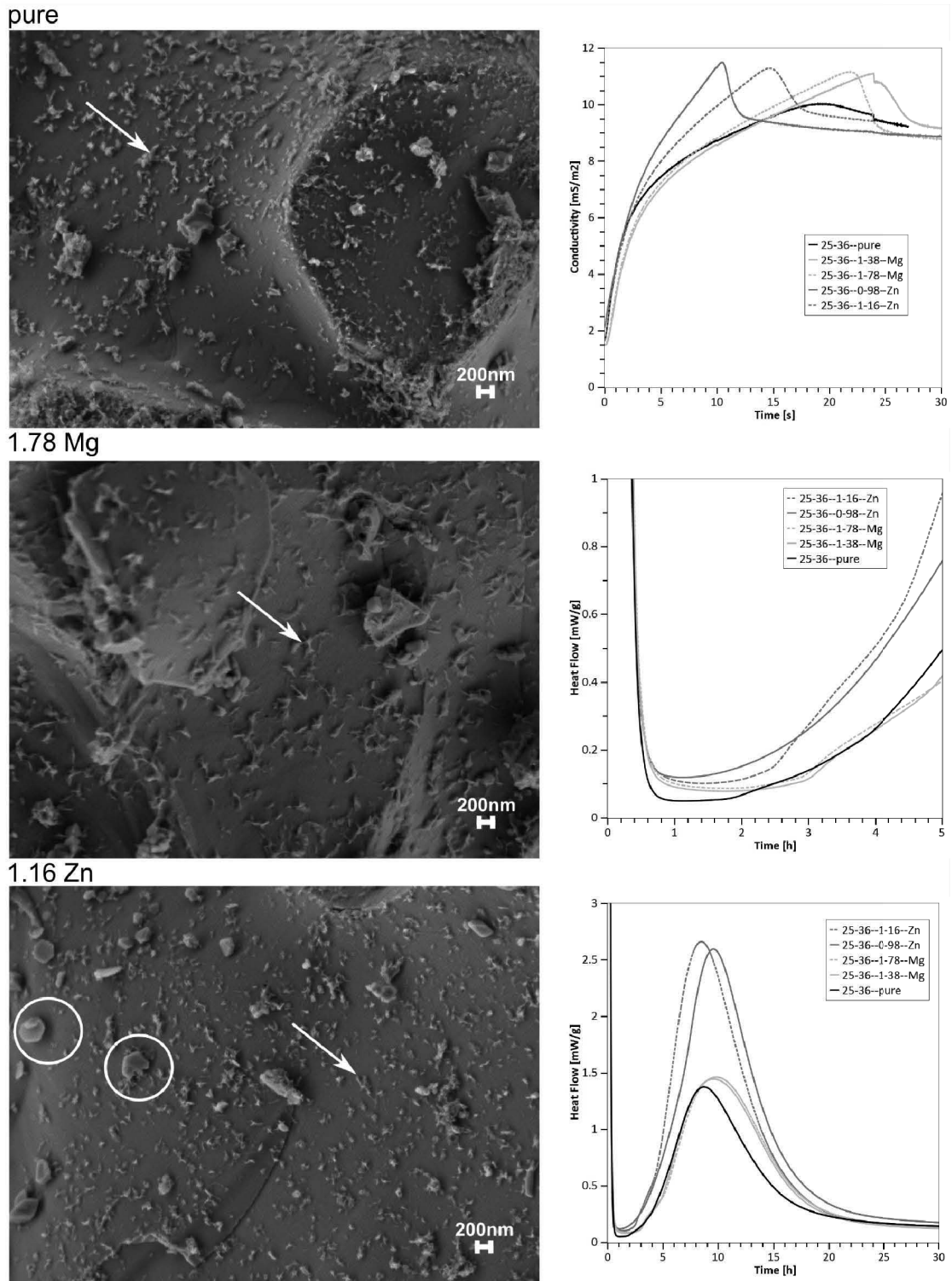
Figure 3.19: Effect of the doping ions present in alite on the duration of the induction period, the formation of etch pits and nucleation of C-S-H. Calorimetry curves and conductivity curves of pure C_3S, alites doped with MgO and ZnO. SEM images in secondary electron mode, which shows the etch pits and C-S-H nuclei formation.

3.4 Discussion

3.4.1 Defects and surface morphology

The grinding procedure induces a lot of defects and changes the surface properties of the particles, observed for alite in Figure 3.8 and Figure 3.14 and C_3S in Figure 3.13. The dry grinding produces much more debris than the wet grinding. The defect density is very difficult to quantify due to the heterogeneity of the samples and the limited observable area by TEM. In the case of alite, the grains are large (25-36 μm) compared to the observable area (5x10 μm). Even if different samples were prepared, a proper quantitative analysis is difficult. The parts of the grains close to the surface were clearly more deformed than the inner part, which is in good agreement with other studies[78–80]. The dry ground particles were more damaged than the wet ones. Small alite debris exhibited more intense deformation than the bigger particles (Figure 3.8). According to Tromans and Meech[81–84], there is a critical size to reach before substantial plastic deformation can be generated in a particle. Our observations may well support this hypothesis, because small particles were much more deformed than bigger ones. This fact may explain why C_3S particles exhibit much more damage than alite ones, because C_3S particles are much smaller. Another factor can be their different specific hardness[98], which can lead to different behavior for the rupture process during grinding.

Annealing reduces the density of crystalline defects in C_3S (Figure 3.13) and alite (Figure 3.14), mainly by removing the damaged layer close to the surface of the grains. TEM only shows 2 dimensional defects. Other point defects such as vacancies cannot be identified by TEM but a reduction in their number would also be expected. These defects also have an impact on the dissolution rate[99].

3.4.2 Hydration kinetics

The effect of these different types of damage on the hydration kinetics is mainly observed during the induction period (Figure 3.6 and 3.7). The lower the dissolution rate is, the longer the induction period is. This would be expected for samples that show a lower defect density and a lower surface roughness. As proposed by Tromans and Meech[81–84], removing smaller particles is not only removing specific surface, it is also removing highly reactive particles due to the excess of molar energy due to plastic deformation. Thus, the enhancement of dissolution rates due to the presence of the small particles is not only related to their increase in specific surface area, but also because they were highly deformed. The samples ground by disc mill followed by surface cleaning are exempt of plastically deformed, highly reactive small particles (Figure 3.6 and 3.7). Likewise, the samples ground by Mc-Crone showed a very low amount of debris and had surfaces with less microrelief (Figure 3.6 and 3.7). These two samples exhibit the same heat released during the induction period. Conductivity measurement (Figure 3.6 and 3.7) shows much slower dissolution rates these samples.

The main consequence of the reduction of defects after annealing is on the induction period (Figure 3.13). As shown by the calorimetry curves the slow dissolution regime (surface reaction controlled step) is lowered after annealing. When a saturated lime solution is used this effect of slowed down surface reaction is even more pronounced and the induction period of annealed samples hydrated in a saturated lime solution is the longest (Figure 3.16).

In the case of alites with different ions, the conductivity measurement (Figure 3.19) shows three distinct dissolution rates for the three compositions (pure C_3S, alite with magnesium and alite with zinc). The duration of the induction period (Figure 3.19) is slightly different for the three cases, and its duration follows the same trend as the conductivity measurement. It is the shortest in the presence of zinc and it is the longest in the presence of magnesium. The C-S-H formation is similar for pure C_3S and alite with zinc, while it is different for alite with magnesium. Similar observations about the different sizes of C-S-H clumps during the induction period are made on C_3S when hydrated with different w/c. When the system is more diluted, bigger C-S-H clumps precipitates on the C_3S surface while the system is still in the induction period. These observations may be inconsistent with the hypothesis that C-S-H must reach a certain size before starting to grow. Different size of C-S-H clumps are observed at the end on the induction period for the different systems. However, a lot of C-S-H nuclei are observed during the induction period, but only some of them can start to grow during the induction period, explaining the different sizes observed.

3.4.3 Etch pits formation

The SEM pictures do not indicate a major change in the density of etch pits between C_3S and annealed C_3S (Figure 3.17). However, since the distribution of etch pits on the surface of the samples is very heterogeneous, the SEM observation are not inconsistent with the hypothesis that there is a reduction in dissolution rate due to a lower number of defects. Furthermore, bigger and deeper etch pits are observed on the surface of C_3S in a higher w/c (Figure 3.18). The observed etch pits are mainly located at the edges of grains, were there is and higher defect density. Etch pits can nucleate all over the surface and not necessarily at the intersection of a defect with the surface[77]. Etch pits with a size range in the order of atoms in depth are expected to form on a perfect surface[77], but they are not visible on the SEM images. The etch pit nucleation can be similar during the fast dissolution period on both untreated and annealed samples. For the annealed samples, slow dissolution regime corresponding to the lateral step propagation is much slower due to the reparation of the surface and the reduction of defects. This is well supported by the conductivity measurement (Figure 3.15), where the slope of the rapid dissolution is similar in both samples, while the slope of the slow dissolution regime is lower for the annealed samples.

These observations are in good agreement with the geochemical theory of dissolution proposed for cement by Juilland et al.[5]. The surface property of the particles controls the dissolution rate during the induction period and the C-S-H nucleation is a consequence of the

alite dissolution. They also reveal that the dissolution in two steps developed by Lasaga and Luttge[54] for cleaved surfaces is not as simple in the case of ground particles. As pointed out by Ardvidson and Luttge[69] the history of the mineral surface plays an important role in the transition between the two regimes. In C_3S hydration, Nicoleau et al.[56] measured two distinct dissolution rates for pure C_3S and alite and two different transitions were observed. For ground particles, a lot of kinks and step are already present on the surface of the mineral and contribute to the dissolution kinetics since the beginning of the reaction. Due to the presence of this roughness, the dissolution rate in the slow dissolution regime is not strictly related to the number of etch pits created. The combined effect of the pre-existing surface roughness and the different transition between the two regimes accounts for the duration of the induction period. The defect density and surface morphology is strongly related to the duration of the induction period, while the etch pits formation seems more related to the solution composition.

3.5 Summary

This chapter focused on the duration of the induction period and parameters that influence it. The main findings are listed below:

- This work suggests that the controlling mechanism during the induction period is the dissolution rate. As the defect density and/or the surface roughness are reduced, the duration of the induction period is extended.

- The grinding procedure changes the defect density and surface structure of the particles.

- The effect of the different grinding procedures and its consequent defects density and surface morphology on the hydration kinetics is a longer induction period for particles exempt of debris and with low amount of surface roughness.

- The annealing of quenched and ground C_3S does not change the crystal structure, while for alite a transition from M3 to M1 polymorph seems to occur. However the defect density is lowered after annealing in both cases, resulting in an extension of the duration of the induction period.

- For samples having different chemical composition (alite doped with zinc and magnesium) distinct dissolution rates are measure for the different samples composition. Also different nucleation rates and sizes of C-S-H is observed.

- The etch pit formation is difficult to quantify due to their heterogeneous distribution along the surface and their small size barely visible with the SEM. Bigger and deeper etch pits are observed for more diluted systems. In the case of annealing, no real difference in etch pits formation are observed on annealed samples. Similar etch pits formation on alites with different composition are also observed.

4 Main hydration peak

Part of the results of this chapter on doping ions has been accepted for publication in the Journal of the American Ceramic society.

This chapter presents the results of the development of hydrates on alite grains during acceleration period. SEM is used to follow the evolution of the coverage of the surface and the hydrates morphology during acceleration period. STEM is used to characterize the morphology and composition of C-S-H from the beginning of the acceleration period up to 24 hours. The observed microstructure evolution is compared with the kinetics of the hydration followed by isothermal calorimetry. The influence of the water to cement ratio and the specific surface area on the hydration kinetics and the resulting microstructure changes are studied as well as the impact of the doping ions present in alite.

4.1 Literature review on the acceleration period

4.1.1 Theories about acceleration period

The mechanism causing the acceleration of hydration is still debated because two mechanisms occur simultaneously at this stage: the precipitation of Portlandite and the rapid growth of C-S-H. The controversy comes from which induces which.

Study of C-S-H seeds[53] indicates that, when more C-S-H is added to the system, the induction period is shorter. NMR study of Bellman[41] shows that dimeric silicon is detected only from the end of the induction period, when C-S-H starts to grow, indicating that there is a change in the C-S-H composition between the induction period and the acceleration period, that trigger the onset of the acceleration period.

The geochemistry approach[5;67] indicates the onset of the acceleration period is due to the massive precipitation of Portlandite, when the supersaturation degree is reached.

Bullard and Flatt[7] have examined the hydration kinetics through kinetic cellular automaton simulations to test two hypothesis controlling the induction period, the protective membrane and the geochemistry approach. Their simulations showed that both mechanisms can lead to a normal hydration kinetic curve of C_3S and changes in solution composition that are consistent with experimental data from literature. The difference between the two mechanisms is when the precipitation of Portlandite is suppressed. In the case of geochemistry approach, the induction period last for hours, since dissolution of C_3S is in steady state condition and the driving force for growth of C-S-H is not sufficient. In the case of the protective membrane approach, this has no implication on the duration of the induction period, because the dissolution of the passive layer is triggered by the C-S-H precipitation. The authors concluded that only in the geochemistry approach the precipitation of Portlandite is a trigger for the acceleration period.
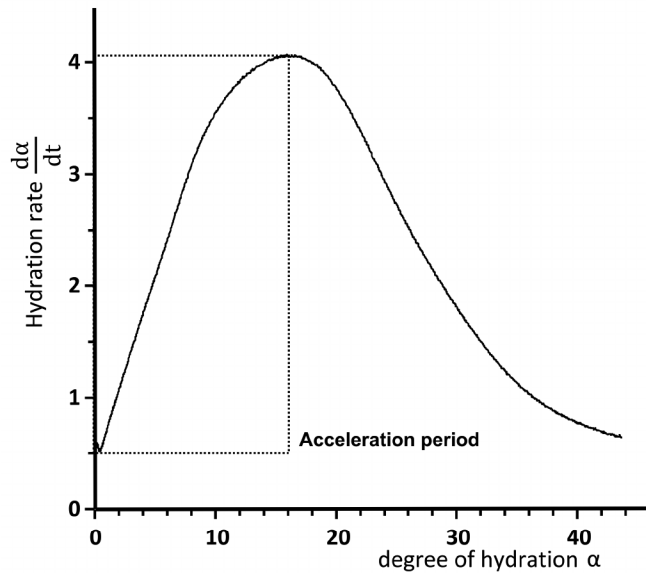
Figure 4.1: Evolution of the hydration rate versus the degree of hydration for an alite paste with particles <25 μm, hydrated at 20 °C with at w/c of 0.4.

Once the acceleration period starts, authors agree that the growth of hydrates controls the kinetics[6,9]. Gartner and Gaidis[100] suggested that the reaction is autocatalytic and its kinetics are limited by the growth of C-S-H rather that Portlandite. Assuming that C-S-H growth is autocatalytic, the kinetics during the acceleration period is proportional to the surface area of C-S-H. Further experimental work done by Garrault et al.[51,52] also indicates that the acceleration period is governed by the the heterogeneous nucleation and growth of C-S-H.

During the acceleration period, an almost linear dependency is observed between the hydration rate and the degree of hydration, which implies an exponential dependence of the degree of hydration with time[100]. The rate is defined as the derivative of the degree of hydration (α) with time and can be extracted from a calorimetry curve.

The fraction of C_3S hydrated can be expressed as per equation 4.1:

$$\frac{d\alpha}{dt} = k\,\alpha^{\frac{2}{3}} \qquad\qquad (4.1)$$

The exponent $\frac{2}{3}$ can be related to the fact that the surface area of C-S-H is proportional to the two thirds power to its mass. Figure 4.1 illustrates the evolution of the hydration rate versus the degree of hydration for an alite paste with particles <25 μm, hydrated at 20 °C with at w/c of 0.4.

4.1.2   C-S-H growth and morphology

The mode of growth of C-S-H is still not clear, whether it is by aggregation of nanoparticles[101] or by growth at the ends of large and defective sheets of silicate[102].

Gartner[102;103] proposed that C-S-H grows as large defective flakes, which can be connected together by their ordered part. Integration of equation 4.1 gives a t^3 dependence of α with time. Gartner[103] suggested that the only way to have such a high order of dependence was with a constant nucleation process. According to this model, a tobemorite sheet grows in 2D from the solution. A second sheet can nucleate on the first one, then grow and thicken the first sheet. Following the heterogeneous nucleation, this process ends with the sheet-like structure. The branching region may have a tobemorite-like structure and the growing region may be amorphous (Figure 4.2).
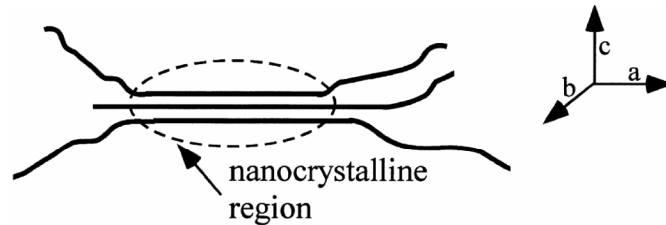
Figure 4.2: Schematic represenation of C-S-H structure, from Gartner et al.[102].

In hydrated C_3S pastes two different morphologies of C-S-H are observed. One type of product is found in between grains, in the pore space. The second type of product is found within the original unhydrated grain. Consequently, the two different morphologies are referred to outer product (OP) and inner product (IP) respectively[104–106]. In general, OP is textured and for pure cement or C_3S pastes has elongated shape called fibrils. IP is more homogeneous and seems to be composed by particles. Figure 4.3 shows an illustration from Richardson[106] of the two different products in a pure C_3S paste, hydrated for 8 years at 20 °C with a w/c of 0.4.
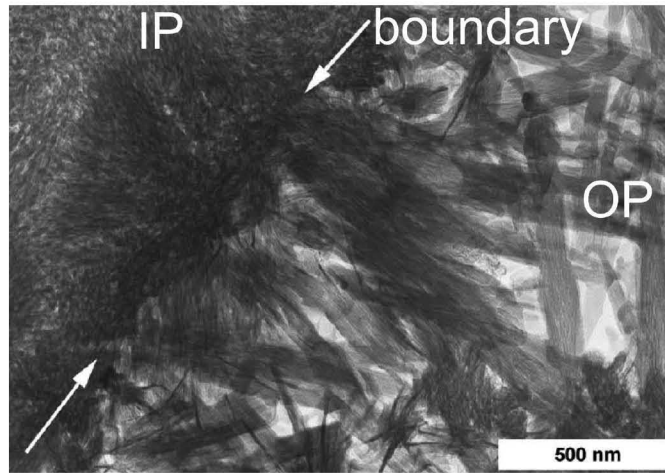
Figure 4.3: Illustration of Inner product and Outer product in C-S-H. The arrows indicates the boundary between IP and OP. Image from Richardson[106].

4.1.3 Parameter influencing the growth of C-S-H

Effect of the specific surface area

The particle size distribution is known to play an important role on the heat development profile in the calorimetry curves. Costoya[28] extensively studied this effect, a decrease of the acceleration slope and maximum heat released were observed for larger particles size, as indicated by Figure 4.4.
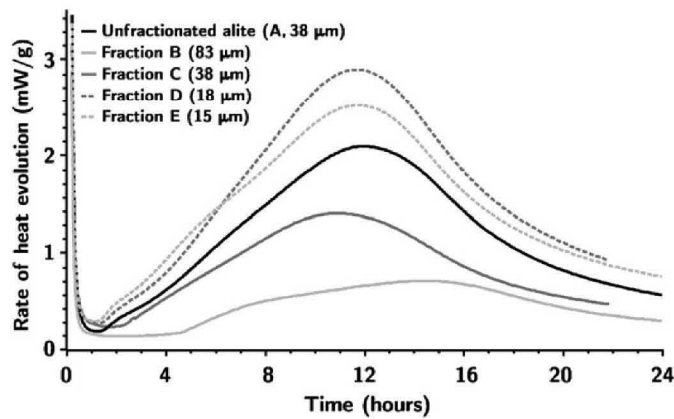
Figure 4.4: Impact of the PSD on the calcorimetry curve of alite as studied by Costoya[28] and Bishnoi in[107].

The microstructure development was also affected by the differences in particles size distribution: a thinner C-S-H rim was observed to form at the maximum heat in samples with coarser particles size. Garrault[108] observed that for a same degree of hydration, the thickness of C-S-H rim produced around particles is thicker for finner ones.

Filler effect

The filler effect is the enhancement of the hydration reaction in the presence of non-hydraulic filler[109], which provides nucleation sites. Finely ground limestone is a filler, but not totally inert, since some chemical reaction can occur with aluminate[1] (not the case here).

At early age, the presence of limestone accelerates the hydration of C_3S by providing extra surfaces for nucleation[110–112]. SEM study showed that during hydration surfaces of both C_3S and limestone are covered by hydrates[113]. It is also evident that on the limestone surface many more nucleation sites were present, showing that limestone acts physically by increasing the available surface for nucleation. At later age, limestone may reacts with alumina present in clinker to form hemicarbonate and monocarbonate[114;115].

Effect of doping ions

Changes in reactivity due to the foreign ions are often attributed to the polymorph, but once they are in solution they can also influence the nucleation or growth of hydrates. C-S-H is known to show a wide range of solid solution and morphologies and foreign ions may enter in the structure[116–118]. This has been notably reported in the case of aluminum[119;120], and zinc which can replace Si-tetrahedron[121;122] and increase the C-S-H chain length[123].

There have been numerous studies on the effects of these ions on hydration kinetics and strength development[19;124–129]. Some studies tried to relate the difference in hydration kinetics to the type of polymorph[126–130]. However, inconsistencies were observed between polymorph, type of ions and reactivity. Other authors concluded that the type of ions was determining rather than the type of polymorph[124;125].

Stephan et al.[21;22;131] investigated the effects of magnesium, aluminum and iron on the crystal structure and hydration kinetics of alite. They observed that pure C_3S is triclinic, iron and aluminum stabilized triclinic polymorphs, and magnesium the monoclinic polymorph. Doping of alite with magnesium had almost no effect on hydration kinetics despite the change in polymorph. Doping with iron had a strong effect on hydration kinetics (decreasing the main hydration peak), despite retaining the triclinic structure. Rather than the hydration kinetics being related to the type of polymorph, the modification of hydration kinetics appeared to be better related to the hydrate morphology. Alites doped with magnesium showed similar hydration products to pure C_3S, while alite doped with aluminum and iron showed shorter and more compact C-S-H and Portlandite crystals were smaller.

4.1.4 Transition from acceleration period to deceleration period

As discussed above, it is agreed that the nucleation and growth of C-S-H is controlling the reaction rate during the acceleration period. However, it is not clear what is causing the transition from the acceleration to the deceleration period.

Garrault et al.[51;108] suggested that C-S-H grow around particles of C_3S until covering the whole surface. The C-S-H rim reaches a certain thickness, which is dependent of the particle size distribution of C_3S. The C-S-H rim formed acts as a diffusion barrier, limiting further the growth by the diffusion of species through the layer.

Bishnoi[107] and Costoya[28] argued against a diffusion control mechanism, because due to the different thickness of C-S-H rim produced around grains, simulations of the deceleration period with a diffusion controled mechanism revealed one order of magnitude in the diffusion coefficient between different fractions of particles[107]. This would indicate that a large variation in the transport properties of C-S-H exist for a same alite with different particles size distribution, which would be unlikely. Also no such change was observed for the alites through different experimental techniques. Instead, they proposed that the loosely packed C-S-H grows quickly outwards grains and starts to densify when it impinge with C-S-H growing from other grains[107]. This hypothesis is well supported by TEM observation of cement where low density products are observed at early age[132].

Kirby and Biernacki[133] showd that a densifying growth of C-S-H itself cannot explain the deceleration period. Their experiments on varying the water to cement ration in pure C_3S, alite and cement paste shows very little dependence of the maximum heat with the space available for C-S-H to grow. They agreed with the fact that a low density C-S-H product forms at first and then slowly start to densify, but they disagree on the fact the impingement between grains causes the transition.

The growth of C-S-H is limited, but the reason remains unclear. The main arguments proposed to explain this limitation are the lack of space, the transition to a diffusive regime, the consumption of small particles and the lack of water. There are aspects to all these hypothesis which do not correspond to the experimental observations.

4.1.5 Numerical modeling

Several mathematical models have been developed to predict hydration kinetics and microstructure development. These are covered in detail in the review of Thomas et al.[8].

Thomas[134] proposed new modelling tools for the nucleation and growth kinetics of tricalcium silicate hydration. Firstly, the standard Avrami[135;136], also refereed as Johnson-Mehl-Avrami-Kolmogorov, JMAK, model was described. This approach considers that a fixed volume is filled by a new phase by nucleation and growth process, for which nucleation is spatially random and the linear growth rate in any direction is constant. At later stage, the growing regions will impinge each other and form a common interface, which is not growing anymore. When this model is applied to C_3S hydration, it is implicitly assumed that the diffusion of species is not rate limiting, which is the case for the first hours of hydration. The process is defined by the dimensionality of the growth, n, and the effective rate constant. In the standard Avrami model n should be 4, for the three-dimension growth and constant nucleation rate.

The main objection to the use of the JMAK model to describe cement hydration is that there is no random nucleation in the volume. For the early hydration of cement, it is well established that C-S-H nucleates on surfaces. The hydration product may grow along surfaces and outward into the pore solution and the product from adjacent particles eventually coalesce. This process is analogous to phase transformation in a polycrystalline material. The model derived by Cahn[137], referred as the boundary nucleation and growth, BNG, described this process. This approach considers a fixed volume containing single planar boundaries and assumes that nucleation can occur only on the boundary. The nucleation is randomly distributed and the growth is constant in any directions. The impingement occurs between two nuclei growing on a same surface or from two nuclei growing from adjacent surfaces. The process is defined by two independent growth rates, the rate at which the nucleated boundary area transforms and the rate at which the nonnucleated grains between boundaries transforms.

C_3S hydration was studied by the two models by different workers[107;134;138]. Thomas[134] observed that the JMAK model is unable to account for the effect of the water to solid ratio and the particle size distribution. A change in the w/c would affect the distribution of nuclei in the JMAK model and increase the amount of hydration at the peak, while the effect of w/c on the degree of hydration at the peak measured in paste showed almost no changes. In the boundary nucleation and growth model, the distribution of nuclei is not affected by the w/c since they are constrained to form only on the particle surfaces. The situation is reversed for the effect of the PSD. In the JMAK the distribution of nuclei is not affected by the size of the particles, while it has a strong effect on the hydration kinetics. In the BNG model, the size of the particles change the surface for nucleation and thus influences the distribution of nuclei.

Bishnoi[107] studied the hydration kinetics of alite with different particle size distribution with the two models discussed above using the modeling platform μic[139]. Evaluation of the simulations for alites with the different PSDs, showed that only impingement from neighborhood particles can induce deceleration, even if lateral impingement slows down the reaction. No deceleration occurred for any of the fractions simulated. This was because the volume of a uniformly dense C-S-H formed at the peak was insufficient to cause impingement between growing particles.

It was proposed that a low packing density product was growing and filling the space between particles and this packing density increases with the advancement of the reaction[107]. A modification of of the nucleation and growth theory was proposed to induced sufficient impingement between particles, with the following hypotheses:

- The surface of the particles is only partially covered by hydrates

- The availability of C-S-H surface controls the growth of product

- Fresh outer product has a low packing fraction

- C-S-H grows uniformly over its exposed outer surface

- The rate of increase of packing fraction of C-S-H is assumed to decrease linearly with density

Figure 4.5 shows a schematic illustration of the nucleation and growth mechanism with a densification of product during growth.
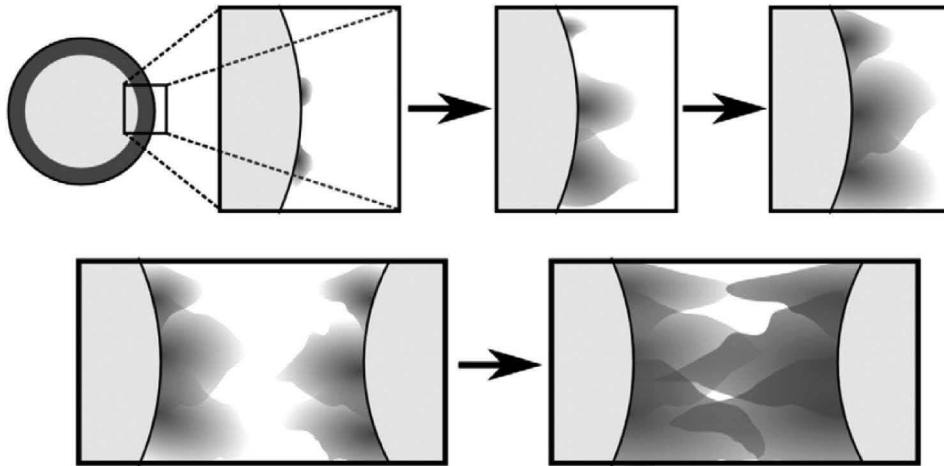
Figure 4.5: schematic illustration of the nucleation and growth mechanism with a densification of product during growth proposed by Bishnoi. Image taken in[107].

The same hydration kinetics of the alites divided in different fractions were simulated with this new model and good correspondance was obtained. Further, it was observed that for finer particles, the growth rate was lower that for larger particles. It was stated that to have enough impingement between hydrates from neighborhood particles, a lower rate of growth was required for particle with closer neighbor (finer particles).

More recently Bishnoi[140] tested different shapes for the growth of products with equations similar to the ones from Avrami[135;136] and Cahn[137]. The results indicated that the rule of impingement cannot be applied for nuclei growing on the surface of different substrate particles. Simulations provided by Cahn equation are correct only if unrealistic parameters are used. It was then proposed[140] that the nucleation of phases that occurs in the free space at the same time as growth occur on the surface of the substrate can be modeled using the rule of impingement if the remaining untransformed volume is known.

Garrault and Nonat[51] developed a model to describe the growth of C-S-H on the surface of C_3S. Based on AFM observations[141], C-S-H was described to grow by oriented aggregation of three-dimensional identical units. C-S-H formation consisted of a heterogeneous nucleation leading to the formation of clusters followed by their growth. The growth was split in two terms, the growth along the surface and the increase of cluster thickness. The model takes into account three parameters: the number of growth clusters, the parallel growth and the

perpendicular growth. The simulated images of C-S-H growth showed good comparison with AFM observations. However, these experiments and simulations were carried out on systems with a w/c of 50.

4.2 Systems studied

The impact of water to cement ratio on the acceleration period was studied with C_3S batch 2. The two water to cement ratio studied were 0.4 and 0.8.

The effect of annealing on the acceleration period was studied on C_3S batch 1. The annealing procedure was described in chapter 3.

The effect of the specific surface area is studied on alites batch 1 and 2. The different grinding procedures were described in chapter 3. Batch 1 of alite was separated in different particle size distributions and thus has different specific surface areas. Batch 2 was ground with different grinding procedures resulting in powders with different specific surface areas, despite sieveing the powders between 25 and 36 μm. For all samples, the specific surface area was calculated from the particle size distribution assuming spherical particles.

Blends of C_3S with limestone were studied in a collaboration with Elise Berodier, whose project is focused on the filler effect. The purpose of this study is to examine the impact of limestone on early hydration of pure C_3S, without aluminium. Kinetic aspects are evaluated as well as the development of the microstructure.

The effect of the doping ions on the hydrates development was studied on the alites with magnesium and zinc.

4.3 Parameters influencing the acceleration period

4.3.1 Annealing

Figure 4.6 shows the calorimetry curve of C_3S after annealing.

The annealed samples enter the acceleration period with a steeper slope than the freshly ground ones. The height of the peak after annealing is only slightly modified for C_3S. Except for the sample treated for 10 minutes at 650 °C, all peak intensities of annealed samples are higher. There is no clear explanation for such an observed increase. The position of the main hydration peaks is modified too, due to the combined effect of the lengthening of the induction period and a steeper slope of acceleration period. The deceleration stage appears similar for all samples. After the heat peak all the curves converge.

A reduction of the bump and a steeper acceleration slope is observed for annealed samples. This bump was attributed to a massive precipitation of Portlandite (endothermic peak) by
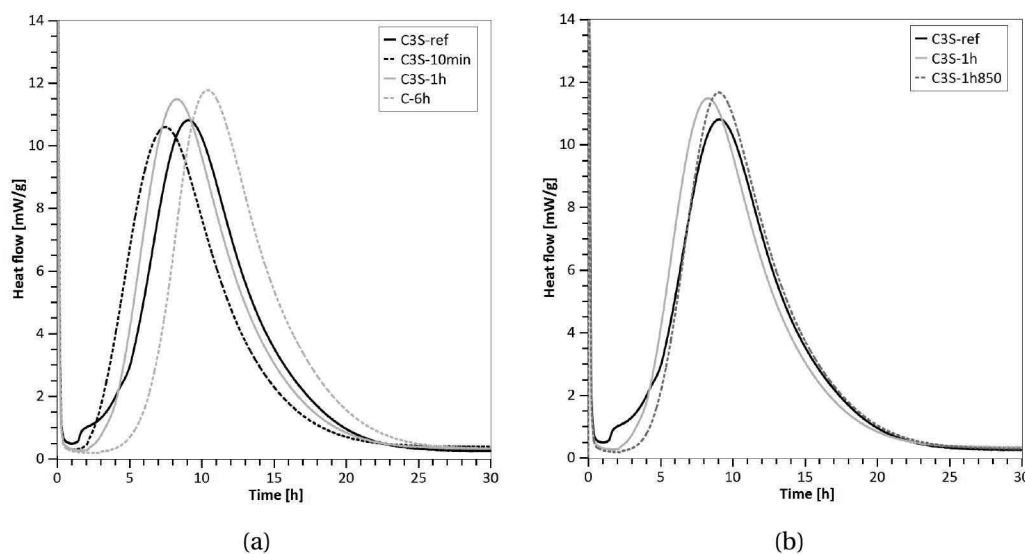
Figure 4.6: Impact of the annealing on the hydration kinetics of C_3S, (a) effect of the duration of annealing at 650 °C and (b) for 1 h at 650 °C and 1 h at 850 °C.

Damidot et al. [142;143]. We rather believe that the precipitation of Portlandite at the end of the induction period lowers the undersaturation of the solution with respect to C_3S and so allows the rate of dissolution to increase again, but, if the rate of growth of C-S-H cannot keep up, the rate of the reaction will slow down again. In the conductivity experiments, the calcium concentration reaches more rapidly the critical degree of supersaturation of Portlandite for the reference C_3S (first heated, quenched and ground), since the dissolution rate is higher during the induction period, leading to a massive precipitation of Portlandite at the end of it (bump). When the dissolution rate is lower, it takes longer to reach the critical supersaturation (Figure 3.15 of chapter 3). On the other hand, the period of rapid C-S-H growth seems to occur sooner (steeper acceleration) after the precipitation of calcium hydroxide at the end of the induction period for the annealed samples. It is proposed that the longer induction period allows more and better organized C-S-H nuclei to form, so rapid growth of C-S-H now coincides with Portlandite precipitation, which leads to a disappearance of the bump and a steeper slope in the acceleration period.

To investigate differences in microstructural development, the hydration was stopped for C_3S after first heating, quenching and grinding (reference) and the same C_3S subsequently annealed 1h at 850 °C (annealed) during the acceleration period (6 hours) and at the maximum heat (9 hours).

By 6 hours (Figure 4.7), both samples are in the middle of the acceleration period. Extensive growth of C-S-H has taken place in both cases. The morphology of the C-S-H seems to be the same for both samples. The backscattered images at low magnifications (Figure 4.7) reveal a clear difference in the number of nuclei of calcium hydroxide present. The Portlandite precipitates as clusters surrounding unreacted grains of C_3S. A higher number of clusters is

seen in the reference sample than the annealed one. Analysis of several images indicated there are 36 clusters per mm^2 for the reference C$_3$S and 25 clusters per mm^2 for annealed C$_3$S. This observation is consistent with the conductivity results (Figure 3.15), which showed that the supersaturation of Portlandite at the point it starts to precipitate is lower in the annealed sample. A lower supersaturation should lower the number of nuclei forming.

At the maximum heat (9 hours), for both samples the surface of C$_3$S is covered by hydrates and the morphology of the C-S-H seems to be the same (Figure 4.8). The backscattered images at low magnifications (Figure 4.8) shows that cluster are larger than at 6h. It is interesting to note that a clear difference in morphology of CH clusters is observed between samples. In the annealed sample, many small clusters are present among large clusters, while in the reference sample only large clusters are visible. Analysis of several images indicated there are now around 45 clusters per mm^2 for both samples.

The SEM study indicates that the overall morphology of C-S-H is similar in C$_3$S before and after annealing. There is a noticeable effect on the number of CH clusters, which is higher during the acceleration period in the quenched, reference sample, corresponding to a slightly higher supersaturation before precipitation seen by conductivity. The number becomes equivalent at the maximum heat flow, due to the appearance of numerous small clusters.

Figure 4.7: SEM images in secondary electron mode showing surface of C_3S and annealed 1h at 850 °C C_3S pastes during the acceleration period. Calorimetry curve of C_3S. Results show that the surface of grain is partially covered by hydrates during acceleration period and less CH clusters are observed in the case of annealed C_3S.
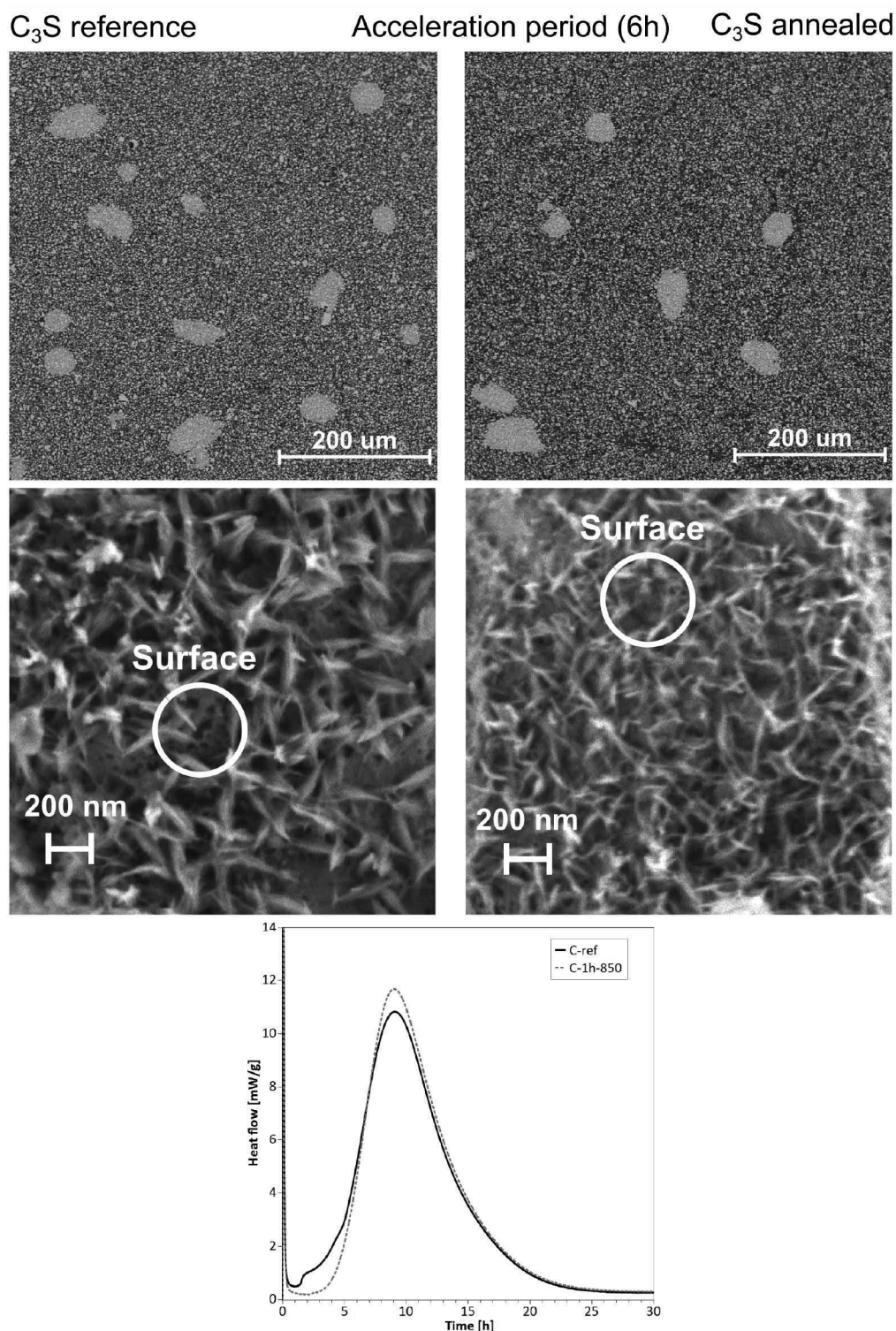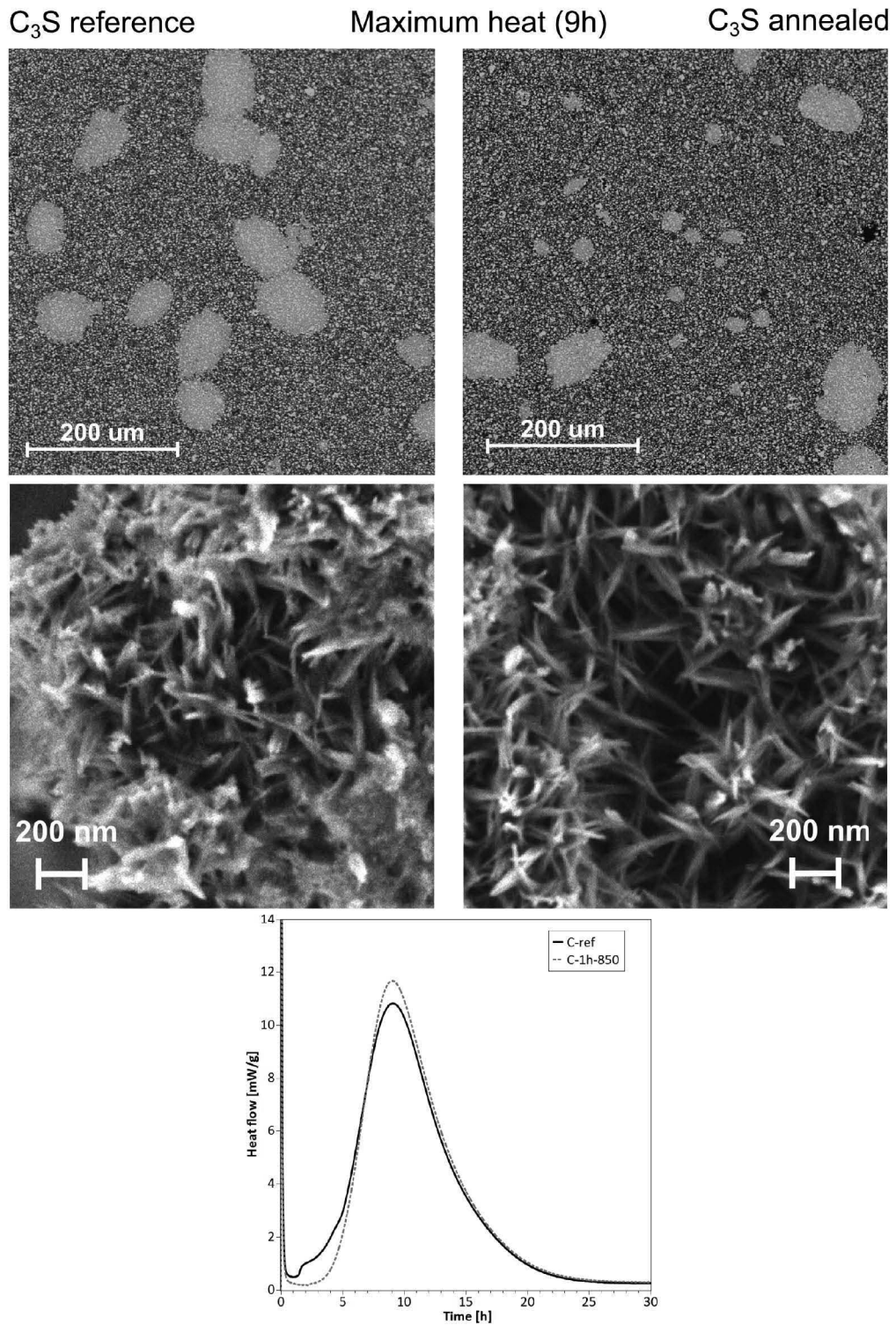
Figure 4.8: SEM images in secondary electron mode showing surface of C_3S and annealed 1h at 850 °C C_3S pastes during the acceleration period. Calorimetry curve of C_3S. Results show that the surface of grain is partially covered by hydrates during acceleration period and less CH clusters are observed in the case of annealed C_3S.

4.3.2 Water to cement ratio

The increase of the water to cement ratio has an effect to increase the space between particles. According to Bishnoi hypothesis[107], as there is more space between particles for the growth of hydrates, it is expected that its outward grow would be faster. The effect of the increase of the w/c on the slope of the acceleration period in calorimetry curve is little as indicated by Figure 4.9. The observed differences are an increase of the duration of the induction period, already discussed in the previous chapter, the reduction of the bump at the end of the induction period and an slight increase of the maximum heat flow.

Surface coverage and needles length

In order to compare the surface coverage and the hydrate morphology at the same degree of hydration during the acceleration period, hydration was stopped after 5 h 30 for the paste at w/c 0.4 and 6 h 30 for the paste at w/c 0.8. During the acceleration period, SEM images (Figure 4.9) show that the surface of the paste with the higher w/c is less covered by hydrates and there are deeper etch pits on the surface of the grain. Also C-S-H needles seem more agglomerated than for paste with a lower w/c.

The hydration was also stopped at the moment of the maximum heat flow. At this stage, their degree of hydration was 23% for the w/c of 0.4 and 29% for the w/c of 0.8. At the maximum heat flow, the surface is completely covered by hydrates and it is not possible to see the surface anymore (Figure 4.10).

To evaluate the thickness of the C-S-H rim and the length of the C-S-H needles at the maximum heat flow, STEM images on grains cross-sections were acquired (Figure 4.10). The images show that needles seem longer in the case of higher w/c and the thickness of the C-S-H rim is larger. From the images, the length of the C-S-H needles was measured. Needles were considered as the outer part of the C-S-H rim as indicated in Figure 4.11. Needles were measured on many images and result indicates that the sample with the higher w/c has longer needles (Figure 4.11). Measurements were repeated after 24 h and after 7 days of hydration, to see if needles continue to grow from the maximum heat flow. It seems that the length of the needles continue to increase from the peak, but very slowly (Figure 4.11).
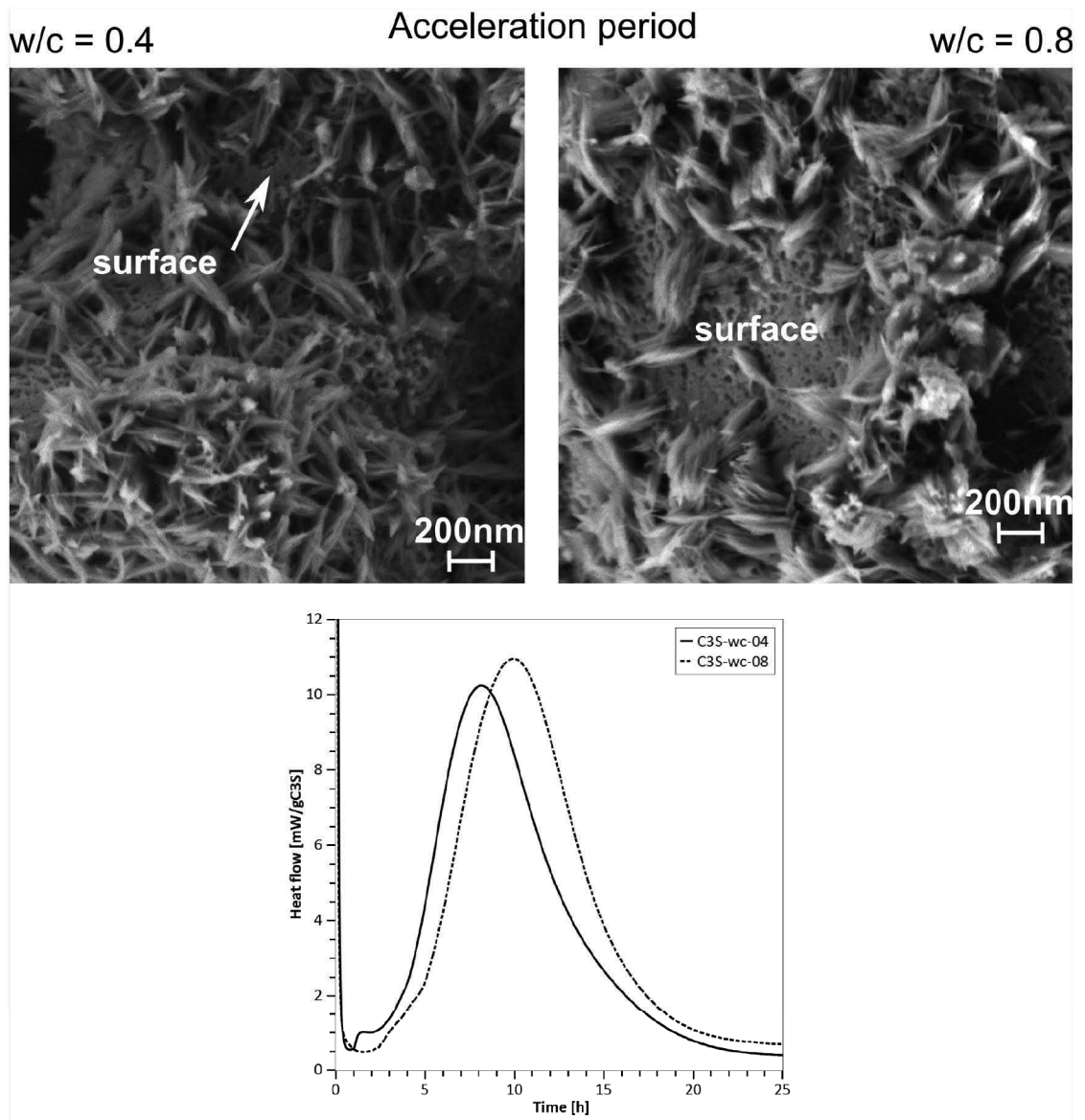
Figure 4.9: SEM images in secondary electron mode showing surface of C_3S pastes prepared with w/c 0.4 and 0.8 during the acceleration period. Calorimetry curve of C_3S. Results show that the surface of grain is partially covered by hydrates during acceleration period.
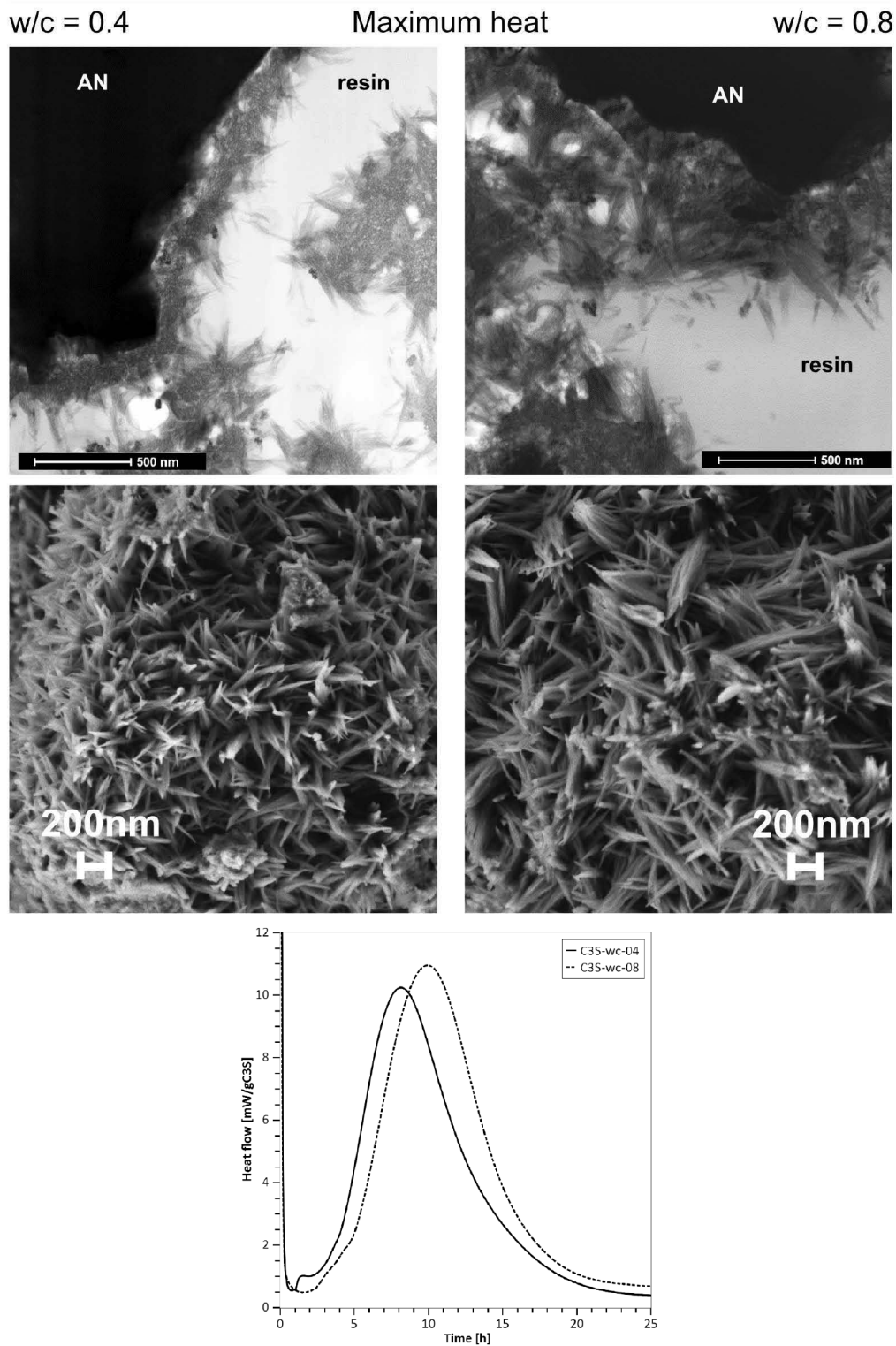
Figure 4.10: SEM images in secondary electron mode showing surface of C_3S pastes prepared with w/c 0.4 and 0.8 at the maximum heat flow. Calorimetry curve of C_3S. STEM images of C_3S at the maximum heat flow. AN indicates anhydrous C_3S grains and resin indicates the resin used to prepare the samples. Results show that the surface of grain is completely covered at the maximum heat flow. The C-S-H layer is thicker for sample with a higher w/c.
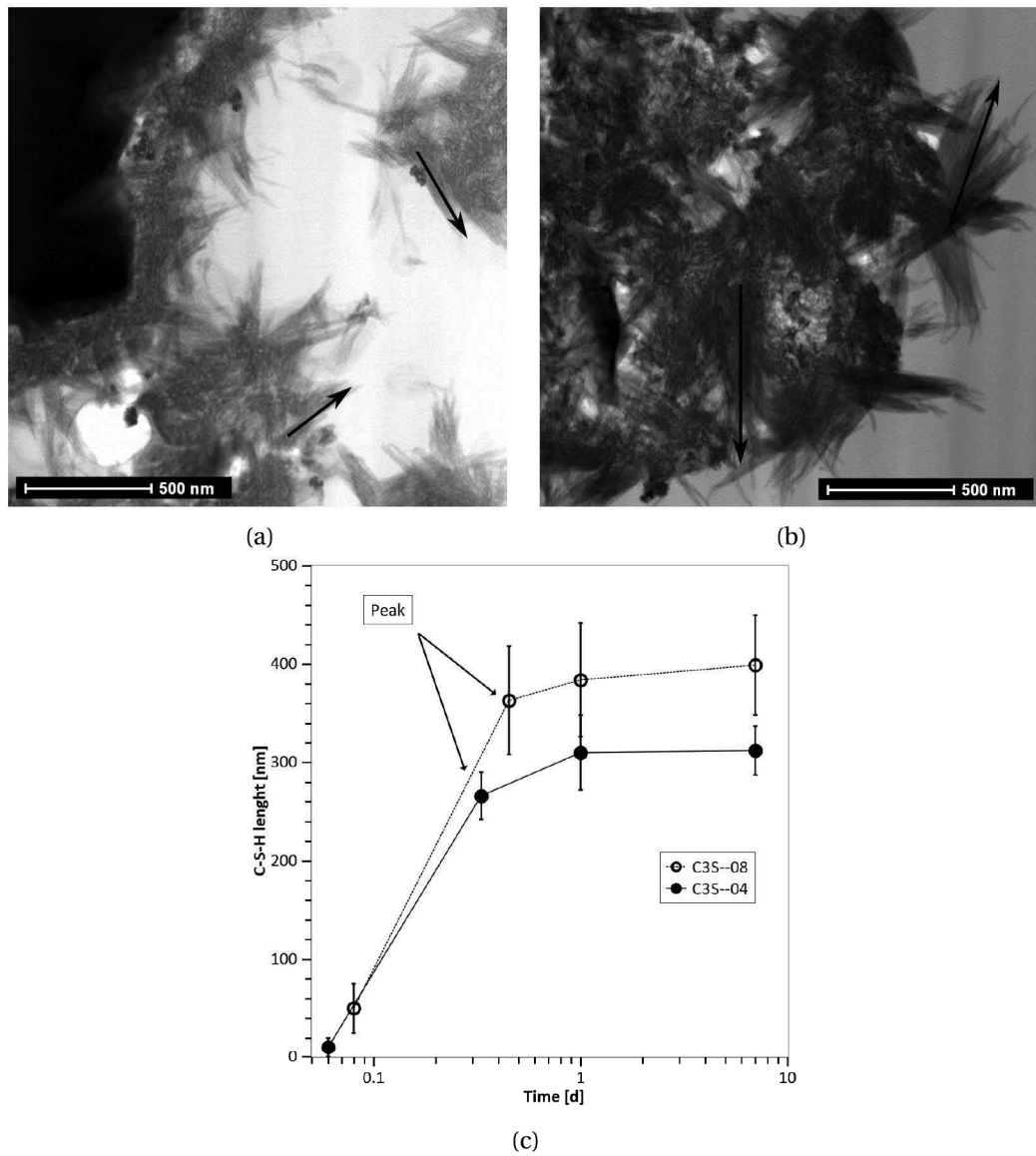
Figure 4.11: Details on C-S-H needles for measurement. (a) w/c 0.4, (b) w/c 0.8 and (c) Measurement of the C-S-H length in nm. The error bar represents the dispersion of measurements in several images.

Morphology of C-S-H

The evolution of the microstructure of pastes was studied by STEM from acceleration period to 24 h (Figure 4.12). It can be observed that the thickness of the rim of C-S-H around particles increases with time for both samples.

C-S-H with a low packing density is observed to form during the acceleration period. Impingement between C-S-H growing from different C_3S grains is already observed for the low w/c sample. In the case of higher w/c, little impingement seems to occur.

At the maximum heat flow, for both samples C_3S grains are completely covered by outer-product, which is characterized by intermixed needles. A thicker layer of C-S-H is observed for lower w/c, while longer needles are observed for higher w/c. In term of morphology, the outer-product in both samples shows a fibril morphology. A gap is observed between C-S-H and anhydrous grain. The needles started to fuse to form a dense layer, between the surface of the grains and the outward needles. It is proposed that at the peak a transition occurs between the formation of the outer-product and the initiation of the formation of the inner-product.

After 24h, the inner-product is visible and the gap between the grains and C-S-H layer disappears. Inner-product for C_3S look like a dense packing of globules, as described by Richardson[106]. The inner-product in the lower w/c sample looks isotropic, while for the higher w/c sample it shows fibrils. The surface of the grain is severely etched. A densification of the product is also observed with time. The C-S-H is more compact at 24 h. It is proposed that the presence of this gap , results from the growth of needles only at the tip at the beginning of the acceleration period. Once C-S-H start to form inner-product, the gap is filled and disappears.
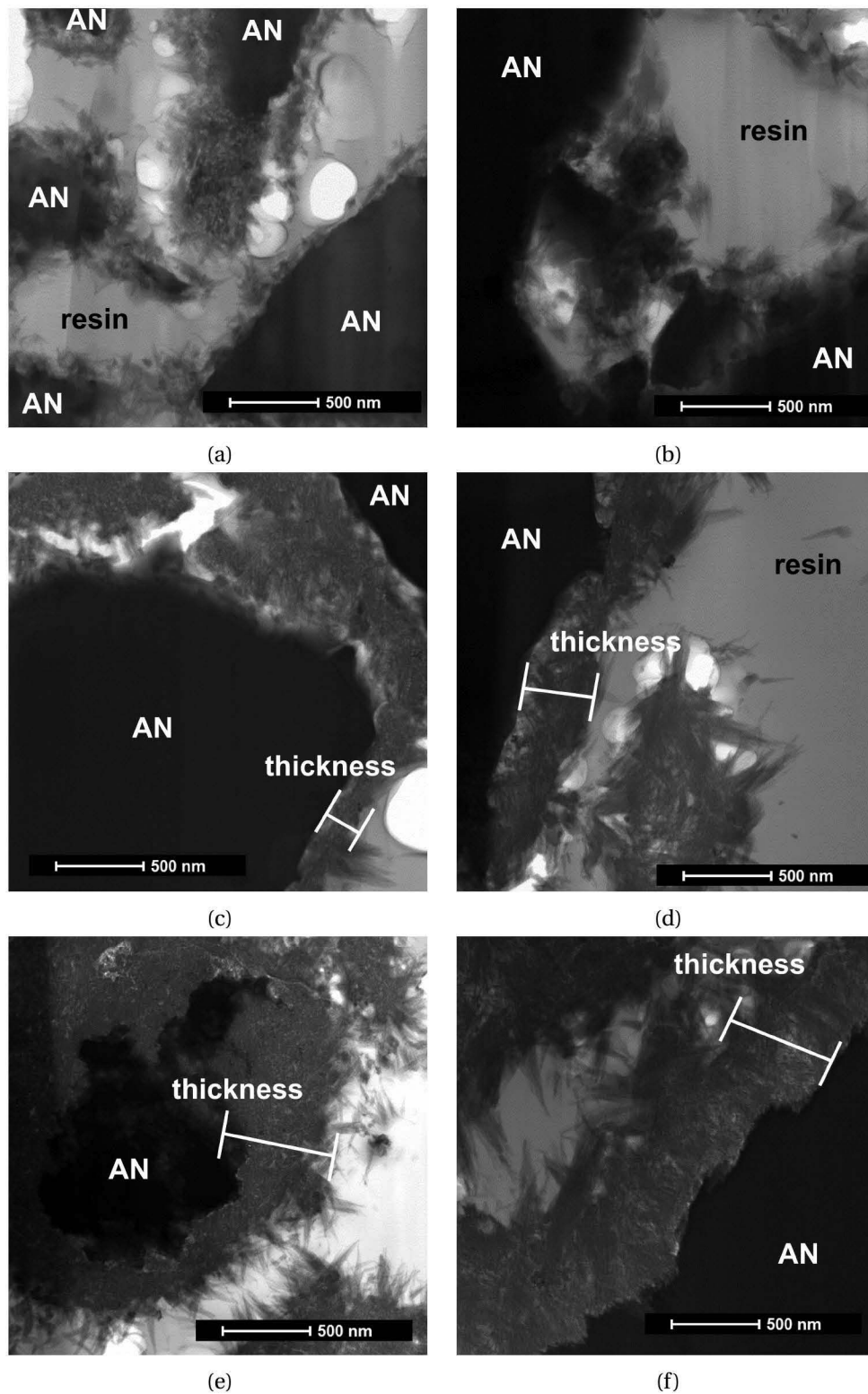
Figure 4.12: STEM images of C_3S (a) w/c 0.4 after 5 h 30, (b) w/c 0.8 after 5 h 30, (c) w/c 0.4 after 8 h, (d) w/c 0.8 after 10 h, (e) w/c 0.4 after 24 h, (f) w/c 0.8 after 24 h. AN indicates anhydrous C_3S grains and resin indicates the resin used to prepare the samples.

75

4.3.3 Limestone

Hydration kinetics

The hydration kinetics of the system with 40 wt% replacement of limestone is compared with C_3S pastes with a w/c of 0.4 and 0.8, in order to compare the dilution effect and the addition of calcium due to the presence of limestone. Figure 4.13 (a) shows the calorimetry curves and Figure 4.13 (b) shows the cumulative heat for the three systems. Curves are normalized to g of C_3S.

(a)   (b)
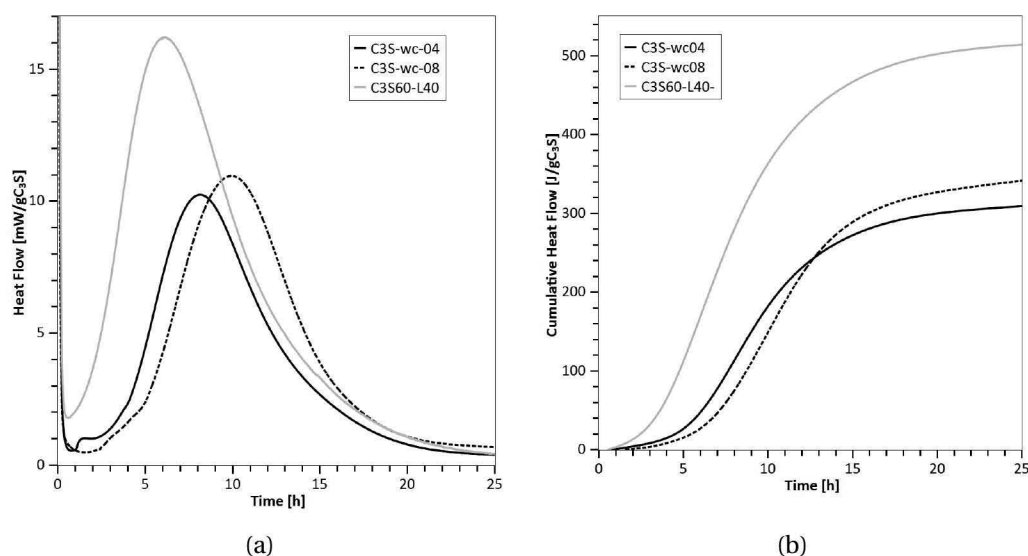
Figure 4.13: (a) Calorimetry curves and (b) Cumulative heat of C_3S at w/c of 0.4 and 0.8 and C_3S blended with 40% limestone.

The presence of limestone increases the slope of the acceleration period and the height of the maximum heat, resulting in an increases of the cumulative heat for the sample with limestone compared to the pure C_3S pastes. The filler effect of limestone increases the dissolution of C_3S in order to precipitate C-S-H on both surfaces (limestone and C_3S grains).

Attempts were made to follow the evolution of C_3S dissolution and Portlandite formation by in-situ XRD during the first 24 hours of hydration. The technique gives relatively good results for the C_3S dissolution, but it was not possible to follow the Portlandite formation for two reasons. First, the Portlandite has a preferential orientation which distorts the measurements. Second, in C_3S paste, Portlandite precipitates as clusters which are randomly distributed in the microstructure. Since the shape and distribution of these clusters vary from one sample to another, no precise measurement of the Portlandite by XRD was possible.

Regarding the consumption of C_3S, there is first a delay corresponding to the induction period in the calorimetry curve. Then, there is a fast consumption of anhydrous corresponding to the main hydration peak. Finally, there is a slow consumption corresponding to the period of

low activity in the calorimetry curve after the main hydration peak (Figure 4.14). A delay in the consumption of C_3S is observed for the higher w/c, but once it starts, the consumption is similar to lower w/c samples, in good agreements with the calorimetry results. In the case of limestone, the consumption of C_3S is very fast from the beginning .
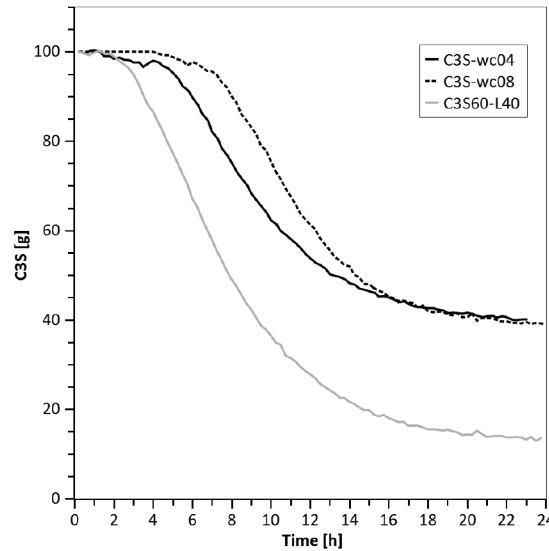
Figure 4.14: C_3S consumption in the different samples determined by in situ XRD.

The degree of reaction was calculated from both calorimetry curves and in-situ XRD results for the consumption of C_3S. In calorimetry, the degree of hydration is calculated by the ratio of the specific heat produced at time t [J/g] and the specific reaction enthalpy at 100% of reaction. In the case of alite reaction, the the specific reaction enthalpy at 100% of reaction is 514 J/g[1]. From XRD the degree of reaction is the amount of C_3S consumed at any time. Figure 4.15 shows the degree of hydration calculated from calorimetry curves (Figure 4.15 (a)) and from in-situ XRD (Figure 4.15 (b)).

Both methods give good correspondence for the calculation of the degree of hydration of C_3S paste with a w/c of 0.4. For the paste with a w/c of 0.8 and the paste with limestone, the degree of hydration from 10 hours is underestimated by XRD compared with calorimetry. It is most probably due to the formation of CH clusters, which can perturb the detection of C_3S signal. As these clusters engulf anhydrous particles, the higher amount of CH present the more perturbed is the signal of C_3S. Determination of the Portlandite content of the three system is given in the next chapter (chapter 5).

(a)

(b)
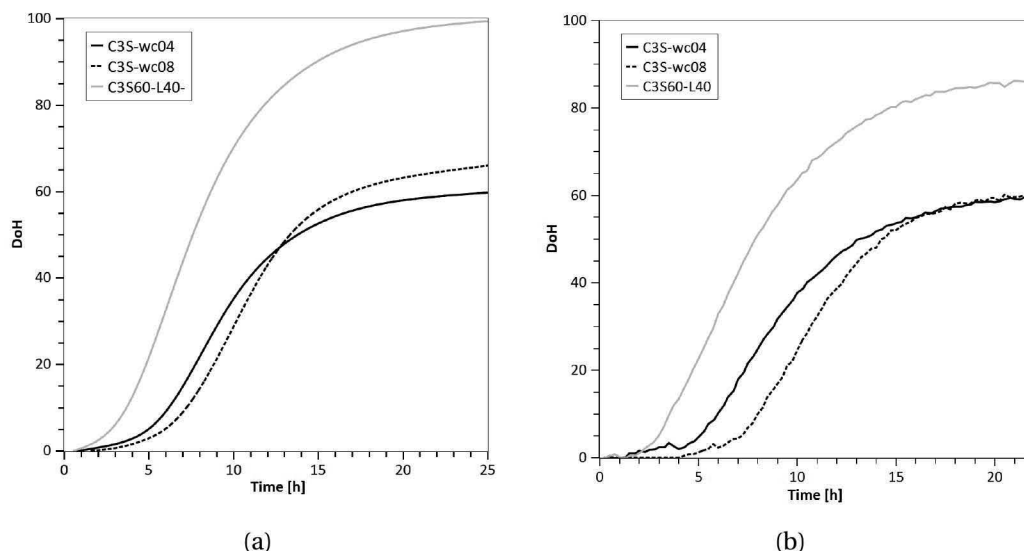
Figure 4.15: Degree of hydration of C_3S at w/c of 0.4 and 0.8 and C_3S blended with 40% limestone calculated from (a) Calorimetry curves and (b) In-situ XRD.

Morphology of C-S-H

SEM images of the sample containing limestone were acquired during the acceleration period, to observe the nucleation of C-S-H on the C_3S and limestone surfaces. Figure 4.16 shows the surface of the C_3S grain (4.16 (a)) and limestone grain (4.16 (b)), for the mix of 60% C_3S and 40% limestone after 3 h of hydration.

Obviously, C-S-H precipitates preferentially on limestone surface. The needles are well oriented and in a larger quantity. On the C_3S surface, C-S-H needles seem thicker and are heterogeneously dispersed. It is also observed that the C_3S grain undergoes severe dissolution. In comparison with the pastes of C_3S in Figure 4.9, in the presence of limestone, C_3S undergoes more dissolution. It is coherent with the hydration kinetics (Figure 4.15), which showed faster dissolution of C_3S in the presence of limestone. It is proposed that limestone increased the nucleation rate of C-S-H, due to a crystallographic effect, thus stimulating the dissolution of C_3S. Limestone provides also calcium during hydration.
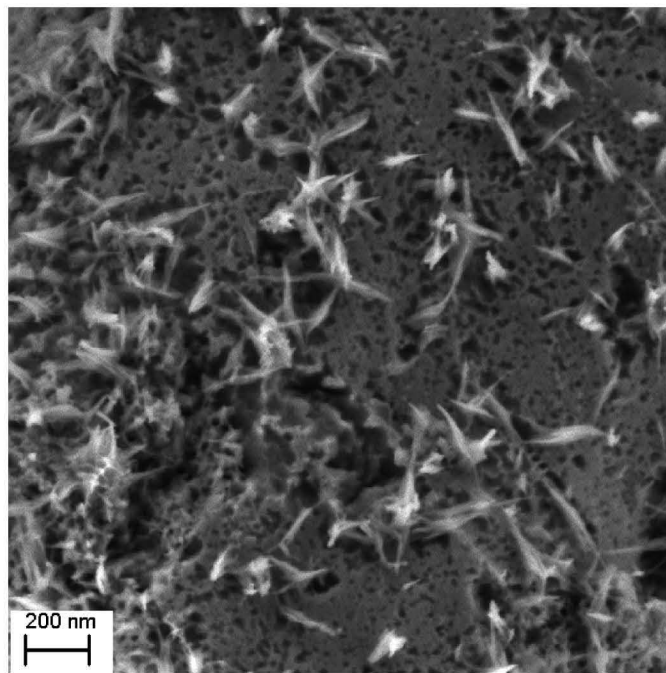
(a)
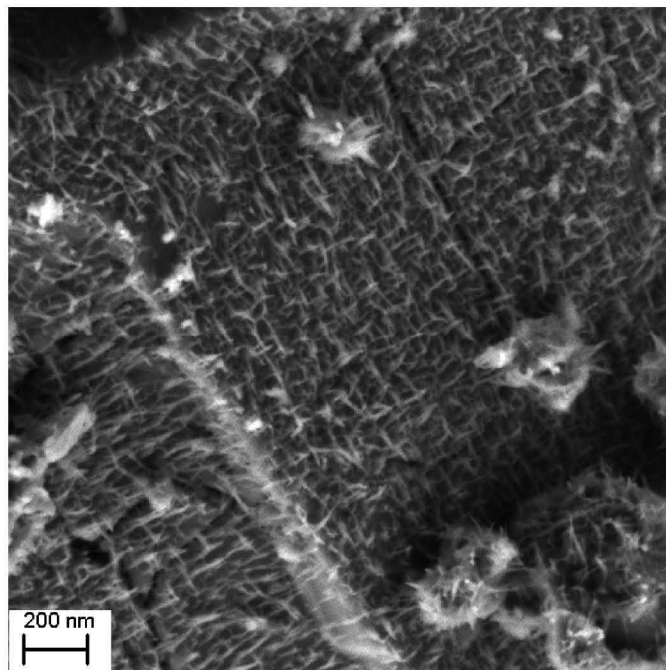
(b)

Figure 4.16: SEM images in secondary electron mode of the surface of (a) C_3S grain and (b) limestone grain, for the mix of 60% C_3S and 40% limestone after 3 hours of hydration.

C-S-H development around C_3S and limestone particles was further investigated by STEM at the maximum heat and after 24h, as indicated by Figure 4.17.
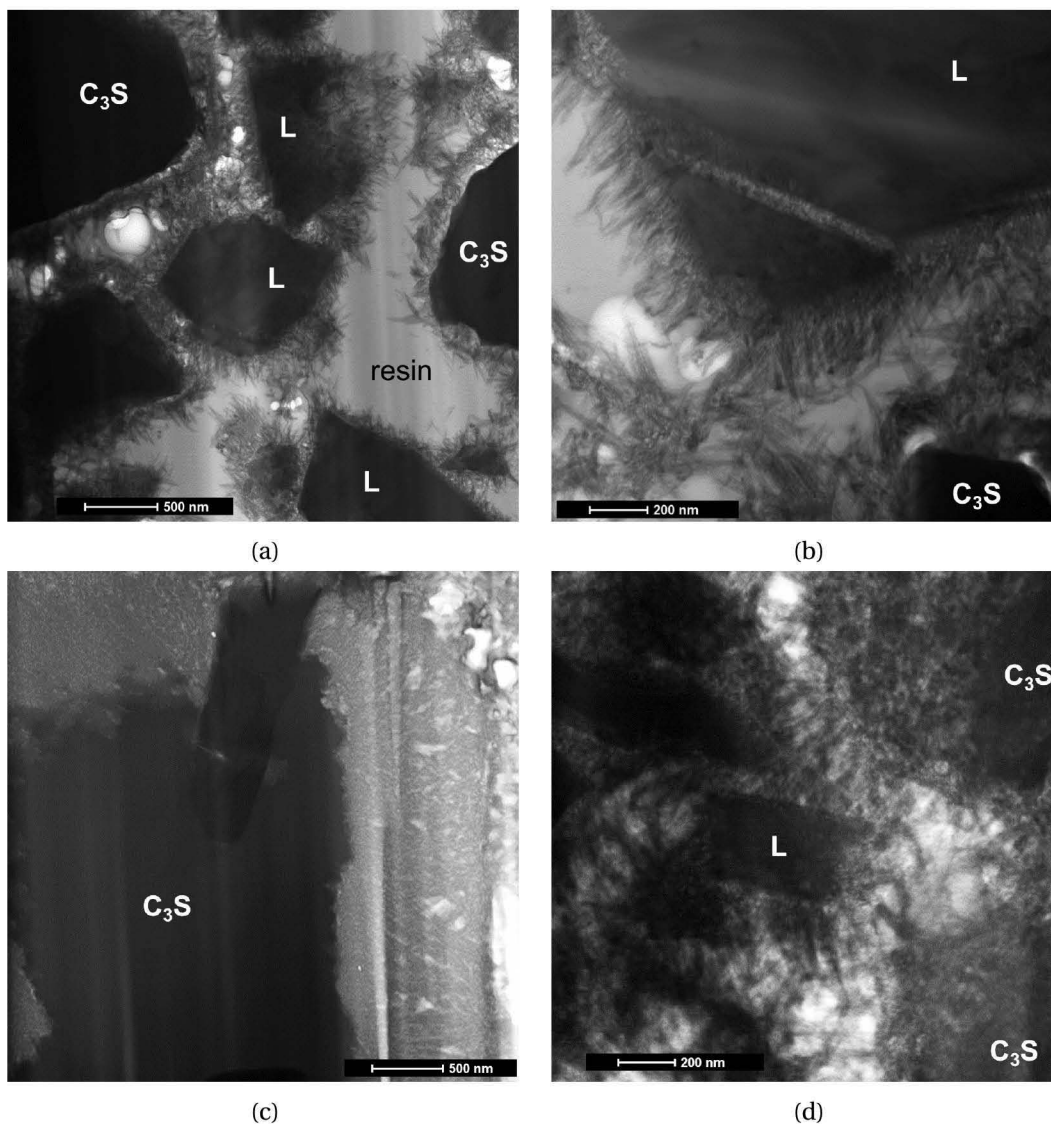
Figure 4.17: STEM images in bright field mode of 60% C_3S - 40% limestone at the peak (a) (b) and after 24 h (c) (d). C_3S indicates C_3S grains and L limestone.

At the maximum heat, C-S-H is observed on both grains of C_3S and limestone. The morphology of C-S-H is different from the other C_3S samples. The needles have a fibril morphology, but they are thinner and are straight perpendicular to the surface of the grains and seem less dense. As images are acquired in bright field mode, for a same thickness, a denser region appears darker. A gap between the C-S-H layer and C_3S grain is observed, while on limestone grains there is no gap.

After 24 h, the formation of inner-product is observed around C_3S grains, but not around limestone grains.

A measurement of the needles length from the maximum heat flow until 7 days is showed in Figure 4.18.
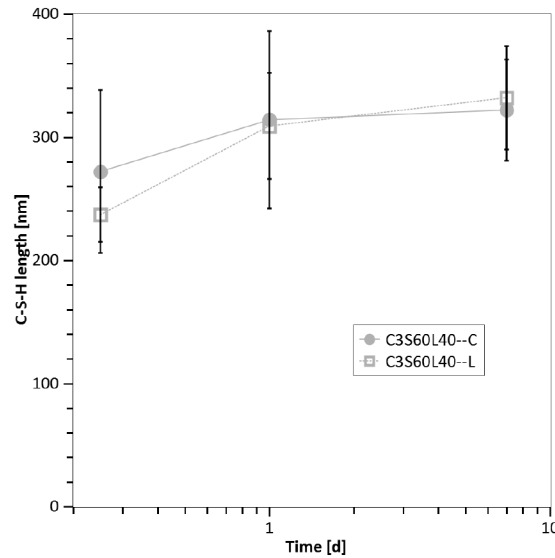
Figure 4.18: Evolution of the needles length with time in the sample with limestone. Needles were measured on C_3S grains and limestone grains. They are indicated by C and L respectively. The error bar represents the dispersion of measurements in several images.

There is no clear distinction between the needles growing on the C_3S grains and on the limestone grains. At the beginning of hydration, they appear to be slightly shorter on the limestone grains, but after 24 h no more difference is observed and the growth of the needles is very slow. The sample with limestone shows a similar evolution of the needles length than the pure paste with a w/c of 0.4 (Figure 4.11 (c)).

Microscopy observations revealed that the presence of limestone increases the nucleation rate of C-S-H, but not its growth rate, as needles have similar length that in pure C_3S pastes. C-S-H preferentially precipitates on limestone surfaces. Also on limestone surface, the C-S-H needles are well oriented, suggesting that calcite provide a better substrate for C-S-H nucleation, most probably due to a crystallographic effect. As limestone dissolves during hydration of C_3S, the increase of calcium in solution combined with the crystallographic effect explain the increase in nucleation rate. This also explains the shorter induction period.

81

4.3.4 Specific surface area

Alite

The specific surface area is known to influence the slope of the acceleration period. An increase in specific surface area gives a higher surface to be covered by hydrates. More hydrates growing, means more dissolution resulting in the increase of heat released for smaller particles. However, the relation between C-S-H growth and specific surface area remains unclear, especially regarding C-S-H rim thickness and needles length at the maximum heat flow. Calorimetry curves of both batches of alite are indicated in Figure 4.19.

(a)

(b)

(c)
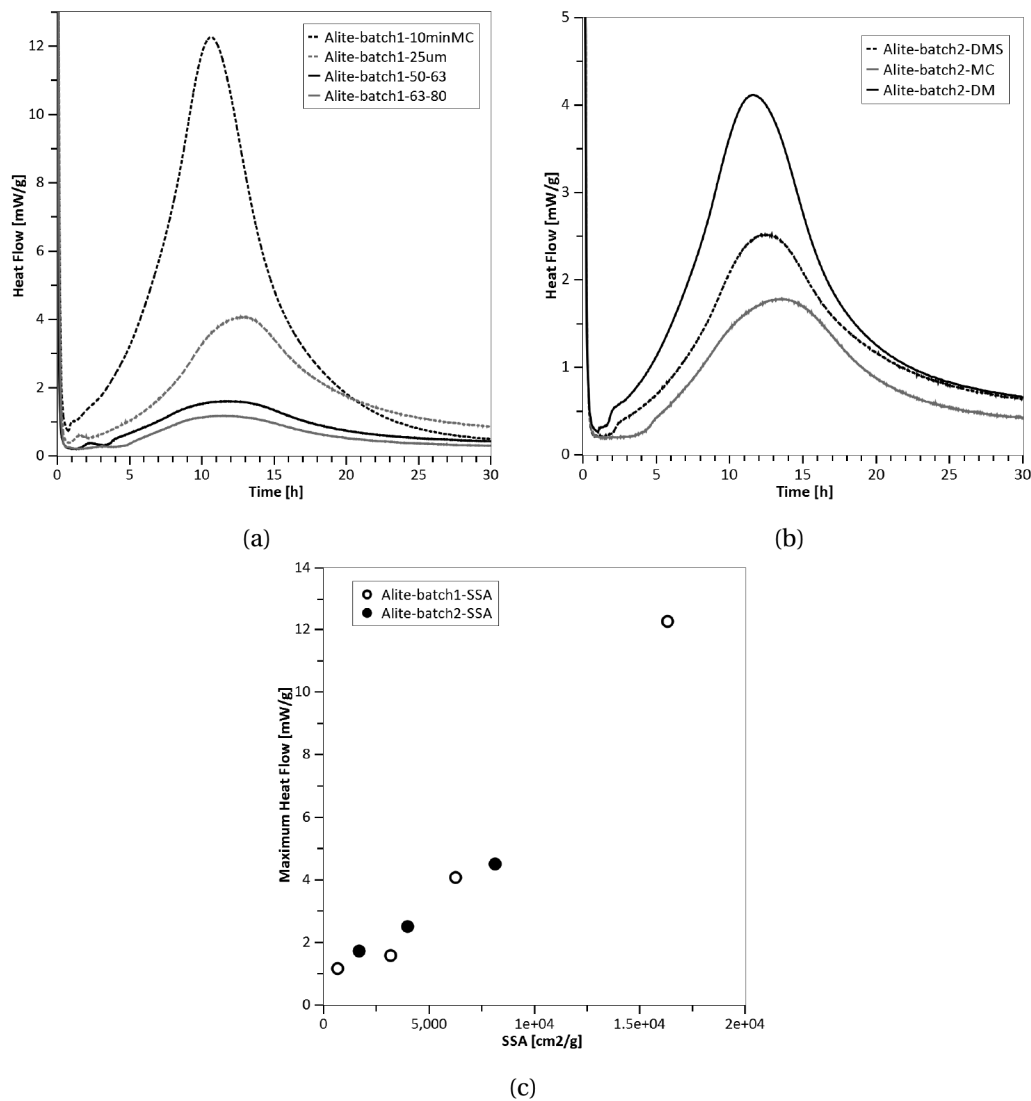
Figure 4.19: Calorimetry curves of (a) alite batch 1, effect different PSD, (b) alite batch 2, different grinding procedures and (c) dependence of the height of the maximum with the specific surface area.

The effect of the increase of specific surface area is an increase of the slope of the acceleration period and the maximum heat flow when the particles are smaller. However, the maximum occurs always at similar time despite the different surface to cover by hydrates. A linear relationship between the specific surface area and the height of the maximum heat flow is observed, as indicated by Figure 4.19 (c).

To study more in detail the coverage of the surface and the thickness and morphology of the C-S-H rim around particles, the hydration was stopped during the acceleration period (6 h) and at the top of the main hydration peak (arrounf 10 h) for the batch 2 of alite.

Figure 4.20 shows the SEM images after 6 hours of hydration. At this stage, the surface is still visible between C-S-H needles. Also some Portlandite crystals are between C-S-H needles. The coverage of the surface is different between samples, this may be due to the different degree of hydration of the alites stopped at 6h.

At the maximum heat flow (Figure 4.21), for all samples the surface is completely covered by hydrates. Since the surface is completely covered by hydrates, it is difficult to distinguish the needles and evaluate their respective lengths. STEM images of samples prepared by disc mill and by Mc-Crone micronizer grinding were acquired (Figure 4.21). C-S-H needles surround anhydrous grains and no Portlandite is observed on these images. C-S-H is observed to grow as needles outwards from the grains of alite. The surface of anhydrous samples is etched for both samples, but a gap is observed between grains and C-S-H, as already mentioned for pure C_3S.

The thickness of C-S-H rim is similar for both samples, despite their different specific surface areas. Smaller particles seem to exhibit larger rim of C-S-H than bigger particle for a same paste (Figure 4.21). This is most probably due to a sectioning effect. There is a lot of space between particles and little impingement of the C-S-H needles is observed. However, the region of interest is very small in STEM compared to the whole sample and more impingement may occur elsewhere.

The STEM images allow a measurement of the length of the C-S-H needles. C-S-H length was compared for alite ground by disc mill with alite ground by Mc-Crone micronizer, since they exhibit different specific surface areas. Needles were considered as the part coming outward from the C-S-H forming around grains, as indicated by Figure 4.22. Measurement of the needles confirmed similar length for both samples, despite their different specific surface areas (Figure 4.22 (c)).

Figure 4.20: SEM images in secondary electron mode showing surface of alite ground with disc mill, disc mill followed by sedimentation and Mc-Crone micronizer during the acceleration period. Calorimetry curve of alite prepared with the different grinding procedures. The results indicate that during acceleration period the surface of the grain is still visible.
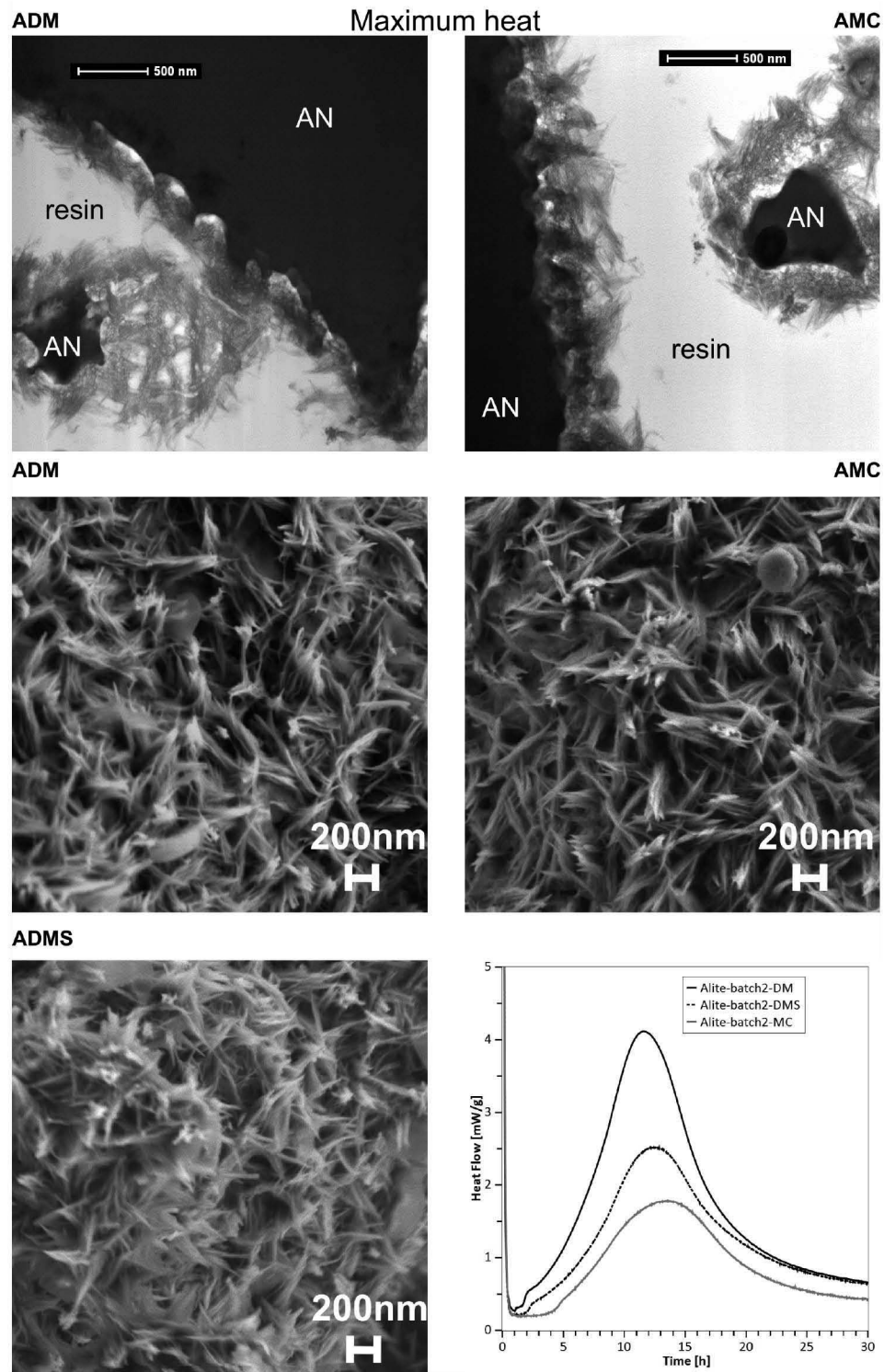
Figure 4.21: SEM images in secondary electron mode showing surface at the maximum heat flow of alite ground with disc mill (10 h), disc mill followed by sedimentation (11 h) and Mc-Crone micronizer (12 h). STEM images of alite at the maximum heat flow for disc mill and Mc-Crone micronizer grinding. In these images, AN indicates anhydrous grain, resin for the embedding resin. Calorimetry curve of alite prepared with the different grinding procedures. The results indicate that the surface is completely covered at the maximum heat flow.

85

(a)   (b)

(c)
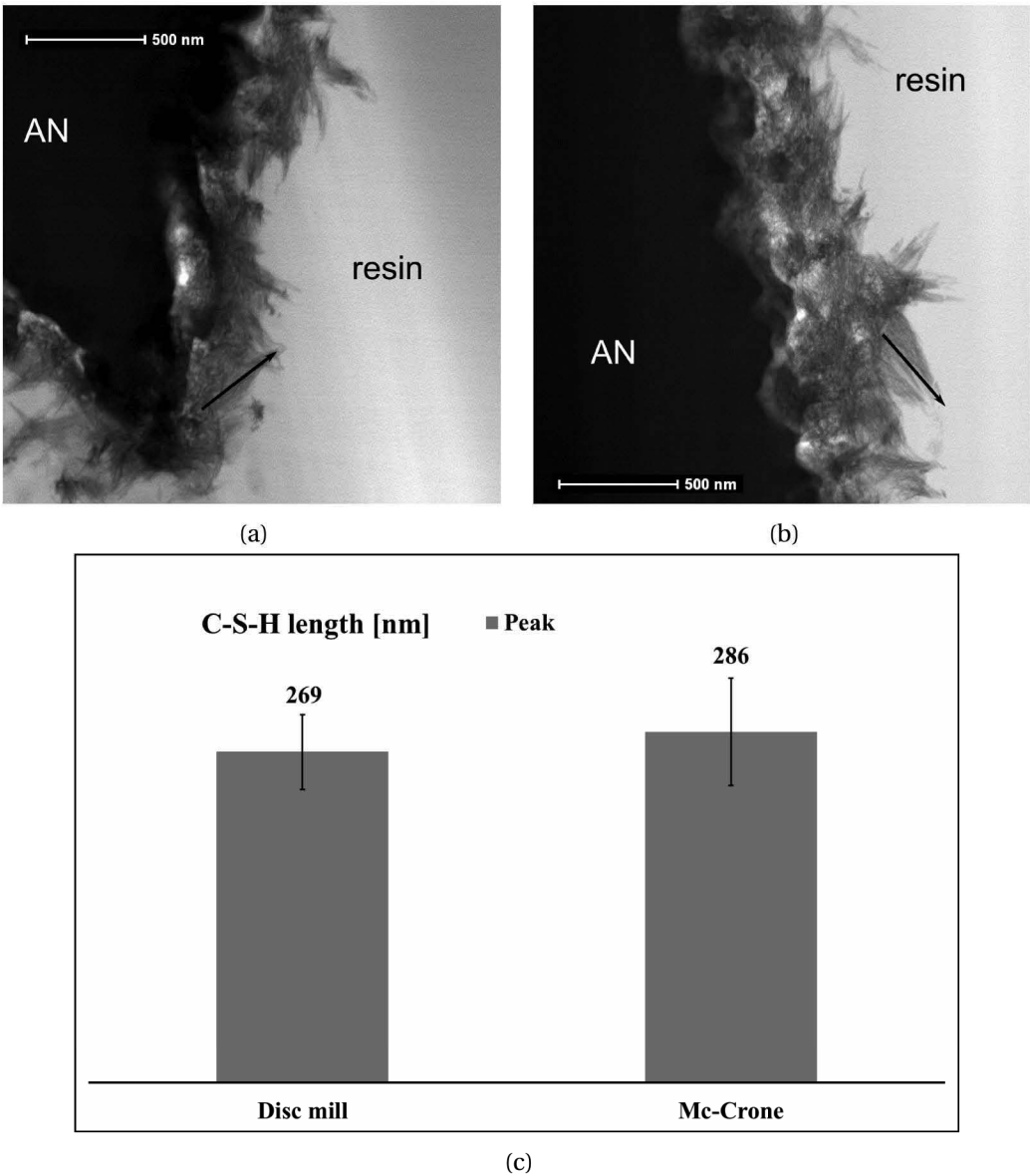
Figure 4.22: Details on C-S-H needles for measurement. (a) disc mill, (b) Mc-Crone micronizer grinding and (c) Measurement of the C-S-H length in nm. The error bar represents the dispersion of measurements in several images.

Clinker

Similar observations about the coverage of the surface during the acceleration period were found for clinker samples. The major difference is that the surface is covered by C-S-H and ettringite, indicated by Aft on SEM images (Figure 4.23). The surface is visible during the acceleration period (Figure 4.24). It should be emphasized that the hydrate distribution on the clinker samples is much more heterogeneous than for alite samples. Some grains were only little covered during acceleration, while other grains were completely covered. However only at the moment of the maximum heat flow all grains were completely covered (Figure 4.25). Also some grains had more ettringite and some grains had more C-S-H.

Regarding the STEM images, the formation of hydrates layer is similar for both samples (Figure 4.25). In clinker ground by Mc-Crone micronizer, the original contour of the anhydrous grain is clearly visible and it seem that a low density product (lighter) is formed between the grain and its original limit. This feature corresponds to the shell formation as observed in cement by Mathur[144].

In clinker samples, especially on STEM cross sections, it is more difficult to distinguish between C-S-H needles and ettringite needles. No measurement of the needle length was done, to avoid over-interpretation of the images and a confusion between the two hydrates.
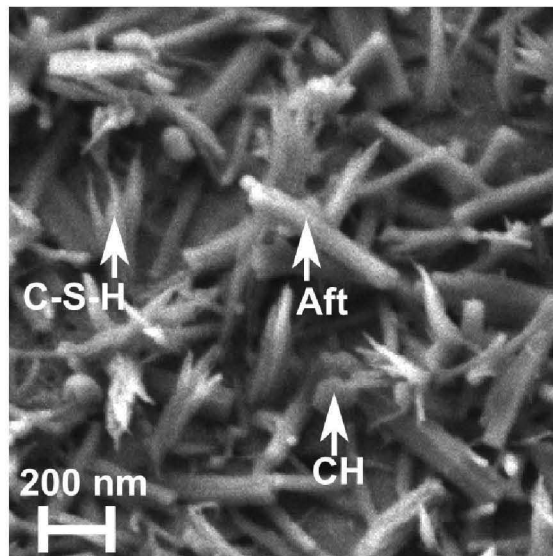
Figure 4.23: SEM images in secondary electron mode of cinker surface, showing C-S-H, Ettringite (AFt) and Portlandite (CH).
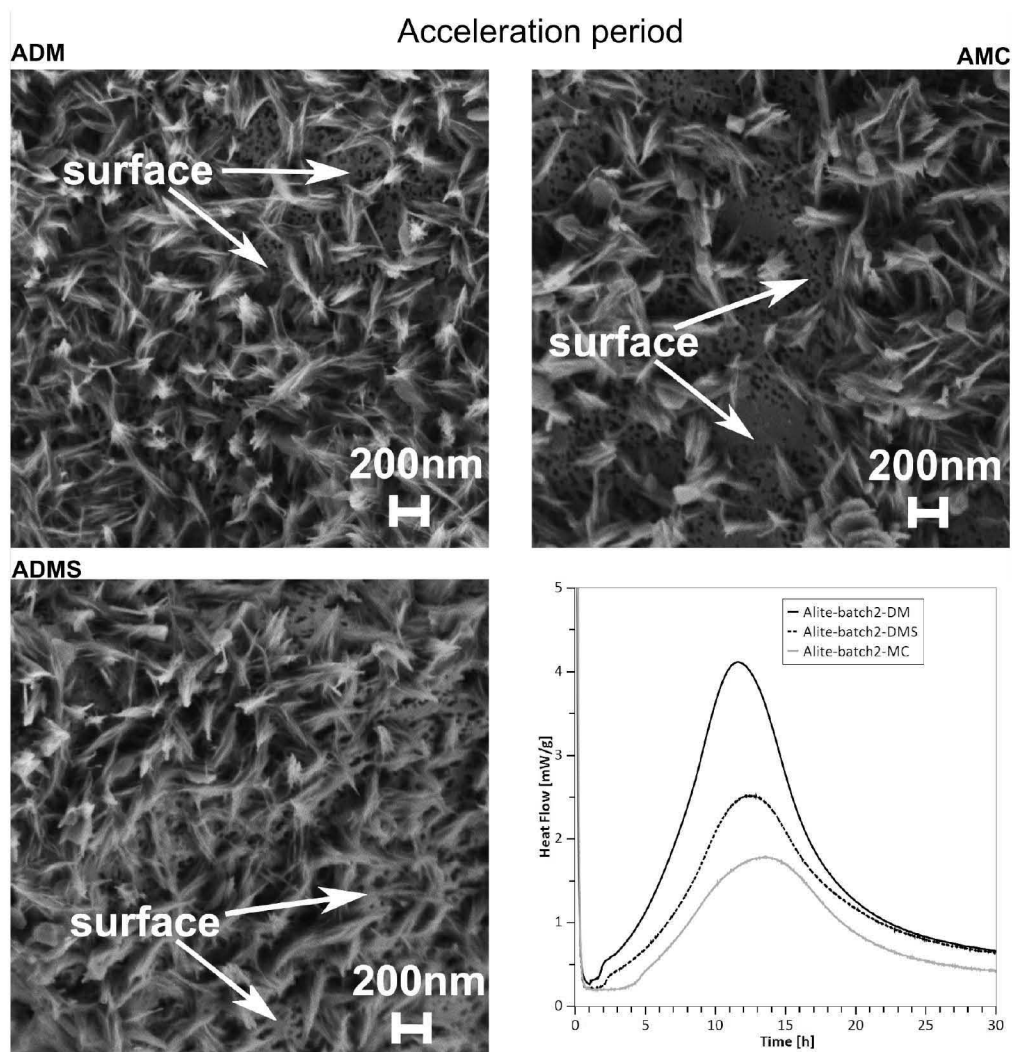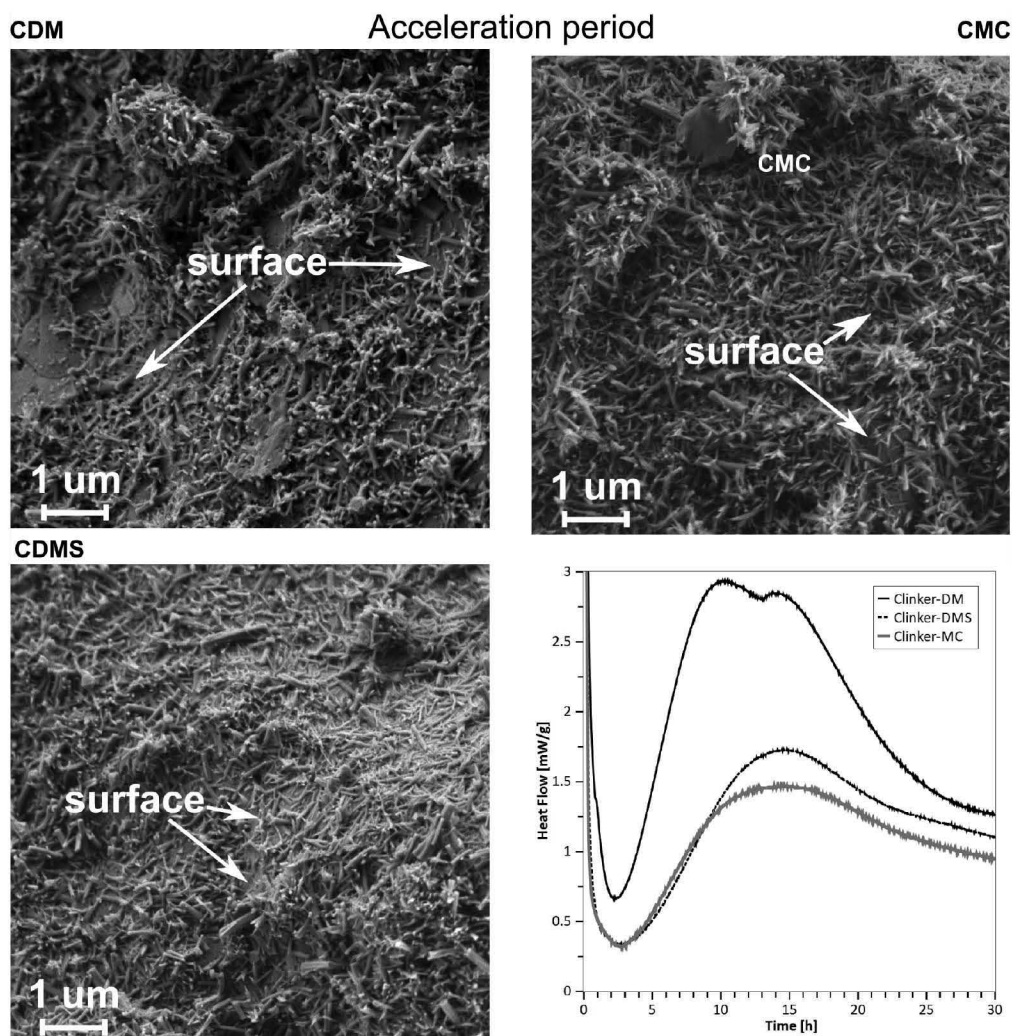
Figure 4.24: SEM images in secondary electron mode showing surface of clinker ground with disc mill, disc mill followed by sedimentation and Mc-Crone micronizer during the acceleration period. Calorimetry curve of clinker prepared with the different grinding procedures. The results indicate that during acceleration period the surface of the grain is still visible.
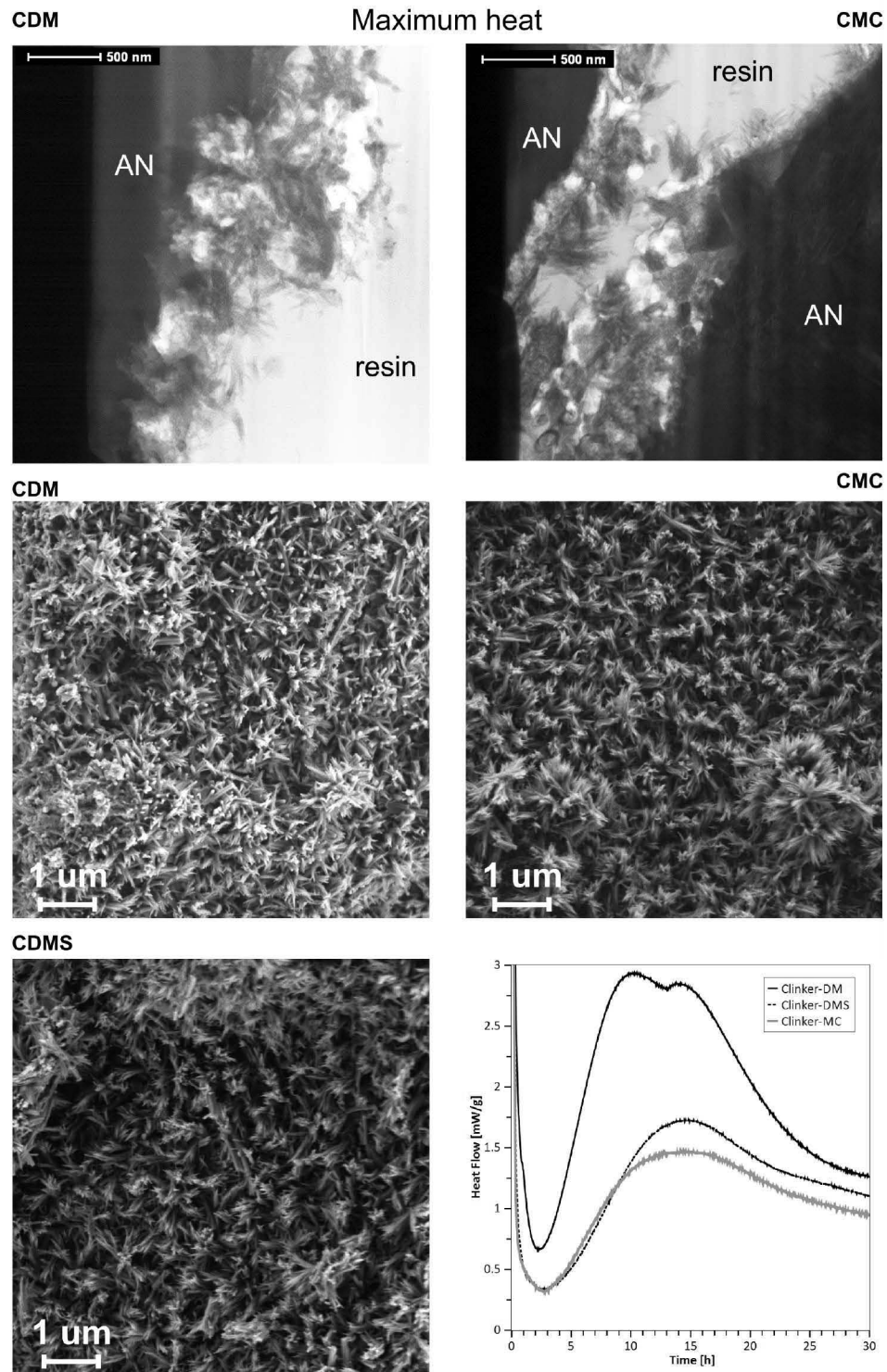
Figure 4.25: SEM images in secondary electron mode showing surface at the maximum heat flow of clinker ground with disc mill (12 h), disc mill followed by sedimentation (14 h) and Mc-Crone micronizer (14 h). STEM images of clinker at the maximum heat flow for disc mill and Mc-Crone micronizer grinding. AN indicates anhydrous grain, resin for the embedding resin. Calorimetry curve of clinker prepared with the different grinding procedures. The results indicate that the surface is completely covered at the maximum heat flow.

89

4.3.5   Doping ions

Hydration kinetics

To avoid artifacts from differences in specific surface areas, two powders were prepared. One with coarser particles sieved between 25 and 36 μm and one with finer particles ground 10 min in the McCrone micronizer. The calorimetry curves of the two samples is given in Figure 4.26.
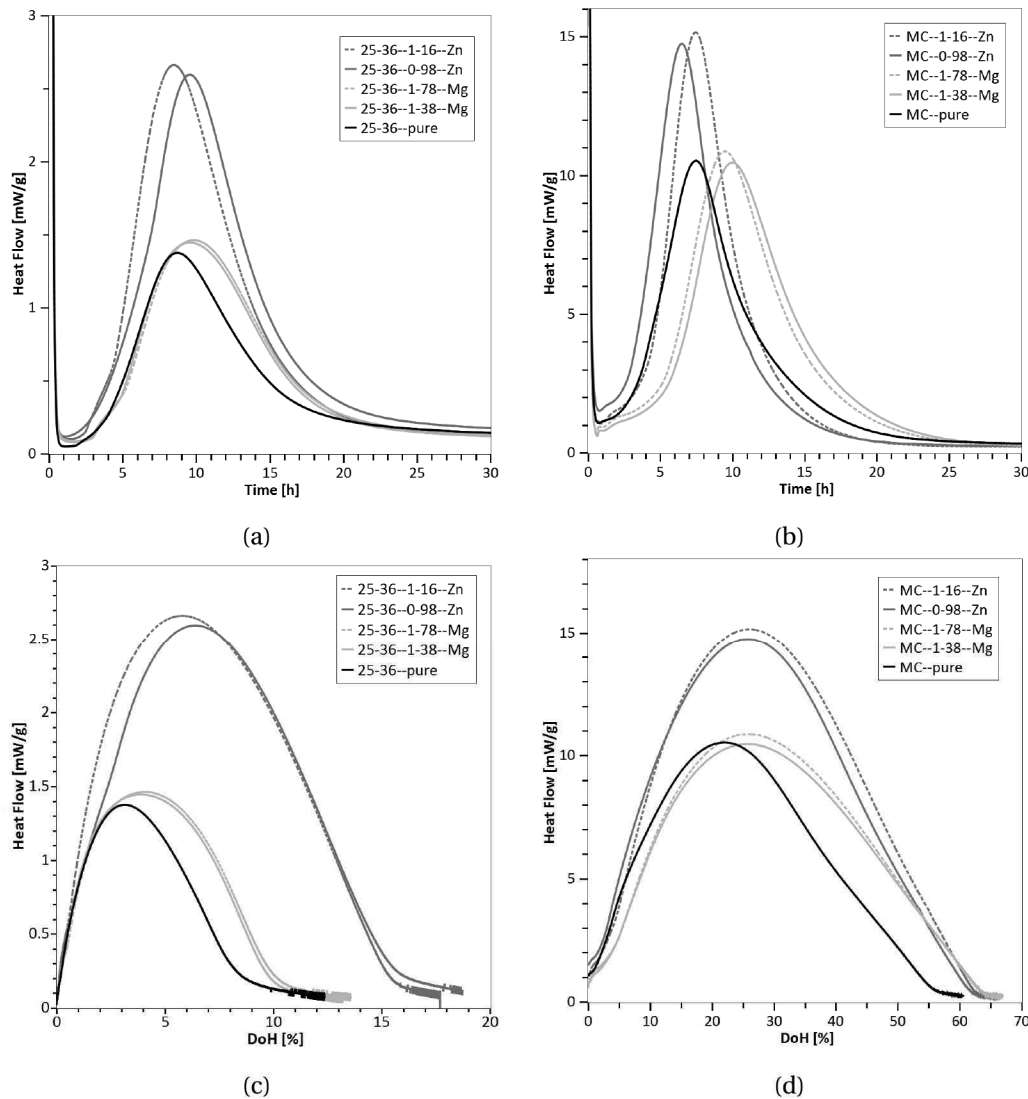
Figure 4.26: Calorimetry curves of alite doped with magnesium and zinc. (a) alite sieved between 25 and 36 μm (b) alite ground 10 min in the McCrone micronizer. Evolution of the heat flow as a function degree of hydration for alite doped with magnesium and zinc. (c) alite sieved between 25 and 36 μm (d) alite ground 10 min in the McCrone micronizer.

The effect of the doping ions on the duration of the induction period was discussed in the previous chapter. For the reground samples, the duration of the induction period is shorter for all samples, due to the very high specific surface area.

After the end of the induction period, magnesium doped alites show a wider peak, but the height of maximum heat flow is similar to pure C_3S (Figure 4.26 (a)). In the case of finer particles (Figure 4.26 (b)), the alite with magnesium enters the acceleration period more gradually resulting in a shift in the time of the maximum heat release rate. However, the peak is still wider. Zinc has an accelerating effect from 2 to 10 hours, with a maximum heat flow at least twice that of pure C_3S, and the peak is also wider (Figure 4.26 (a)). For the coarser particles (25-36 μm) there were slight differences in the specific surface area. However, for the alites with zinc, the specific surface area is only 11% higher, while the increase in maximum heat released is 86% (Figure 4.26 (b)). In the case of finer particles, the presence of zinc increases the maximum heat released by 50%. Even if the alite with zinc has a slightly higher specific surface area as described in chapter 2, this cannot account for the observed increase of the maximum heat flow of the sample sieved between 25 and 36 μm. After 24 hours, the rate of heat evolution is similar for all the samples.

Figure 4.26 (c) and 4.26 (d) shows the evolution of the heat flow with the evolution of the degree of hydration. In the case of coarse particles, the reaction slows down at a degree of hydration around 10% for pure C_3S, 11% in the presence of magnesium and 16% in the presence of zinc. In the case of fine particles, due to the higher specific surface area, the reaction slows down at a degree of hydration around 58% for pure C_3S and alite with magnesium and 63% in the presence of zinc. In the presence magnesium the hydration rate of C_3S is increased during the deceleration period. In the presence of zinc, the hydration rate of C_3S is increased both in the acceleration period and deceleration period (Figure 4.26 (c) and 4.26 (d)).

For the finer particles, mixes between pure C_3S and alites were prepared, with the proportions two thirds of pure C_3S and one third of alite. Two different mixes were prepared: pure C_3S mixed with 1.38 wt% of magnesium and pure C_3S mixed with 0.98 wt% of zinc. The kinetics of the reactions of the mixes were compared with the hydration kinetics of pure C_3S and the corresponding alites paste, as indicated in Figure 4.27. It is interesting to note that for the induction period and the beginning of the acceleration period, mixes follow the kinetics of pure C_3S (Figure 4.27 (b)). During the acceleration period, they diverge from the kinetic of C_3S, to follow the kinetics of their respective alites. At the maximum heat flow it tends to follow the curve of their respective alites. However, for some unknown reason the mix with magnesium shows a maximum heat flow is slightly lower than both pure C_3S paste and pure alite with 1.38 wt% of magnesium paste. The fact that the mixes follow the hydration kinetics of their respective alite only after entering the acceleration period, tends to indicate that ions act only when they are in solution. It is proposed that they may affect the C-S-H growth and eventually be incorporated in C-S-H. Also the ions have little impact on the dissolution rate, since it seems to follow kinetics of pure C_3S.

(a)   (b)
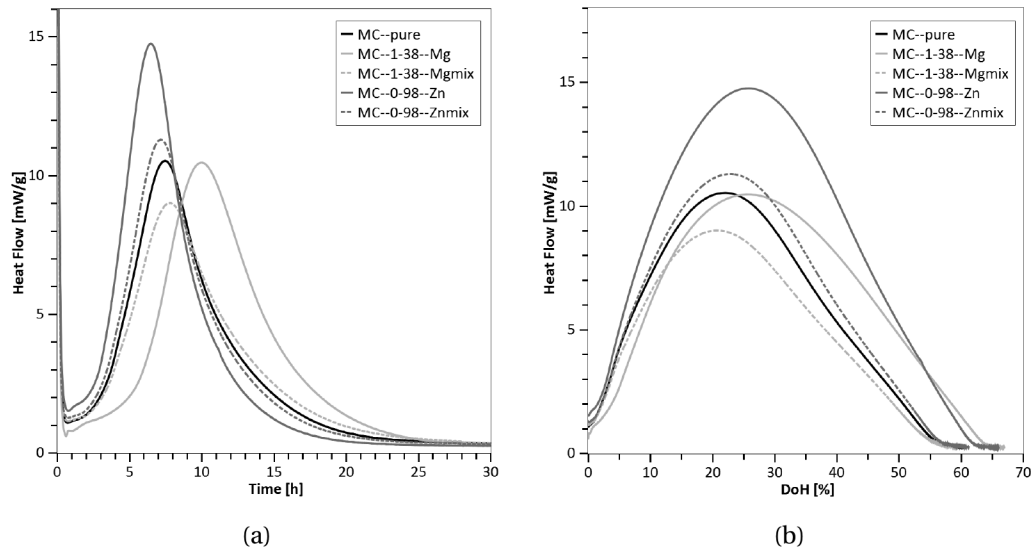
Figure 4.27: (a) Calorimetry curve for the mixes pure C_3S and alites doped with magnesium and zinc. (b) Evolution of the heat flow as a function of the degree of hydration for the mixes pure C_3S and alites doped with magnesium and zinc.

To better understand how zinc and magnesium influence the nucleation and growth of hydrates, SEM images were acquired at 2 hours of hydration on alites, with 1.78 wt% of magnesium and 1.16 wt% zinc, and compared with pure C_3S (sample 25-36µm). The SEM images are shown in chapter 3, Figure 3.19. They showed small clumps of C-S-H, which may originate from a single nuclei. The number of C-S-H clumps was counted on different images; results are given in Figure 4.28. The nucleation density seems not to be influenced by the presence of zinc, but is affected by the presence of magnesium, as shown in Figure 4.28. In the presence of magnesium less nuclei form, but they seem to be bigger after 2 hours (Figure 3.19).
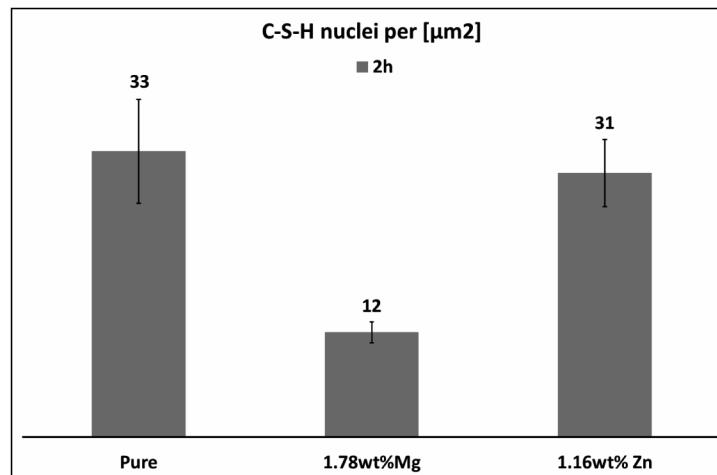
Figure 4.28: Number of C-S-H clumps per μm^2 on the surface of alite with different dopant. The error bar represents the dispersion of measurements in several images.

Morphology of C-S-H

STEM images were acquired on the same samples, at 10h and 24h of hydration to look at the hydrate morphology (Figure 4.29). A clear difference in C-S-H lengths and thickness between pure C_3S and the 2 alites is observed.

After 10 hours of hydration, the surface of the alite grains in all three samples is covered by C-S-H, even alite with magnesium, which had less nuclei at early ages (Figure 4.29 (a), 4.29 (c) and 4.29 (e)). At the peak for all samples a gap between C-S-H and the alite grain is observed. Also the surface remains relatively smooth.

From 10 to 24 h a densification of C-S-H needles is observed, which seems similar for all three samples (Figure 4.29 (b), 4.29 (d) and 4.29 (f)). further the formation of a dense inner-product starts. The gap between C-S-H and alite grain totally disappears and the surface is rough. The samples containing zinc have the thickest layer of C-S-H around grains, which can be explained by their higher degree of hydration at this time.

The lengths of the C-S-H needles were measured on several images following the same procedure used before. In the presence of magnesium, C-S-H needles are thicker about 30 %, but have a similar length to pure C_3S. In the presence of zinc, C-S-H needles are a bit thicker (20 %) and clearly longer confirmed by measurements inFigure 4.30.

In order to see if magnesium and zinc enter into solid solution in hydrates and thus may modify their morphologies, EDX mapping was done on Mg- and Zn- doped alites, with hydration stopped at 24h. Figure 4.30 shows the selected region, containing anhydrous grain, C-S-H and Portlandite and the resulting elemental mapping for magnesium and for zinc.

From Figure 4.30, it is clear that ions are present in the anhydrous grains and are not incorporated in Portlandite, as expected. Quantification of EDX mapping indicated 0.3 at% of magnesium and about 0.7 at% of zinc in C-S-H. Since the reliability of measurements below 1% is poor and the fact that there may be a considerable background signal, the presence of Mg in C-S-H is questionable. Rather, magnesium is present in clusters, which are not evident in the STEM images. These clusters, rich in magnesium, were already observed at 10h by EDX mapping and suggest the formation of another hydrate phase containing magnesium (e.g. brucite, or M-S-H?). This is consistent with other studies on cement, which show very little incorporation of magnesium in C-S-H[119;145]. The reason why magnesium is not incorporated in C-S-H comes from the fact that magnesium hydroxide precipitates at pH about 9 and remain then insoluble[146]. In the alite pore solution the pH is about 12.6.

Zinc is incorporated homogeneously in C-S-H and no clusters were observed. The occurrence of longer needles suggests that zinc increases the growth rate of C-S-H. In terms of atomic radii, the effective radius in pm for Zn^{2+} is 0.74, while for Ca^{2+} it is 1 and for Si^{4+} it is 0.4. From their respective sizes it is most likely that zinc is replacing calcium sites. Kulik et. al[147] showed that the most stable hydrated phase in the presence of zinc is a CZSH ((Ca+Zn)/Si = 1).
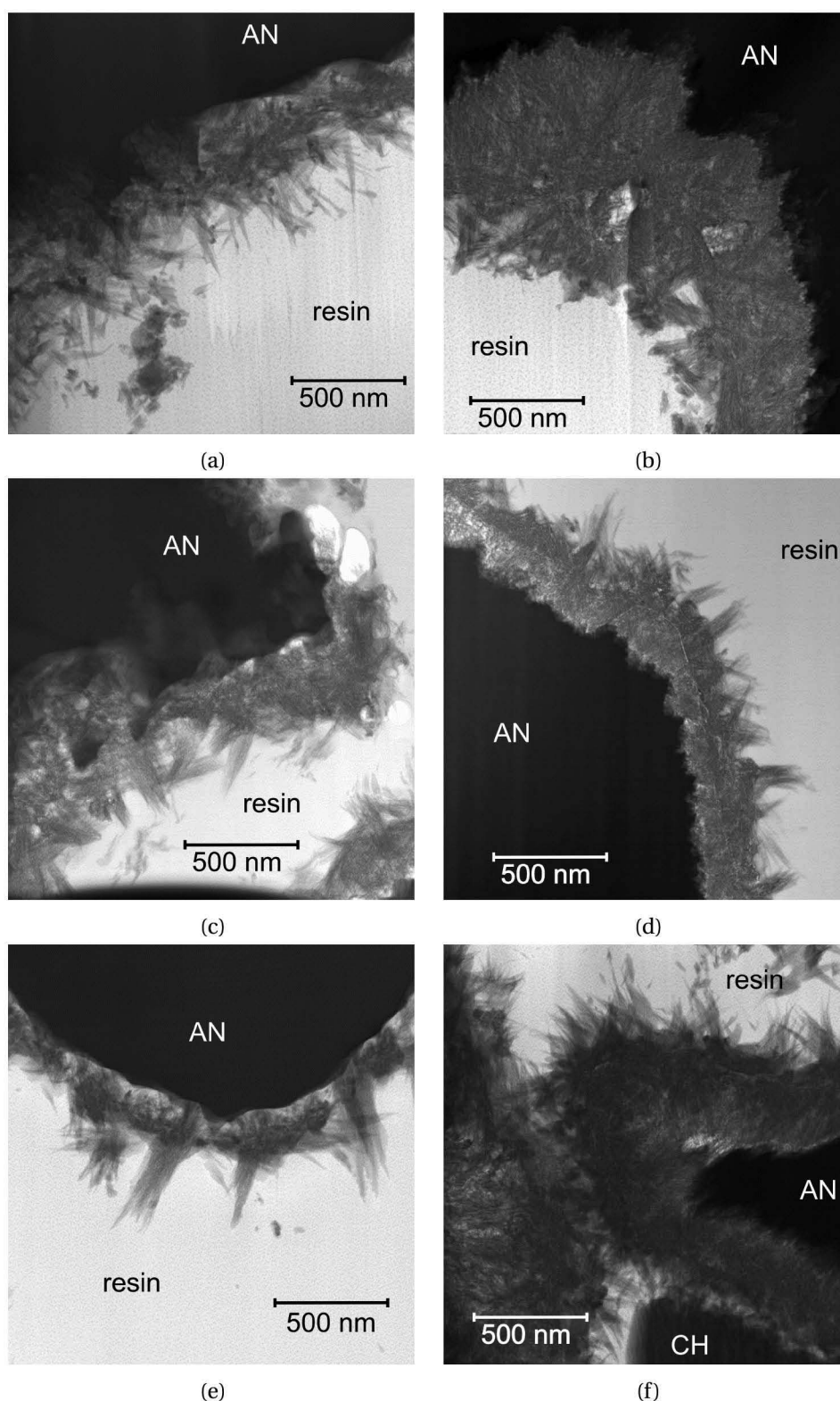
Figure 4.29: STEM images in bright field mode of pure C_3S, (a) after 10 h, (b) after 24 h, alite with 1.78 wt% of magnesium (c) after 10 h (d) after 24 h and alite with 1.16 wt% zinc (e) after 10 h, (f) after 24 h. In the images, anhydrous grains are indicated by AN, resin by resin and Portlandite is indicated by CH.
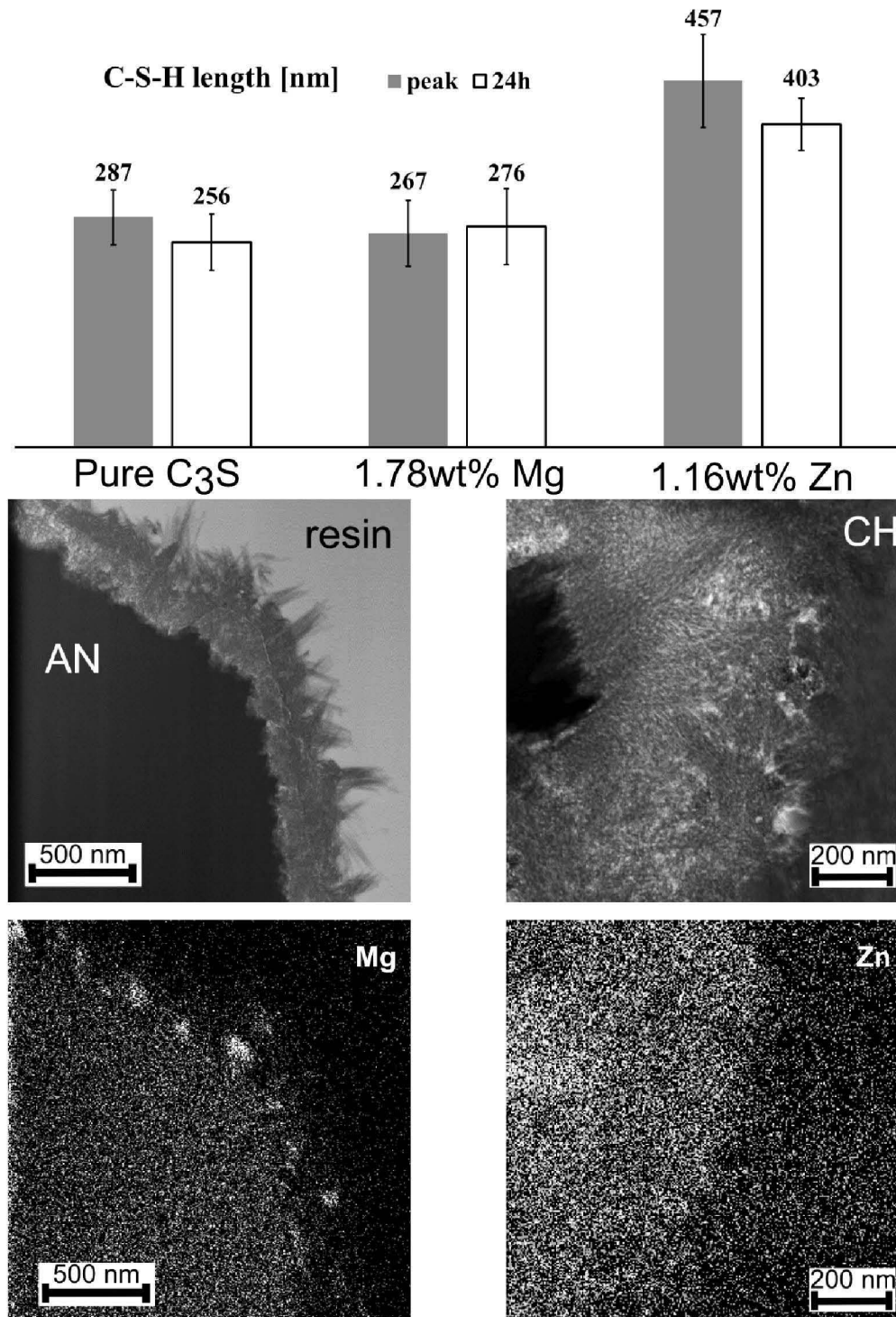
Figure 4.30: Measurement of the C-S-H length in nm. STEM images and EDX mapping after 24 h of hydration for alite with 1.78wt% of magnesium and alite with 1.16wt% zinc. In the images, anhydrous grains are indicated by AN, resin by resin Portlandite by CH, magnesium by Mg and zinc by Zn. Results show that zinc is well incorporated in C-S-H and needles are longer, while magnesium is not incorporated in C-S-H and there is no effect on the C-S-H needles length.

4.4 Numerical modeling

4.4.1 μic equations

In the previous section, it was observed that nucleation and growth of C-S-H govern the acceleration period and is modified by the presence of ions. Simulations of calorimetry curves of alites with ions and alite ground with different grinding procedures were done, using parameters deduced from image analysis. The modelling platform μic[107;139] is used for this study. This platform was already used to simulate early hydration kinetics of alite[148], where the nucleation and densifying growth mechanisms operate during acceleration period. The version of the model used in this work is similar to that of Kumar et al.[148]. However, two essential differences distinguish the current model from the previously published ones[107;139]. The first, which is not essential, is that the impingement between the hydration products of neighbouring grains is neglected as is the disappearance of the smallest particles early in the hydration process. The second, crucial difference is that the nucleation and growth process is assumed to occur in two dimensions at the surface of particles. As the growth observed is needle like, the volume of hydrates is simply obtained by extruding the 2D quantity. Figure 4.31 show a schematic representation of the growth of C-S-H needles on the surface of alite grains.
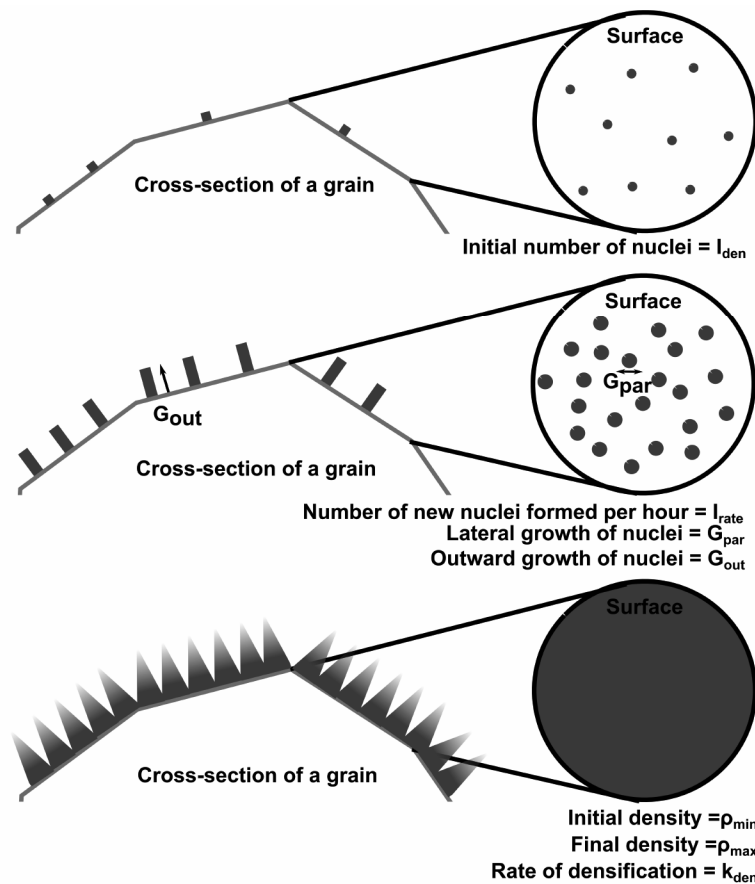
Figure 4.31: Schematic representation of C-S-H growth as used in μic.

Observations show however that the needles are not cylindrical, but rather cones, which further seem to densify during the hydration. We therefore explain the minimal density and densifying kinetics parameters (ρ_{min}, k_{den}) as reproducing these aspects.

To speed up calculations, the equations were modify in such a way that the interaction on the scale of individual particles was not calculated[148]. The concept of extended volume V_{ext}, which represents the expected volume of a set of growing nuclei, was introduced. This volume of densifying C-S-H is calculated along time with equation 4.2:

$$V_{extended} = \int_{0}^{G_{out}} a_{BV} \cdot \left(1 - \exp(-A_f)\right) dy \tag{4.2}$$

Where A_f is written as

$$A_f = \pi \cdot \left[I_{density} \cdot G_{par}^2 \left(t_r^2 - \frac{y^2}{G_{out}^2} \right) + I_{rate} \cdot G_{par}^2 \left(\frac{2y^3}{3G_{out}^3} + \frac{t_r^3}{3} - \frac{2y^3 t_r}{G_{out}^2} \right) \right] \tag{4.3}$$

In the model, the needles growth was calculated by the 2D extrusion. C-S-H is representated as cylindres growing from the surfaces. As microscopy images show rather an agglomaretaion of sheets, a conical shape describes better C-S-H needles. The evolution of the density with time is used as a fitting function to reproduce the cone shape of the needles instead of cylinder. The dependance of the density of C-S-H with time is expressed as:

$$\rho_{t_r} = \rho_{max} - (\rho_{max} - \rho_{min}) \cdot \exp\left(\frac{-k_{den} \cdot t_r}{\rho_{max} - \rho_{min}} \right) \tag{4.4}$$

In equations 4.2 to 4.4 the different parameters are described below:

- a_{BV} which is the total surface of the powder per unit volume, $[\mu m^{-1}]$

- G_{out} which is the outwards growth of C-S-H $[\mu m\, h^{-1}]$

- $I_{density}$ which is the nucleation density on a surface, $[\mu m^{-2}]$

- G_{par} which is the growth parallel to the surface $[\mu m\, h^{-1}]$

- t_r which is the time at which the nucleation and growth process starts, $[h]$

- I_{rate} which is the nucleation rate per unit area $[\mu m^{-2}\, h^{-1}]$

- ρ_{max} which is the maximum density of outer C-S-H $[g\, cm^{-3}]$

- ρ_{min} which is the initial density of outer C-S-H $[g\, cm^{-3}]$

- k_{den} which is the rate of densification of outer C-S-H due to impingement $[g\, cm^{-3}\, h^{-1}]$

The extended volume is converted to the real volume by equation 4.5:

$$\frac{dV_{real}}{dt} = \frac{dV_{extended}}{dt}(1 - V_{real}) \tag{4.5}$$

This equation is only valid for a system with a single product and does not take into account the volume occupied by the other hydrates. To deal with this issue, it was assumed that extended volume was lost due to overlap increase as the real volume available for growth reduces[148], expressed by equation 4.6:

$$V_{real} = 1 - \exp(-V_{extended}) \tag{4.6}$$

Then the mass of alite reacting in a period of time is calculated with equation 4.7:

$$
-dm_{alite} =
$$
$$
\frac{1}{\kappa} \cdot \left[\frac{\rho(t_r)}{\rho_0} \left(dV_{ext,CSH}(t + dt) - dV_{ext,CSH}(t) \right) (1 - V_{real}) + \frac{\rho(t_r + dt_r) - \rho(t_r)}{\rho_0} \cdot V_{real,CSH} \right] \tag{4.7}
$$

Here we use the information from the microstructural observations to make the choice of the parameters:

- the total surface of the powder per unit volume, a_{BV}, was calculated from the specific surface area of the powder deduced from the PSD measurement in $cm^2\,g^{-1}$ and the density of alite $3.15\,g\,cm^{-3}$.

- the nucleation density on a surface, $I_{density}$ in μm^{-2}, was estimated from SEM images.

- the nucleation rate per unit area, I_{rate} in $\mu m^{-2}\,h^{-1}$, was set to 8, assuming a constant heterogeneous nucleation during acceleration. The value was estimated from evolution of the surface of alites particles during the acceleration period.

- the maximum density of outer C-S-H, ρ_{max} was set as $2.1\,g\,cm^{-3}$, commonly accepted value found in the literature[148].

- the rate of densification of outer C-S-H due to impingement, k_{den} in $g\,cm^{-3}\,h^{-1}$, was set at 0.0001, since particles have a narrow size distribution and the space is not entirely filled. If the small particles were considered, the impingement would cause a faster deceleration. However the simplified version of the model used here, does not fully take this effect into account.

- the outwards growth of C-S-H, G_{out} in $\mu m\,h^{-1}$, was calculated from calorimetry curves and STEM images. The calorimetry curves give the duration of the acceleration period as calculated from the end of the induction period to the maximum heat. The STEM images give the length of the needles. With this information the growth rate was calculated for each alite, assuming a constant rate during the acceleration period.

- the growth of C-S-H parallel to the surface, G_{par} in $\mu m\,h^{-1}$, was estimated to be 20-30% G_{out}. This is according to STEM images, which showed that the thickness of the needles were 20% and 30% their length.

- the initial density of outer C-S-H, ρ_{min} in $g\,cm^{-3}$, was the only free parameter and was kept in the same range. From images the initial density of C-S-H was estimated to be around 10% of the maximum density, which is $2.1\,g\,cm^{-3}$.

- the time at which the nucleation and growth process starts, t_r in h, was manually adjusted according to the start of the acceleration period for each sample. It does not vary much between samples and is independent of the nucleation and growth process discussed below. It should not be considered as a parameter as such.

As ρ_{min} and a_{BV} have a strong impact on the height of the maximum heat flow in the simulated curves, to compare the effect of the other parameters on the calorimetry curve, ρ_{min} was set constant for a system and the specific surface area was calculated from the particle size distribution assuming spherical particles. All the other parameters were measured on microsocpy images.

4.4.2 Simulations

Effect of the doping ions

First the calorimetry curves of alite with different dopant were simulated, since they all have the same specific surface area and w/c. for the different inputs parameters, the $I_{density}$ was vary between the different composition as shown by Figure 4.28. Then according to microscopy observation, G_{out} and G_{par}, were calculated from Figure 4.29, which shows thicker needles at the maximum heat flow. The values of the different parameters used are given in table 4.1.

Table 4.1: Input parameters for alite with different dopant.

	Pure	1.78wt% Mg	1.16wt% Zn
G_{out} [$\mu m\,h^{-1}$]	0.041	0.041	**0.075**
G_{par} [$\mu m\,h^{-1}$]	0.011	**0.015**	0.012
ρ_{min} [$g\,cm^{-3}$]	*0.21*	*0.21*	*0.25*
$I_{density}$ [μm^{-2}]	**33**	**12**	**31**
t_r [h]	*1.8*	*2.6*	*2*

Figure 4.32 presents the calorimetry curves of the 3 alites with their corresponding curve simulated with the modeling platform μic. Simulations were adjusted to the calorimetry curves only by changing the time at which the nucleation and growth regime starts. Extremely good agreement is obtained between the simulated and experimental calorimetry curves during the acceleration period and just over the peak maximum.

(a)

(b)

(c)
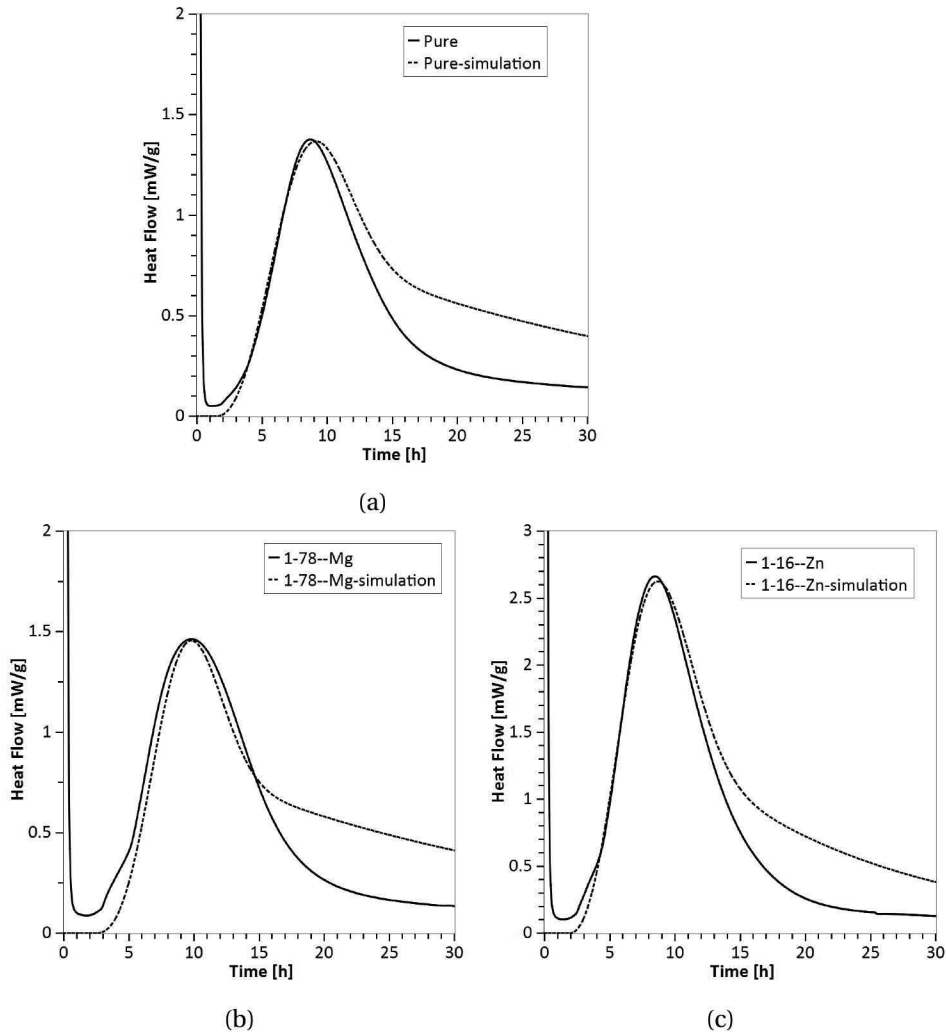
Figure 4.32: Comparison between the experimental and the simulated calorimetry curve of (a) pure C_3S, (b) alite with 1.78wt% magnesium and (c) alite with 1.16wt% zinc.

Effect of the specific surface area

From these results, the samples with different specific surface areas were also simulated. In this case, the only parameter which vary is the specific surface area. There is no microstructural observations indicating a modification of the growth rate of C-S-H when particles size changes. Thus, G_{out} and G_{par} were calculated from Figure 4.21. The same value as alite with 1.78 wt% magnesium for the $I_{density}$ was taken, since these samples contained magnesium. The values of the different parameters are given in table 4.2 and the corresponding simulations of the calorimetry curves are given in Figure 4.33.

Table 4.2: Input parameters for alite with different grinding procedures.

	ADM	ADMS	AMC
SSA [$cm^2\,g^{-1}$]	**8142**	**3993**	**1691**
G_{out} [$\mu m\,h^{-1}$]	0.026	0.026	0.026
G_{par} [$\mu m\,h^{-1}$]	0.01	0.01	0.01
ρ_{min} [$g\,cm^{-3}$]	*0.42*	*0.42*	*0.42*
t_r [h]	*2.6*	*2.6*	*2.6*

(a)

(b)

(c)

(d)
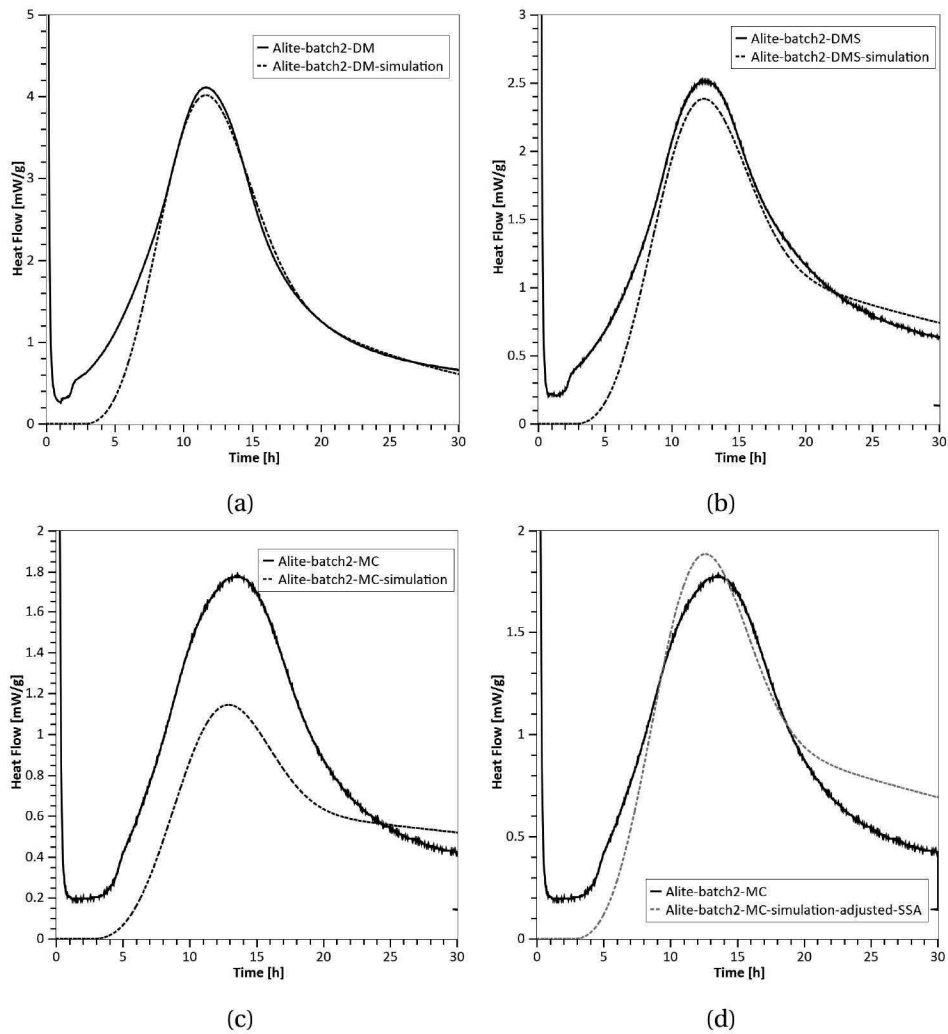
Figure 4.33: Comparison between the experimental and the simulated calorimetry curve of alite ground by (a) disc mill, (b) disc mill followed by sedimentation and (c) Mc-Crone micronizing. (d) Mc-Crone micronizing with is specific surface area adjusted to 3000.

In this case, correspondence between the simulated and experimental calorimetry curves during the acceleration period and just over the peak maximum are slightly less good. In the case of alite ground by Mc-Crone micronizer, the simulated curve cannot approach the experimental one. The main issues comes from the fact the only varied parameter was the specific surface area. The specific surface area was estimated from the measurement of particles size distribution assuming particles as spheres. As shown by Figure 4.34, the particles are not sphere and surfaces are not regular, especially the particles ground by Mc-Crone, which shows angular shapes. With the method used, the specific surface area is underestimated. If particles would be considered as cub, the specifics surface area should be twice higher. Simulation for the alite ground by Mc-Crone micronizer was repeated using a specific surface area of 3000 $cm^2\,g^{-1}$, as indicated in Figure 4.33 (d). As the the specific surface areas and the minimal density are the two parameters influencing the height of the maximum heat in the simulated curves, an underestimation of the specific surface area results in an increase of the minimal density value.

(a)   (b)   (c)
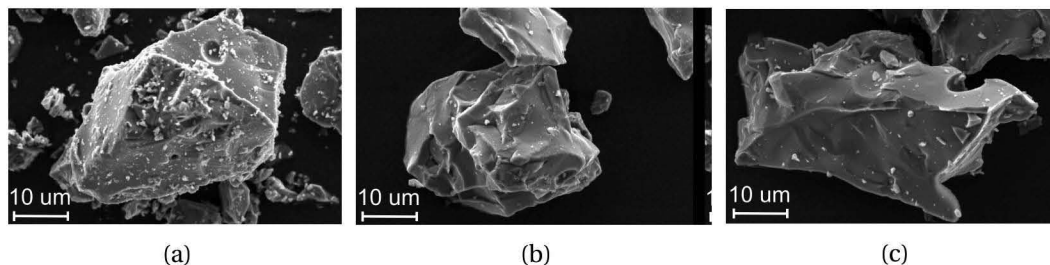
Figure 4.34: SEM images in secondary electron mode of alite after, (a) disc mill, (b) disc mill and sedimentation and (c) Mc-Crone micronizer grinding.

4.5 Discussion

4.5.1 Growth of C-S-H

From SEM observations, it is clear that C-S-H grows with a needle morphology, which can be an agglomeration of sheets. Also these needles have a well defined shape, suggesting a certain order in the C-S-H atomic structure.

These needles grow until a similar length for all systems, as summarized by Figure 4.36. Longer needles were observed in the case of higher w/c, but at the same time lower nucleation rate was observed. This increase of growth may simply result from the higher space available to develop. For a same w/c, only the presence of zinc significantly increased the growth rate of the needles. In this case, the increase is attributed to the incorporation of zinc in the C-S-H atomic structure.

The reason for needle shape can come from different factors. If C-S-H is considered as an imperfect crystal, a needle shape results from the growth of a face with a high surface energy.

In this case, the needles shape is adopted by the system to reduce its energy, as it is observed for other system[149]. Another reason that can force the system to form needles is the diffusion. In metallurgy, the formation of dendrites results from the slow diffusion of species to aliment the growth, thus only the tip can grow. The secondary branching results from different supply of solute. This mechanism is unlikely to be applicable in the case of hydration, since the diffusion of ions in water is very high, especially during the acceleration period, when the system still contains a lot of liquid water.
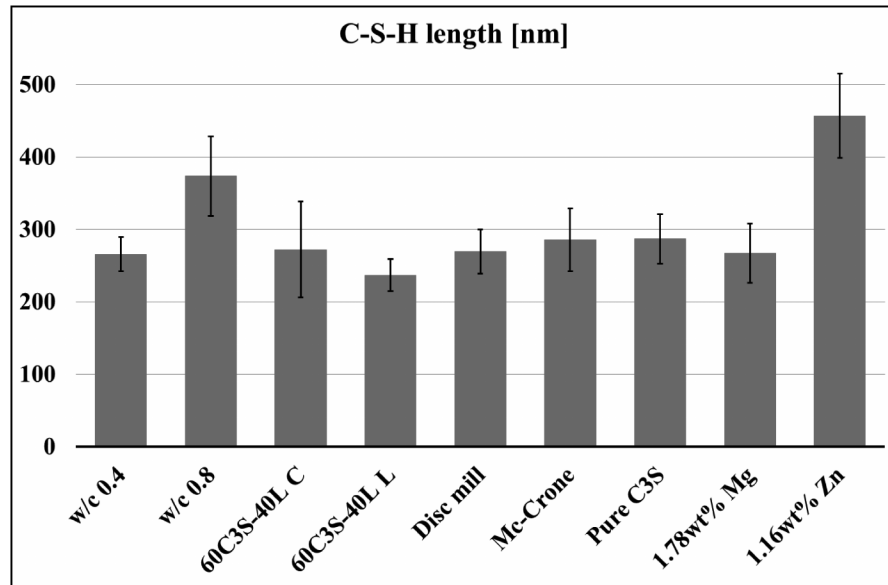
Figure 4.35: Measurement of the C-S-H length in nm at the maximum heat flow for all the systems studied.

In the case of clinker, it is observed that the surface of the grain is also covered by ettringite (Figure4.23). On some grains the surface is completely covered before the main hydration peak (Figure 4.24 and 4.25), but not all grains are completely covered.

4.5.2 Proposed mechanism for the transition from acceleration to deceleration period

STEM images revealed that the impingement is very different between samples, but the deceleration occurs at similar time for all of them. The microstructure is not completely full of hydrates in some cases, even after 24 h of hydration, while in other systems impingement starts during the acceleration period. These experimental results are not in agreement with the hypothesis of Bishnoi[107], that a low density C-S-H product grows rapidly to fill the entire space and then starts to densify, when it impinges with product coming from neighborhood particles, initiating the deceleration period. An increase of the packing density of C-S-H is observed during hydration (Figure 4.12), but C-S-H is not completely filling the space between particles.

The observations show that in any case the surface is completely covered by hydrates at the maximum heat flow, which suggests that the lateral impingement of hydrates is limiting the reaction rather that the impingement due to neighborhood particles. From microscopy observations (Figure 4.9, 4.20, 4.24 and 4.29), it seems unlikely that C-S-H nucleates on the tip of another needle. If the surface is completely covered by hydrates and C-S-H cannot grow on an existing needle, to continue the reaction different growth process needs to be initiated. One can consider that the coverage of the surface is limiting the reaction, which explains why the different specific surface area does not influence the growth rate of the needles, but affects the height of the peak. More surface to cover implies more dissolution and thus a higher hydration peak.

It is proposed that at the maximum heat, a transition from the outer-product to the inner-product growth occurs. Since C-S-H cannot anymore precipitate on the surface of the grain and grow as needles, C-S-H precipitates on the interface between the grain and the originally formed outer-product. Since little space is available there is a limited growth, resulting in an accumulation of nuclei, which would give this isotropic texture observed in the inner-product[104–106]. When this second growth mechanism is activated, no more gap is observed (Figure 4.12 and 4.29). From this point, it is expected that there is less transport through the whole solution and transport mainly proceed in the capillary pores. C-S-H needles are still growing, but with a slower rate.

The following scheme represents the different steps of the growth of C-S-H during the hydration.

Figure 4.36: Representation of the hydration mechanism during hydration kinetics. Fist C-S-H grow as needles outside grains. Once the surface is completely covered by needles, a second growth mode is initiated.

C-S-H nucleates on the surface of particles during the induction period. At the end of it, when the supersaturation degree with respect to Portlandite is reached, C-S-H nuclei start to grow rapidly outward from the surface, but also along the surface. Also, new nucleation and growth sites are created during the acceleration period. C-S-H needles grow during the ac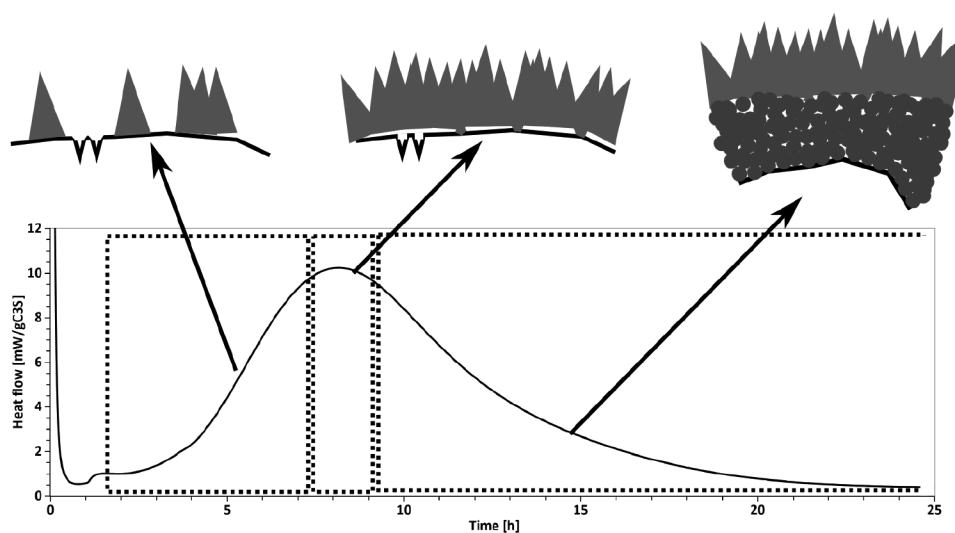celeration period, until no more free surface is available. At this time, the maximum heat flow in calorimetry curve is reached and the surface is completely covered by hydrates. Since no more surface is available for C-S-H to precipitate, a different growth is activated, the formation of the inner-product starts at the maximum heat flow. The transition from acceleration period to deceleration period is caused by a different growth mechanism in C-S-H due to the limitation of the available surface to grow C-S-H needles. However, needles are still growing, but more slowly and well as the Portlantdite.

The mechanism presented above may describe well the reaction of pure C_3S and alite. However, in the case of OPC , the deceleration period seems to depend more on the w/c[150], while for C_3S it only has a little impact. The different behavior may be due to the different particles size distribution between pure C_3S and OPC.

4.5.3 μic simulations

It is remarkable that the input of parameters in line with experimental observations can capture the differences in kinetics until well after the peak maximum. This simulation study supports the hypothesis that the variations in C-S-H morphology produced by the dopant ions results from differences in the nucleation and growth rate and are the main reason for the changes in hydration kinetics. The modeling platform μic is a powerful tool to estimate the kinetic of a hydration reaction and can well capture different changes in the system. The model uses similar inputs as the model proposed by Garrault and Nonat[51], the main differences are that in this case all inputs parameters are estimated on images from pastes samples with a w/c of 0.4 instead of system in diluted conditions and that it also considers the shape of C-S-H.

The lack of agreement in the deceleration regime, arises partly from the incomplete consideration of impingements as already pointed out by Bishnoi[140]. In the model, the equations are edited for planar surface and are used for spherical ones.

The calculated values of the G_{out} are far below the ones required to completely fill the pore space as evaluated by Bishnoi[107;139]. As discussed above, other mechanisms are limiting the rate of reaction in the later part of the deceleration period. Especially, the growth of the needles seems to be much slower beyond the main hydration peak, thus the parameter G_{out} should be decreasing with time, which is not the case in the used version of the model. As needles appear to be cones rather cylinders, and their packing density were increasing during hydration, the minimal density and densifying kinetics parameters (ρ_{min}, k_{den}) were reproducing these aspects. The density was increased between ρ_{min} and ρ_{max} using a sigmoid function of time, which may not be correct.

4.6 Summary

This chapter focus on the acceleration period and gives new insight to the parameters controlling the reaction at this stage. The main findings are listed bellow:

- C-S-H growth controls the reaction during the acceleration period. C-S-H grows as needles outward grains until a certain length. The length appears to be similar for all samples having the same water to cement ratio. In the presence of zinc, the length of needles was increased

- The surface is progressively covered by hydrates during the acceleration period until being completely covered at the moment of the maximum heat flow. It is believed that the lack of surface for precipitation of C-S-H is limiting the reaction at this stage. It is proposed that a transition in the growth mode of C-S-H occurs at the maximum heat causing the deceleration period. It also would explain the transition from the outer product to the inner-product.

- The specific surface area does not influence the intrinsic C-S-H needle growth rate. However it influences the overall hydration kinetics, since C-S-H precipitates on a surface.

- Calorimetry results revealed that all the parameters that influence the main hydration peak, such as the water to cement ratio, the particle size distribution the presence of ions are related to a modification of the nucleation and growth rate of C-S-H.

- Careful consideration of the geometry of the products could be used to successfully model the kinetics of early hydration. The key to the revised model is the needle like growth of C-S-H.

5 Deceleration period

The previous chapters were focused on the kinetics of C-S-H formation and the different parameters influencing its growth rate. In this chapter, the focus lies on the CH and C-S-H composition and morphology in different C_3S blends. Two sets of systems were studied: in the first one the water to cement ratio was varied, in the second one, a blend of C_3S with limestone was prepared to study the filler effect. These two systems are chosen in order to evaluate the impact of the space on the development and composition of C-S-H.

The hydration was stopped at the maximum heat flow, after 1, 7 and 28 days. TGA was used to determine the amount of Portlandite formed and SEM in BSE mode was used to study the morphology of the Portlandite clusters in the different systems. STEM was used to follow the evolution of the microstructure and EDX analyses were done to follow the evolution of the C/S. The C/S ratios obtained were compared with the Portlandite content.

5.1 Literature review on the morphology and composition of CH and C-S-H

C-S-H results from the reaction of C_3S with water during alite hydration, according to equation 5.1:

$$C_3S + (3\text{-x-n})H_2O \longrightarrow C_x\text{-S-H}_n + (3\text{-x})CH \tag{5.1}$$

Calcium silicate hydrate (C-S-H) has a variable composition. The most important component in this variability is the calcium to silicon ratio. A wide range of values have been measured for different systems. First, a review of the experimental measurements of the calcium to silicon ratio in different systems is presented. Second, the different models developed to explain these values are discussed.

5.1.1 C/S in pure pastes determined by transmission electron microscopy

The composition of C-S-H has been studied by microscopy techniques since the 1940s, as reviewed by Richardson[151]. The advantage of using transmission electron microscopy is to have local information about the morphology and composition of C-S-H. The sample preparation is difficult, as special care is required in order to avoid sample damage. As C-S-H contains bound water, it is susceptible to damage, mainly by heating, but also by irradiation[152]. However, heating damage is the most frequent for C-S-H, resulting in bubbles in the structure as reported many times[151;153;154]. This heating may be avoided by limiting the electron dose applied to the paste. The electron dose can be limited by using low beam currents, short observation times or scanning mode in TEM.

Richardson and co-workers[153;155–157] investigated the composition of C-S-H by TEM EDX in different pure OPC or C_3S pastes. Pastes with a water to cement ratio of 0.4 were studied, hydrated from 1 day to 30 years. The samples were hydrated sealed in plastic boxes and cured in plastic bags at 20 °C. For each paste, calcium and silicon ratio was measured in the inner and outer product. Figure 5.1 (a) shows the results for the inner product of the different pastes.

(a)   (b)
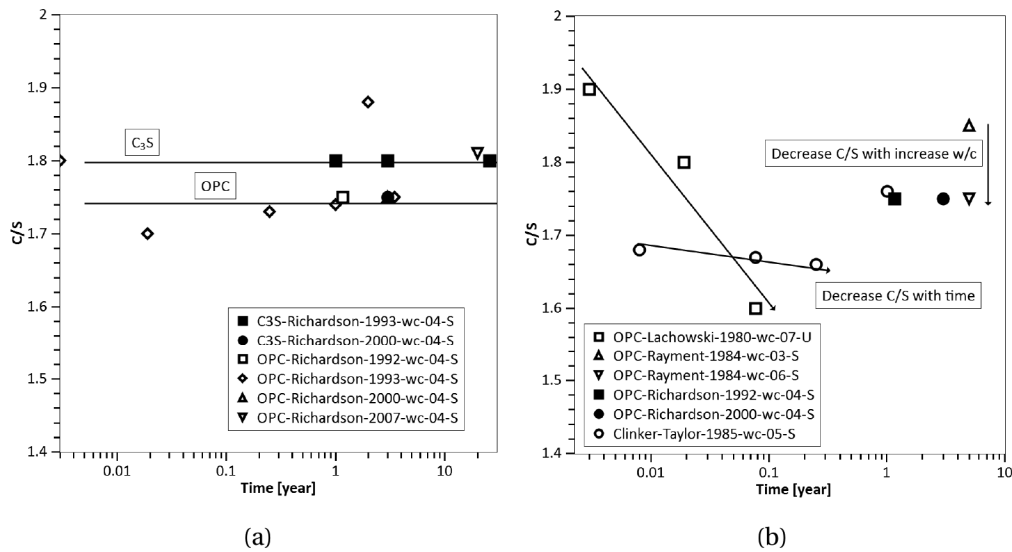
Figure 5.1: (a) Evolution of the calcium to silicon ratio for different OPC and C_3S pastes at a w/c of 0.4, sample cured sealed at 20 °C. Data from Richardson and co-workers[153;155–157]. (b) Evolution of the calcium to silicon ratio for systems with different water to cement ratio. Data are from several workers[155;156;158–160]. S stands for sample cured sealed and U for samples cured underwater.

The C/S vary between 1.7 and 1.9, but there is no tendency in the evolution with time. The oscillations in the values are indicative of the intrinsic error of the measurement technique. However, the values for C_3S paste seem slightly higher than for cement paste. This can be explained by the fact that in pure C_3S there is only calcium and silicon, while in cement

paste other ions such as aluminium are incorporated in the C-S-H structure replacing silicon ions[120].

Other analytical electron microscopy studies were done on pastes hydrated with different water to cement ratios[158–160]. Some of the samples were hydrated sealed[155;156;160], part was hydrated underwater[158]. Figure 5.1 (b) shows the evolution of the C/S for OPC pastes with different w/c values.

From these data, a decrease of the calcium to silicon ratio with time is observed for higher values of w/c. There is no published explanation for the observed decrease of C/S. To understand how the C/S in C-S-H can vary, an understanding of the C-S-H atomic structure and the different models to describe it is required.

5.1.2   Models to describe C-S-H atomic structure

Figure 5.2 shows the evolution of the C/S in C-S-H with the content of Ca in solution and with the C/S in solution, from several authors[161–164]. A drastic increase in the C/S is observed when the content of calcium in the liquid is above 20 mM (Figure 5.2 (a)). From these observations, it was proposed that the equilibrium composition of C-S-H in a saturated lime solution was about 1.5. It is important to emphasize that in C_3S paste the concentration of calcium is around 22 mM, both Portlandite and C-S-H coexist and the values of C/S are around 1.8. This evidence that a certain equilibrium between kinetics and thermodynamic is formed in paste, which would influence the C/S values.
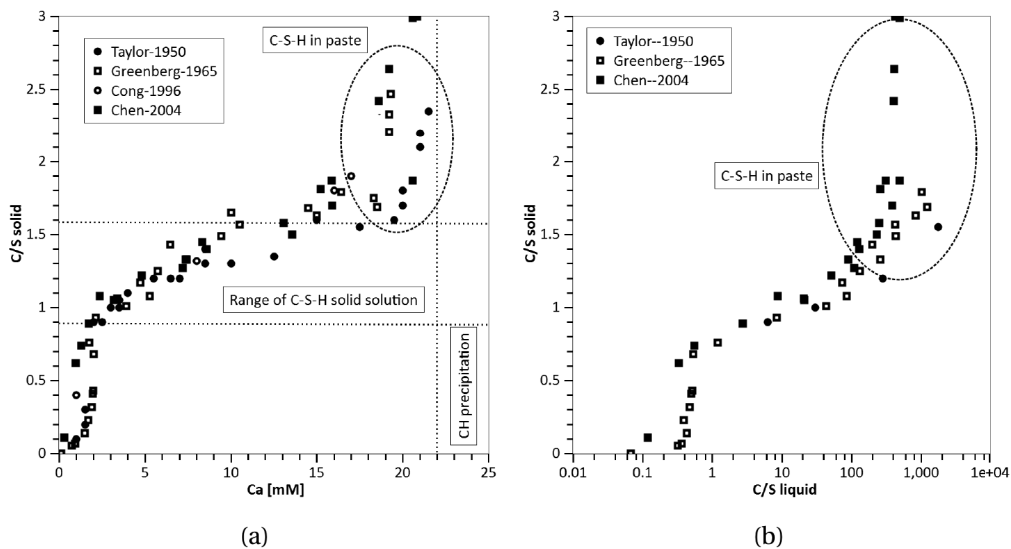
Figure 5.2: (a) Evolution of the C/S in solid as a function of the Ca content in the liquid (b) Evolution of the C/S in solid as a function of the C/S in the liquid. Data from solubility experiments in[161–164].

C-S-H is composed by calcium oxygen sheets covered on both sides by chains of silica tetrahedra (main layer) separated by an interlayer space, which contains water molecules[1]. C-S-H denotes the family of calcium silicate hydrates and is a poorly crystalline material. Two different natural minerals with similar composition are used to describe its atomic structure, tobermorite[165] and jennite[166]. These structures are composed of infinite layers of calcium and oxygen with linear chains of silica tetrahedra, which coordinate with a central calcium octahedra. Every third tetrahedron is not coordinated with the calcium octahedron and bridges two adjacent pairs of tetrahedra. Figure 5.3 shows crystal structure for tobermorite and jennite. The C/S ratio is 0.83 in the case of tobermorite and 1.50 in the case of jennite. These values are some what below the values measured for C-S-H in pure cement paste.

(a)

(b)
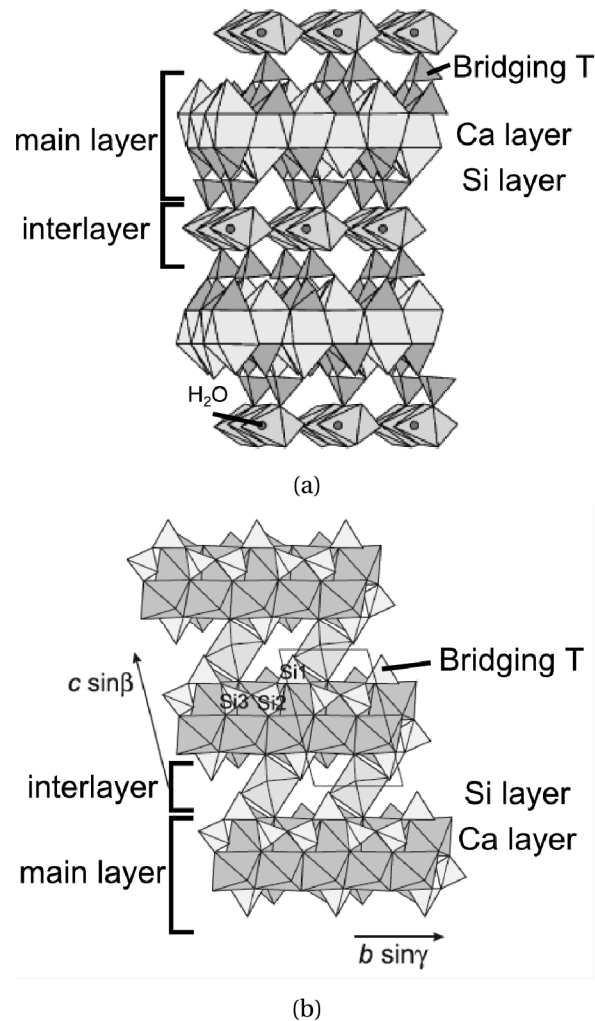
Figure 5.3: Crystal structures of (a) Tobermorite from Bonaccorsi[165], (b) Jennite from Bonaccorsi[166].

In cement paste, the mean chain length varies from 2 for young paste to 5 for mature paste and can even be higher in the presence of SCMs and the C/S varies between 0.7 to 2.3[106].

Tobermorite and jennite can be used to describe C-S-H, but with some modification of their structure, since C-S-H have a shorter chain length and a higher calcium to silicon ratio. If all bridging tetrahedra are removed from tobermorite and jennite structures, calcium silicate hydrates end up with a chain length of 2 and a C/S of 1.25 and 2.20 respectively.

If all the bridging tetrahedra are removed and all protons replaced by calcium ions in a tobermorite-like structure, the resulting C/S is 1.5. So for C-S-H with a C/S lower than 1.5 is agreed that the model to describe its atomic structure is based on a tobermorite-like with elimination of part of the bridging tetrahedra and substitution of part of the protons by calcium ions.

For C/S ratio above 1.5, different models have been proposed to describe C-S-H atomic structure, based on these two minerals and the removal of bridging tetrahedra. Richardson reviewed and described all the different models proposed[167]. There are mainly two categories of models. The first one is based on a mixture of the two minerals. The second one is based on tobermorite with all the bridging tetrahedra removed, all protons replaced by calcium ions and an addition of Ca-OH groups.

For the first category, Taylor[168] suggested that C-S-H is a mixture of tobermorite and jennite. In both jennite and tobermorite, the bridging tetrahedra are removed and the charge is balanced by a OH group. This keeps the net charge unchanged and the omission of the bridging tetrahedron does not require any change in the Ca amount in the interlayer.

For the second category, the position where the Ca-OH groups are added is still debated. Cong and Kirkpatrick[163] suggested that Ca-OH groups can replace some silica chains in the main layer of tobermorite. Nonat and Lecoq[169] suggested that Ca-OH groups are introduced in the interlayer.

Richardson[106] summarized these two points of view and named them the tobermorite-jennite T/J and the tobermorite- solid solution calcium hydroxide T/CH respectively. A general formula was developed to describe the C-S-H composition and atomic structure, which describes all the possible combinations of isolated silica chains of varying length, with a variable number of hydroxyl groups attached to Si atoms in solid solution with a variable amount of CH.

Experimental evidence suggests that the tobermorite-like structure with addition of Ca-OH groups is more likely to describe C-S-H atomic structure. XRD[170;171] and NMR[172] studies of synthetic C-S-H showed no evidence for signal of jennite and only tobermorite-like structure was detected. At high C/S (>1.5) synthetic C-S-H also contain Portlandite[170;171]. Experiments on carbonation of C_3S by Groves et al.[173] and OPC pastes by Richardson et al.[174] showed in both cases that during carbonation, regions of outer-product were densified by the presence of carbonate microcrystal, without impacting the fibrillar morphology of C-S-H, but decreasing their C/S ratios. These results indicates that calcium can easily be removed from C-S-H, without changing it morphology. Earlier study of Stade[175] showed that calcium was easily

leached from a C-S-H with a high C/S leaving a C-S-H with a C/S around 1.25.

5.1.3 Portlandite growth

Portlandite growth and morphology can be modified by several factors, such as the size of the nuclei, the concentration of nuclei, the saturation level of the solution, the temperature and the other ionic species present in the solution can influence it.

Studies on CH crystal growth show the importance of these parameters. Tomazic et al.[176;177] studied the crystallization of calcium hydroxide in aqueous solution. The experiments indicated that the growth rate of calcium hydroxide crystals depends of the initial size of the seed, the amount of seed added into solution and the saturation level of the solution. It was shown that for higher supersaturation level, the growth rates was higher. Hedin[178] showed that the growth rate of a crystal immersed in a solution with a concentration increasing and then decreasing, was higher for larger crystals in a same concentration. The plot of the growth rate versus the concentration showed an hysteresis loop. This result suggested that the crystal surface is activated at higher concentration and inactivated at lower concentration. In these experiments, the concentration limit to initiate CH growth was around 23 mM of Ca in solution. Galmarini et.al[179] showed that ionic species present in the pore solution of hydrating cement, such as silicates, sulphates and aluminates can change the morphology of Portlandite crystals formed. The addition of silicates has the most pronounced effect on the crystals growth. The resulting crystals were large irregularly shaped agglomerates. This results would indicate that the presence of ions inhibit growth some crystallographic faces, while growth on other is promoted.

In paste, these factors also play an important role in the formation and morphology of Portlandite. In alite and C_3S pastes, Portlandite forms fewer, large, convoluted randomly distributed clusters, which engulf anhydrous grains, while in cement paste, Portlandite forms numerous small particles evenly and closely distributed in the matrix, with two shapes: thin hexagonal platelets or random clusters[180–182]. Gallucci and Scrivener[181] explained the different morphology of Portlandite by the presence of gypsum and alumina. Gypsum is thought to promote the nucleation of Portlandite. Berger and McGregor[183] showed the influence of the temperature on crystals of Portlandite during hydration of C_3S at different temperature. The size of the CH crystals increased with decreasing temperature, while the number of crystals decreased with the decreased of temperature. This study also showed that the space available played an important role in the growth of CH. The increasing w/c of the paste increased the time to initiate nucleation because critical supersaturation needed to be reached, but had no clear effect on the growth rate. However more elongated crystals were observed.

5.2 Systems studied

Same pastes of C_3S with a water to solid ratio of 0.4 and 0.8 and mix of 60% C_3S with 40% limestone with a water to solid ratio of 0.4 were used as described in previous chapters. The paste with limestone had an equivalent w/c of 0.67. The pastes were hydrated until 28 days underwater, few drops of saturated lime solution were added on the top of the paste after introducing them in plastic containers.

5.3 Evolution of Portlandite

5.3.1 Evolution of the Portlandite content with time

TGA were done to follow the Portlandite and limestone content in the samples (Figure 5.4). The TGA showed a higher Portlandite content at all times in the sample with a higher w/c. The analysis also revealed a continuous increase in the Portlandite content with time for the sample with a w/c of 0.8. For the sample with a w/c of 0.4, the increase of the Portlandite content is low after 24h.
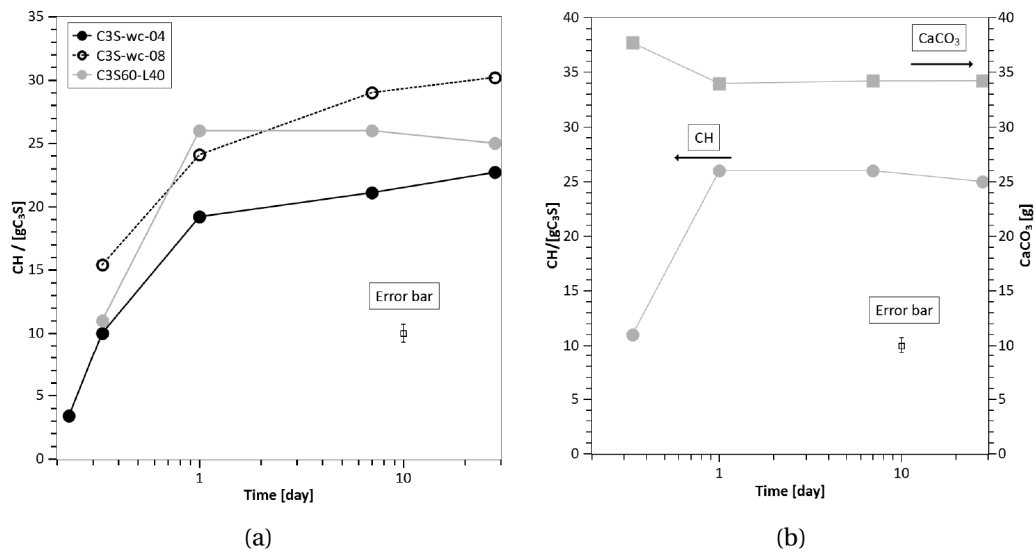
Figure 5.4: (a) Evolution of the Portlandite content with time, (b) Evolution of the Portlandite and the limestone content with time, for the blend of 60% C_3S and 40% limestone. The error bar represents the measurement error of the instrument.

The sample with limestone has no more increase in Portlandite content after 24h, because the C_3S reaches 100% degree of hydration. The quantification of the limestone content shows a consumption of limestone until one day (Figure 5.4 (b)), confirming the dissolution of limestone during hydration and probably increasing the calcium available in solution. After one day, about 15% of the limestone present has reacted. From this point, the amount of limestone is stable around 34% because the reaction stopped, since C_3S reaches 100% degree

113

of hydration.

The calcium to silicon ratio in C-S-H can be calculated from mass balance in equation 5.1, using the amount of Portlandite by TGA, the degree of hydration (DoH) estimated from calorimetry.

Table 5.1: Calculated C/S from TGA and calorimetry. Error on C/S 5 %.

	C_3S (DoH) [%]		CH (TGA) [g/gC_3S]		C/S [at%]	
	peak	24h	peak	24h	peak	24h
C_3S 0.4	22	60	10	19	**1.60**	**2.01**
C_3S 0.8	29	65	15	24	**1.41**	**1.84**
60% C_3S - 40% limestone	26	99	11	26	**1.81**	**2.19**

These calculations predict a lower C/S ratio in C-S-H for the sample with a higher w/c. It also predict a higher C/S for the sample with limestone. The predicted values at the maximum heat are lower than the usual values for C/S. This can be due to the fact that the degree of hydration is calculated from the calorimetry curve and the amount of Portlandite is calculated from TGA after hydration stop. Since at this point the reaction is fast for C_3S it can have a mismatch between the value of the DoH and the time at which the hydration was stopped for the TGA measurements. Slight change in the amount of Portlandite or in the degree of hydration has a strong impact on the calculated C/S values.

5.3.2   Portlandite morphology

The morphology of Portlandite clusters after 24h of hydration is shown by Figure 5.5.

It is observed that dilution has a little effect on the Portlandite morphology. The clusters appear to be slightly more elongated in the system with a w/c of 0.8 than in the system with a w/c of 0.4. In the presence of limestone, many more clusters are observed, but they are much smaller.

The Portlandite formation in these samples was compared with the Portlandite formation in the sample thermally treated 1h at 850 °C as indicated by Figure 5.6.
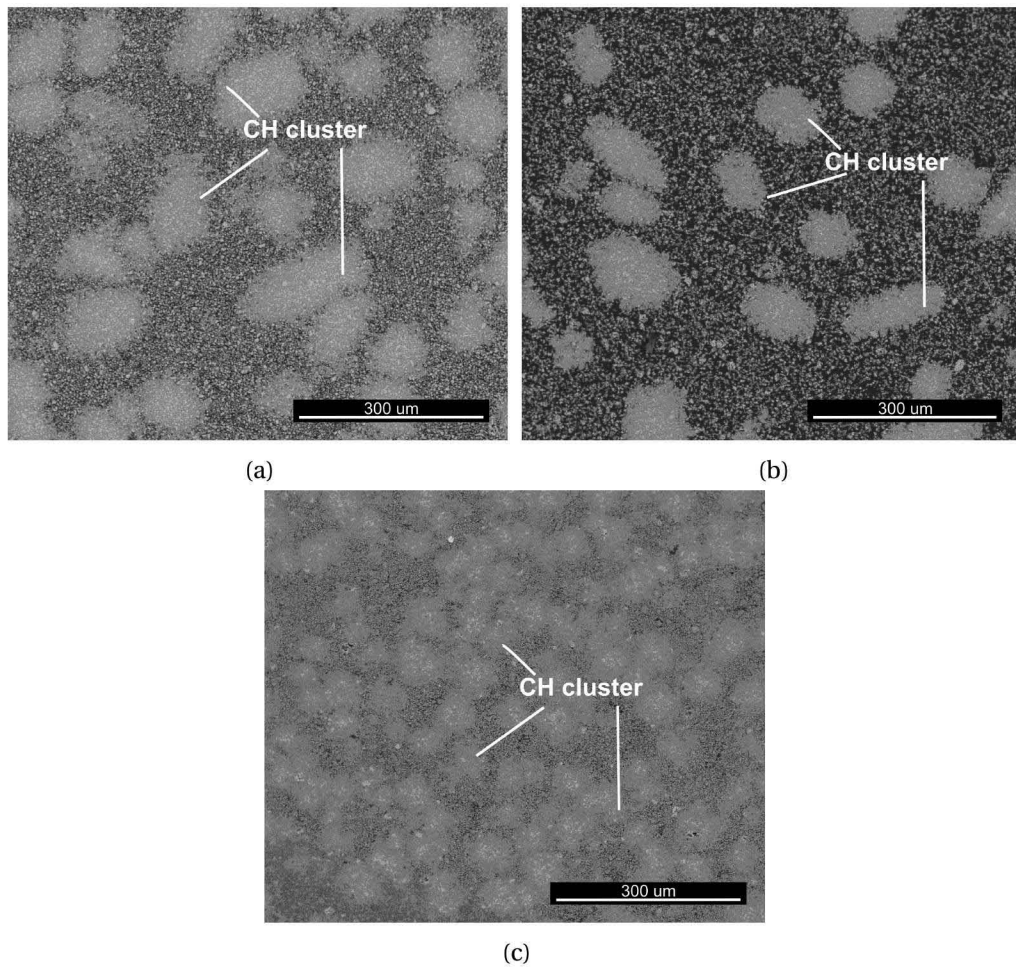
Figure 5.5: Microstructure development after 24h, (a) w/c 0.4, (b) w/c 0.8 and (c) 60% C_3S 40% limestone.
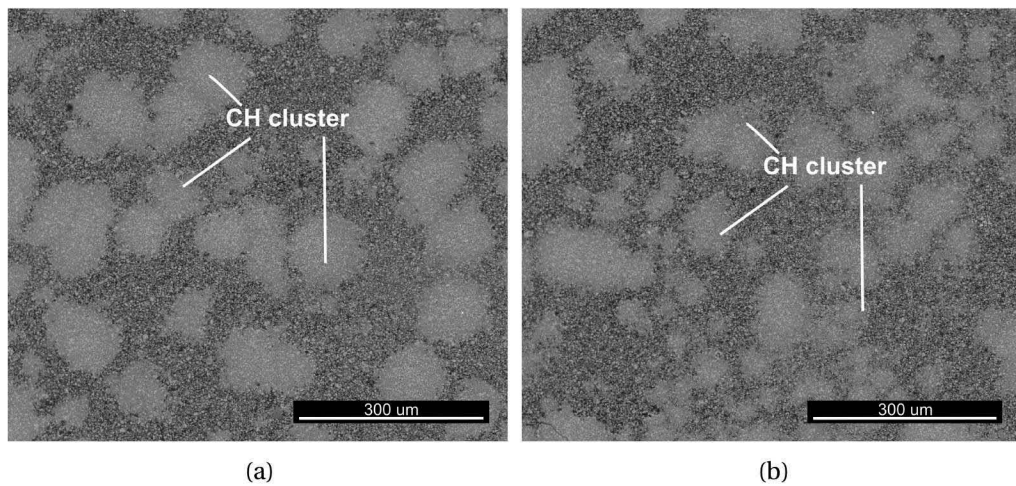
Figure 5.6: Microstructure development after 24h, (a) reference C_3S, w/c 0.4 and (b) annealed C_3S 1h at 850 °C w/c 0.4.

The number of cluster per mm^2 was determined for each system and results are indicated in Figure 5.7. These experiments were done on a different batch of C_3S, but there is no differences
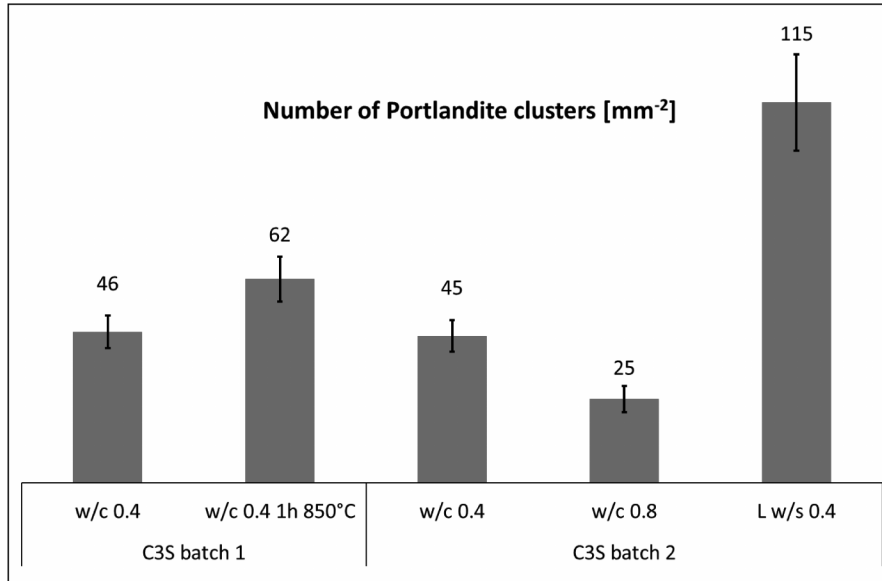
Figure 5.7: Number of Portlandite clusters after 24h of hydration for C_3S and annealed C_3S 1h at 850 °C from batch 1, C_3S w/c 0.4, C_3S w/c 0.8 and blend 60% C_3S 40% limestone from batch 2. The error bar represents the dispersion of measurements in several images.

between the same paste of C_3S with a w/c of 0.4. After annealing, a bimodal distribution of Portlandite clusters is observed with the larger with the same size as in the reference samples and plenty of small clusters, as shown in Figure 4.8. The formation of these small clusters appeared from the main hydration peak.

The annealed sample has more Portlandite clusters due to the appearance of these small clusters from the maximum heat. During the acceleration period, a lower number of clusters was observed. The sample with higher w/c ratio has less clusters, despite a higher amount of Portlandite per gram of C_3S. The sample with limestone has a large number of clusters.

5.4 Evolution of the C-S-H with time

5.4.1 Evolution of the chemical composition of C-S-H with time

The chemical composition of C-S-H was investigated by EDX analysis. Figure 5.8 shows the evolution of the calcium to silicon ratio in the three samples with time. The first measurement times of the series in Figure 5.8 are not the same, because the hydration was stopped at the moment of the maximum heat flow, which is at 6 h for the sample with limestone, 8 h for the sample with w/C of 0.4 and 11 h for the sample with a w/c of 0.8. The other points are after 24 h, 7 d and 28 d. A decrease of C/S is observed between the main hydration peak and 24h for all samples.
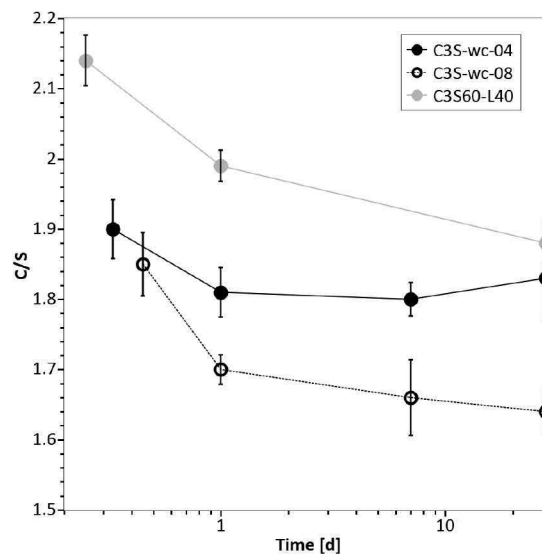
Figure 5.8: Evolution of the calcium to silicon ratio with time. The error bar represents the dispersion of quantification in several maps.

In the case of w/c 0.4, after 24h the C/S remains constant with a value around 1.8, which is in good agreement with previous work by Richardson[153;156]. For the higher w/c, the C/S ratio seems to continuously decrease with time, which corresponds to previous observations of Lachowsky on OPC with a w/c of 0.7[158] and Taylor on clinker with a w/c of 0.5[160].

The limestone sample also shows a decrease of C/S ratio with time. The measurement at 7 days gave a value out of range (C/S = 2.5) and was removed from the graph. This sample suffered from the preparation and large homogeneous areas were not found to do a proper EDX analysis. In general the C/S values in the presence of limestone are higher than for pure C_3S pastes. Zajac et al.[184] observed also higher values of the C/S in C-S-H in the presence of limestone.

When the two samples with different w/c are compared, a decrease in the C/S values for higher w/c is observed at all times. Rayment observed similar trend in OPC samples hydrated for 5 years[159]. Muller et al.[185] measured by ^{1}H NMR white cement pastes and found a decrease of the C/(S+A) for more diluted systems. Figure 5.9 shows the comparison of the evolution of C/S measured by STEM-EDX in C_3S paste at different w/c with the evolution of C/S measured by ^{1}H NMR by Muller et al.[185] in a WPC. Figure 5.9 also shows the evolution of the C/S in a C_3S paste hydrated with a w/c of 1.2.

For a same w/c (in this case 0.4) the C/S in the WPC in lower than the C/S in the C_3S. This can be explain by the fact that WPC has C_3S and C_2S reacting which lower the amount of calcium compared to a pure C_3S paste. The ^{1}H NMR study of Muller et al.[185] show a rapid decrease of the C/S with the w/c. Figure 5.9 (b) shows the evolution of the C/S in three C_3S paste with w/c of 0.4, 0.8 and 1.2. From Figure 5.9 (b) it is observed that the C/S decreass with

(a)   (b)
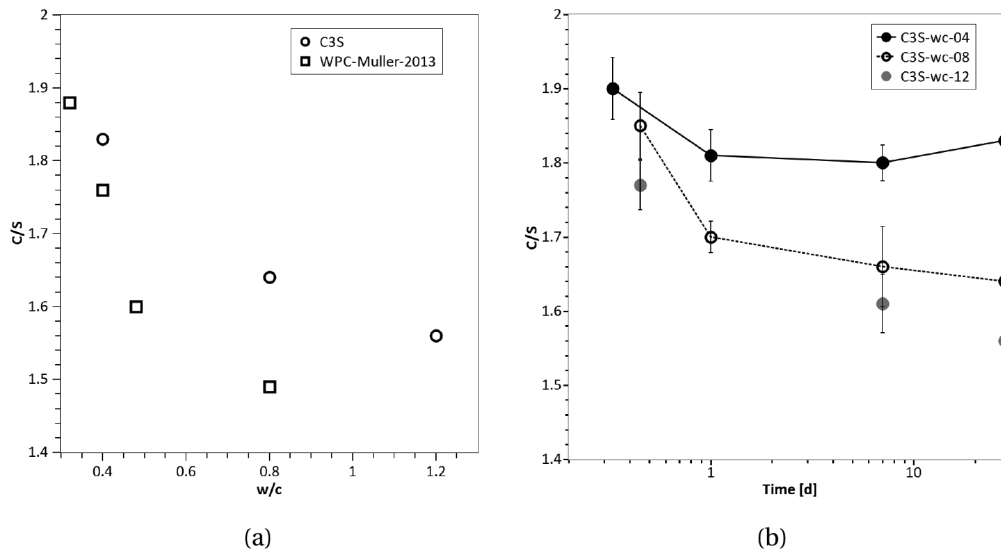
Figure 5.9: (a) Comparison of the effect of the w/c on the C/S ratios for C_3S with the C/S ratios for white cement of Muller et al. [185] for pastes hydrated for 28 days. (b) Evolution of the C/S with time in C_3S samples with a w/c of 0.4, 0.8 and 1.2. The error bar represents the dispersion of quantification in several maps.

the increase of w/c from 0.8 to 1.2, but with lower proportion than between 0.4 and 0.8. It is proposed that their is a strong dependence of the C/S with the w/c for lower values and then for higher values, the decrease of C/S with w/c is more progressive, as indicate by dashed lines in Figure 5.9 (a).

If it is assumed that all silicon is consumed by C-S-H, a decrease of the C/S ratio indicates a decrease of the calcium content.This would indicate that if there is less calcium in the C-S-H, there is more calcium in the Portlandite. Since in pure C_3S paste the only other hydrates present is Portlandite, the remaining calcium should by consumed by Portlandite. TGA analysis showed that the Portlandite content was higher for the sample with the higher w/c (Figure 5.4 (a)). The prediction of the C/S from TGA and calorimetry curves indicated a decrease of the C/S in C-S-H for the sample with the higher w/c, which is in good agreement with the EDX measurements.

5.4.2 Evolution of the morphology of C-S-H at later age

To follow the evolution of the microstructre at later age, STEM images were acquired for each system after 7 d (Figure 5.10) and 28 d (Figure 5.11).

After 7 days, a general densification of the microstructure is observed for the pure C_3S paste, while in the case of limestone, little evolution is visible. In this system the reaction is completed after 24 hours. Some Portlandite crystals are visible in between grains.
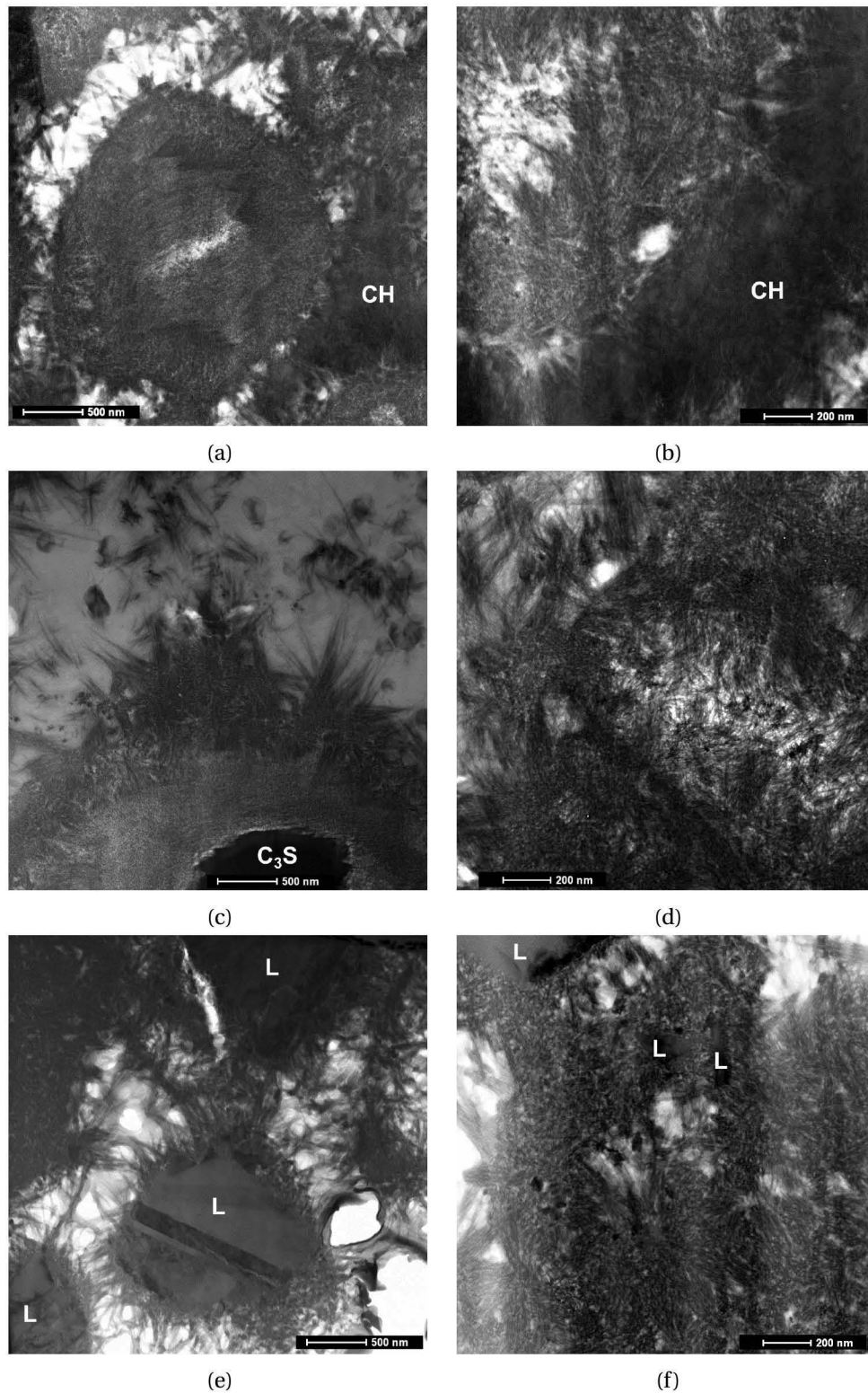
Figure 5.10: STEM images of (a) and (b) w/c of 0.4, (c) and (d) w/c of 0.8 and (e) and (f) C_3S blended with 40% limestone, after 7d of hydration. C_3S indicates C_3S grains, CH Portlandite and L limestone. The sample with w/c = 0.4 has its microstructure full of hydrates, while the sample with w/c = 0.8 has still some space.
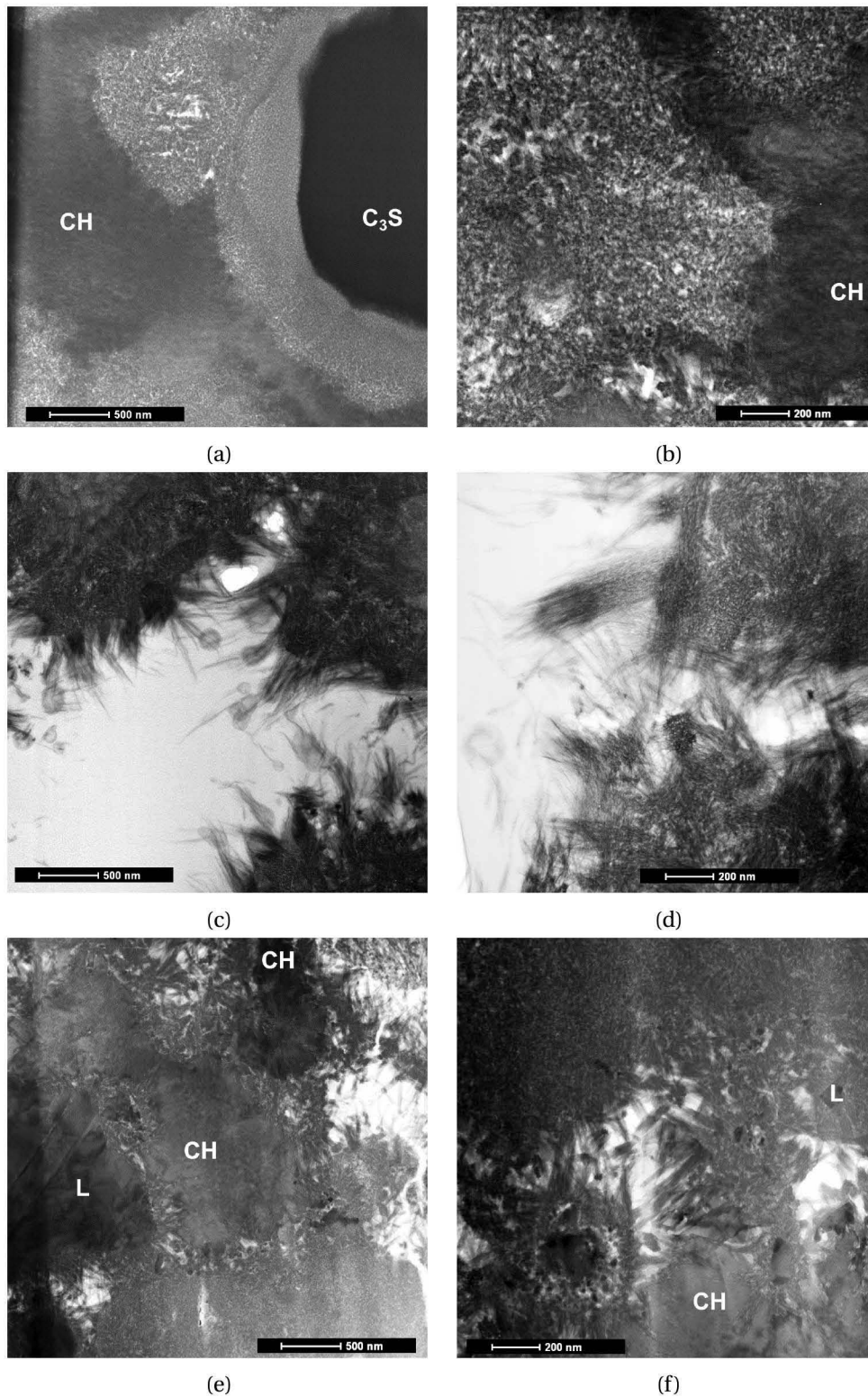
Figure 5.11: STEM images of (a) and (b) w/c of 0.4, (c) and (d) w/c of 0.8 and (e) and (f) C_3S blended with 40% limestone, after 28d of hydration. C_3S indicates C_3S grains, CH Portlandite and L limestone. A general densification of the microstructure is observed for all samples.

In Figure 5.10 (d), the contour of the C_3S grains fully reacted is visible. The outer-product coming out from the original surface of the grain is visible as well as the dense inner-product close to the original surface. However, the morphology in the middle part of the grain is similar to the one of outer-product. It is proposed that, when the grain has completely hydrated, there is again space for C-S-H nuclei to grow and product forms fibrils, like needles in the outer-product. This microstructre can be compared with the "Hadley grains"/shell formation in cement samples, for small grains a space may remain[186].

By one month of hydration (Figure 5.11), the microstructure of w/c 0.4 is completely filled. For this sample, it is difficult to distinguish between inner- and outer-product, but the first one seems more densely packed that the second one. In the sample with a w/c of 0.8, the inner part of the completely reacted grains seems denser than at 7 days and looks similar to the w/c 0.4. The inner-product seems more uniform for this sample than for the sample with a w/c of 0.4, which looks isotropic.

It is interesting to note that C-S-H needles that are embedded in CH crystals and not damaged as visible on Figure 5.12.
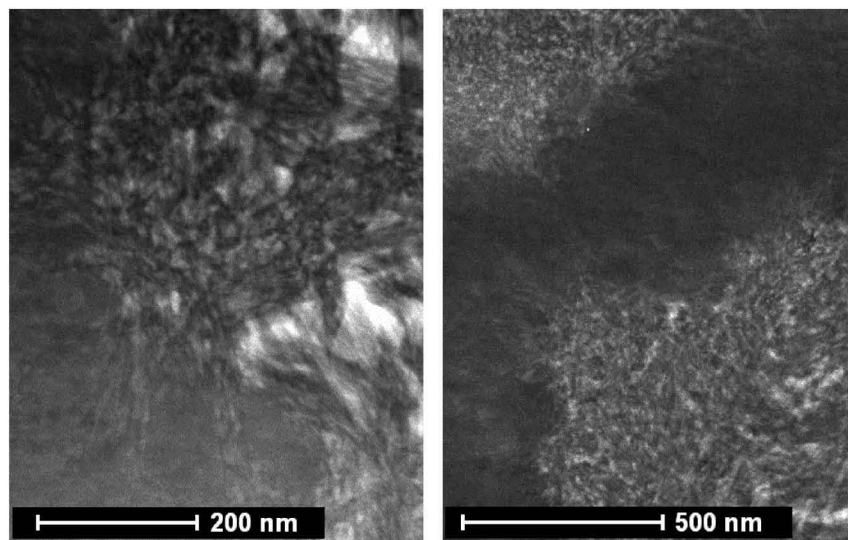
Figure 5.12: C-S-H needles embedded in CH crystals for C_3S w/c 0.4 after 28 days.

There may be significant differences in the morphology of C-S-H between a pure alite or C_3S paste and an OPC paste[132]. First, because an OPC paste contains additional phases and hydrates growing, and second because in an OPC paste there is the formation of shell, already after 4h[132]. For example, in clinker sample shell was already observed at the maximum heat, as indicated by Figure 5.13.
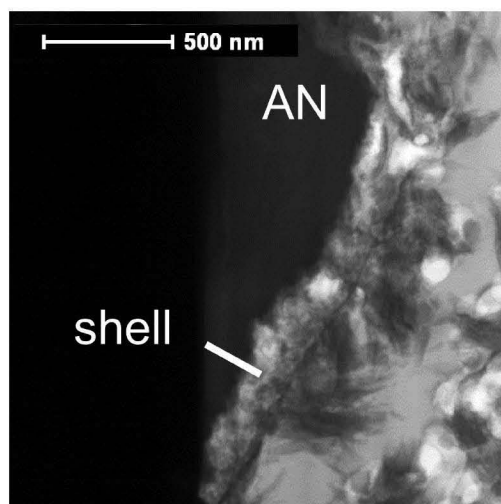
Figure 5.13: Shell formation on clinker ground by Mc-Crone micronizer after 10 hours of hydration.

5.5 Discussion

There is a a strong link between the formation of C-S-H and Portlandite, as when the calcium to silicon ratio in C-S-H decreases, the Portlandite content increases. What is initiating this mobility of calcium is still unclear. Is it because more Portlandite forms in a more diluted system, or is it because C-S-H composition is closer to the thermodynamic equilibrium in the more diluted system?

In the more diluted system, there is no reasonable explanation for an increase in Portlandite growth. The system would reach the same supersaturation degree, as Barret measured same supersaturation degree in solutions with a w/c ranging from 0.35 to 100[187]. SEM images show no evidence of larger crystals formed in the more diluted systems. The porosity is too large even in the lower w/c for having an impact on the crystallization pressure of Portlandite[188]. In the presence of limestone, the amount of calcium in solution is increased, which increase the nucleation rate of Portlandite. Since there are much more nucleation sites, Portlandite growth is limited and CH clusters are smaller.

It seems more likely that the transfer of calcium is initiated by C-S-H. Experiments of Brown[30] shows that in the first minutes of hydration, the amount of calcium in solution is higher for the lower w/c, despite the precipitation of C-S-H. The amount of silicon is already very low indicating the precipitation of C-S-H. C-S-H precipitates from solution with a high calcium concentration, due to the necessity to reach the supersaturation degree with respect to Portlandite. The higher C/S is in the liquid, the higher the C/S is in the solid. Since Portlandite and C-S-H are thermodynamically equilibrated when the C/S in C-S-H is at 1.5, for systems with C/S higher than 1.5, the system would tend to approach this equilibrium. Figure 5.14 shows a schematic representation of equilibrium between CH and C-S-H. One can imagine

that C-S-H formed initially, is metastable, with a composition far from equilibrium. Then the system would tend to approach this equilibrium, which would explain the observed decrease of C/S in C-S-H with time. In the more diluted system, the reaction reaches faster a higher degree of reaction, which allow the system to tend toward the thermodynamic equilibrium.
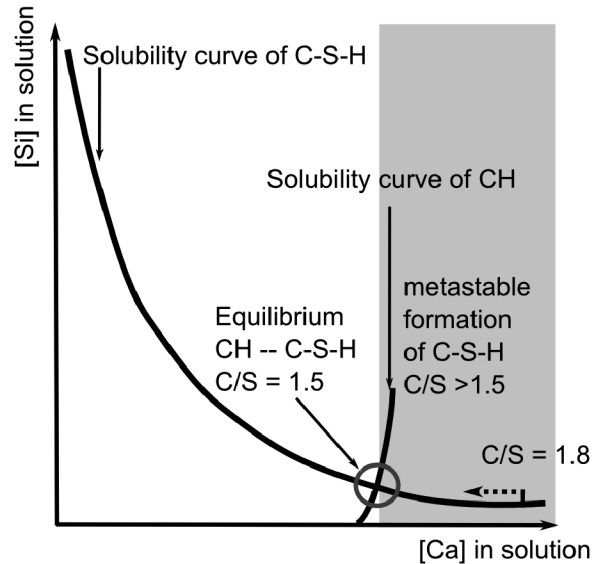
Figure 5.14: Schematic representation of solubility curves of CH and C-S-H. In paste mestastable C-S-H is formed with C/S > 1.5

As chain length of C-S-H with C/S between 1.4 and 2 is similar[163], it would not be expected that the chain length change with the increase of w/c from 0.4 to 0.8. Thus it is not expected that there are longer chains formed with less calcium. It seems that some calcium can easily be removed from C-S-H without changing its morphology, since in the sample with a w/c of 0.8 fibrils are observed even if the C/S is lower than in the sample with a w/c of 0.4. These observations support the C-S-H model of a tobermorite-like structure with Ca-OH group in the interlayer, in order to insure mobility for calcium. Figure 5.15 shows a schematic representation of the atomic structure for a C-S-H with a C/S > 1.5, and with a chain length about 2.

In term of morphology, for all samples C-S-H in the outer-product has fibril morphology, whatever its C/S. The inner product is similar as well, but seems denser in the lower w/c. The formation of a fibril-like product in the middle of the fully reacted small grains can be interpreted either by the formation of hollow shell, either by the formation of a product like outer-product due to the space left from the grain. Kjellsen and Justnes[180] observed formation of low density product in the middle of fully reacted alite and C_3S grains smaller than 5 μm and attributed it to the formation of hollow shell.
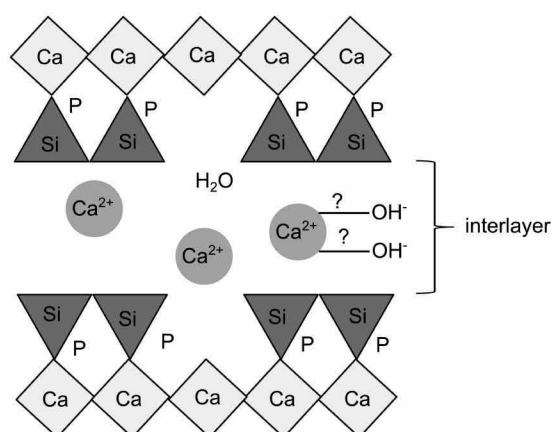
Figure 5.15: Schematic representation of C-S-H, with the calcium oxygen layer, the silicate tetrahedra and the interlayer made of labile calcium, which can be compensated by OH groups, and water molecules.

5.6 Summary

This chapter focused on the Portlandite development, the morphology and composition of C-S-H with time. Two parameters were tested: the dilution and the presence of limestone. The main founding are listed bellow:

- The effects of the dilution were an increase of the degree of reaction and an increase of space in the microstructure

- More Portlandite per gram of C_3S is formed in the more diluted system and in the presence of limestone. The morphology of CH cluster is similar in pastes with different w/c, while smaller clusters are formed in the presence of limestone.

- A decrease of the calcium to silicon ratio in the C-S-H is observed along time for the three systems.

- In comparison, the system with the higher w/c has a lower C/S in the C-S-H and a higher content of Portlandite. The system with limestone has the higher C/S in C-S-H due to the higher amount of calcium in solution.

- There is a a strong link between the formation of C-S-H and Portlandite. As calcium is easily transfered from C-S-H to Portlandite, reducing the C/S in C-S-H without changing its morphology the model of a tobermorite-like structure with Ca-OH group in the interlayer seems to describe the best C-S-H atomic structure.

6 Conclusions and perspectives

This work sheds light on the early hydration mechanisms. New insights were achieved, using the latest developments in microscopy techniques and complemented by conventional techniques such as isothermal calorimetry, XRD and TGA.

6.1 Methodology

Thanks to the latest development in secondary electrons detectors, it was possible to study cement surfaces without carbon coating, avoiding charging effects, using low voltage. This is particularly useful to examine small features, such as etch pits or C-S-H nuclei, whose morphology or size may have been hidden or transformed by the presence of carbon. These techniques also allowed imaging of C-S-H avoiding beam damage.

For TEM, there are two main difficulties regarding the study of cementitious materials: the samples preparation and the beam damage in C-S-H. A method combining mechanical polishing and FIB ion milling microscopy was developed to prepare TEM samples of hydrated cementitious materials. It allowed the preparation of multiple precisely selected regions of interest in a same sample. The microscope settings were optimized in such a way that electron beam damage was minimized. With these two issues overcome, TEM bright field was used to evaluate the defect density in anhydrous gains, after different steps of the sample preparation. STEM images allowed characterization of the structure and morphology of C-S-H. Coupled with EDX detectors, the chemical composition of C-S-H was determined.

The early hydration mechanisms of tricalcium silicate were studied by comparing the evolution of the microstructure followed by microscopy techniques with the hydration kinetics determined by isothermal calorimetry.

6.2 Hydration mechanisms

Mechanism that govern the kinetics in the different periods of hydration are summarized in the following and illustrated by Figure 6.1:

Induction period:

- The observations suggest that the controlling mechanism during the induction period is the dissolution rate. As the defect density and/or the surface roughness are reduced, the duration of the induction period is extended. C-S-H nucleation is observed during the induction period, but has no significant impact on its duration.

- The defects observed in the samples are of two different natures. There are dislocations and stacking faults observed in the bulk samples, but in addition after grinding, there is a damaged layer, which appears at the grain edge. The defect density is reduced by annealing, mainly by removing this damaged layer. The surface structures of the particles is affected by the grinding procedure.

- The ions present in alite affect the nucleation rate and sizes of C-S-H.

- Etch pit formation is observed during the induction period, but it is difficult to quantify due to their heterogeneous distribution over the surface and their small size barely visible with the SEM.

- The end of the induction period coincides with the precipitation of Portlandite. A critical degree of supersaturation needs to be reached to initiate the massive precipitation of Portlandite, explaining the longer duration of induction period for the more diluted system and the same duration when C_3S is hydrated with a saturated lime solution.

Acceleration period:

- The results indicate that the growth of C-S-H controls the reaction during the acceleration period. C-S-H grows as needles outward from grains up to a length characteristic of the system.

- The length of the needles can be influenced by the presence of certain ions. In the presence of zinc, the length of needles is increased.

- The surface is progressively covered by hydrates during the acceleration period. It is completely covered at the moment of the maximum heat flow. It is believed that the lack of surface for precipitation of C-S-H limits the reaction at this stage.

- The specific surface area does not influence the intrinsic C-S-H needle growth rate. However, it influences the overall hydration kinetics, since C-S-H precipitates on surface.

- The presence of limestone has no impact of the growth rate of C-S-H needles, whereas it strongly promotes its nucleation rate, due to a crystallographic effect.

Careful consideration of the geometry of the products could be used to successfully model the kinetics of early hydration using the modeling platform μic. The key to the revised model is the needle like growth of C-S-H.

Deceleration period:

- It is proposed that a transition in the growth mode of C-S-H occurs at the moment of the maximum heat flow, causing the deceleration period.

- A transition from the outer product to the inner-product formation occurs. C-S-H needles continue to grow, but at a much slower rate.

- The water to cement ratio influences the morphology and packing density of C-S-H product.

6.3 Hydrates composition

In alite and C_3S pastes, two hydrates develop, C-S-H and Portlandite. The particularity of these systems is that Portlandite precipitates as clusters, which engulf anhydrous grains. A strong link between C-S-H and Portlandite formation is observed, and appears to be dependent on the amount of water in the system. The observed relations between C-S-H and Portlandite are listed below:

- More Portlandite per gram of C_3S is formed in the more diluted system, while the morphology of their clusters is similar in both pastes.

- This is connected to a decrease of the calcium to silicon ratio in the C-S-H observed in the more diluted system. The C/S in C-S-H is also observed to decrease with time in a each paste.

- It is proposed that calcium is easily removed from C-S-H, suggesting a tobermorite-like structure with mobile calcium in the interlayer. Initially, C-S-H precipitates at high calcium concentration, due to the supersaturation with respect to Portlandite.

- At first, C-S-H is formed under metastable thermodynamic conditions, controlled by the dissolution kinetics. Once Portlandite precipitates, the system tends to reach the thermodynamic equilibrium. C-S-H releases calcium, which precipitates as Portlandite.

6.4 Perspectives

In this work, mainly C_3S and alites samples were studied. As pure C_3S powders have a narrow particles size distribution, with a diameter d_{50} of $3\,\mu$m, it is convenient to prepare TEM samples. Several particles are in the regions of interest and they all have a homogeneous composition. With the adapted sample preparation method and microscope settings, studies on early hydration of real cement pastes are still possible. Many aspects are different between a C_3S paste and a cement paste. First, cement has polyphased grains, thus have several reactions occurring simultaneously during hydration. Second, in cement, particles size distribution range from 0.01 to $50\,\mu$m, which profoundly changes the filling of space.

C-S-H was observed to grow as needles by aggregation of sheets, but the mechanisms by which C-S-H forms at the atomic scale remain unclear. It can be by the assemblage of blocks composed of dimeric silica chains or by the formation of C-S-H atom by atom at the growing part of the needle. The structure of C-S-H is widely studied by atomistic modeling and further work is needed in order to compare models with experimental observations.

Other microscopy techniques, such as STEM tomography and 3D reconstructions should be considered to gain insight on the structure of C-S-H. Structure and pore network at the nanoscale are at major interest, since it controls the permeability of the sample.

The equilibrium between C-S-H and Portlandite was established on the basis of observations on few paste samples hydrated for relatively short period. More systematic studies are needed to fully understand the thermodynamic equilibrium in a paste. With such information, long term properties cementitious materials could be predicted.

Simulations of the hydration kinetics were successfully obtained, using experimental observations as inputs for the modeling platform μmic. Equations are needed to consider the growth of single needles and correctly treat the impingement between neighboring grains. However, the encouraging results open possibility for the prediction of hydration kinetics of more complex systems.
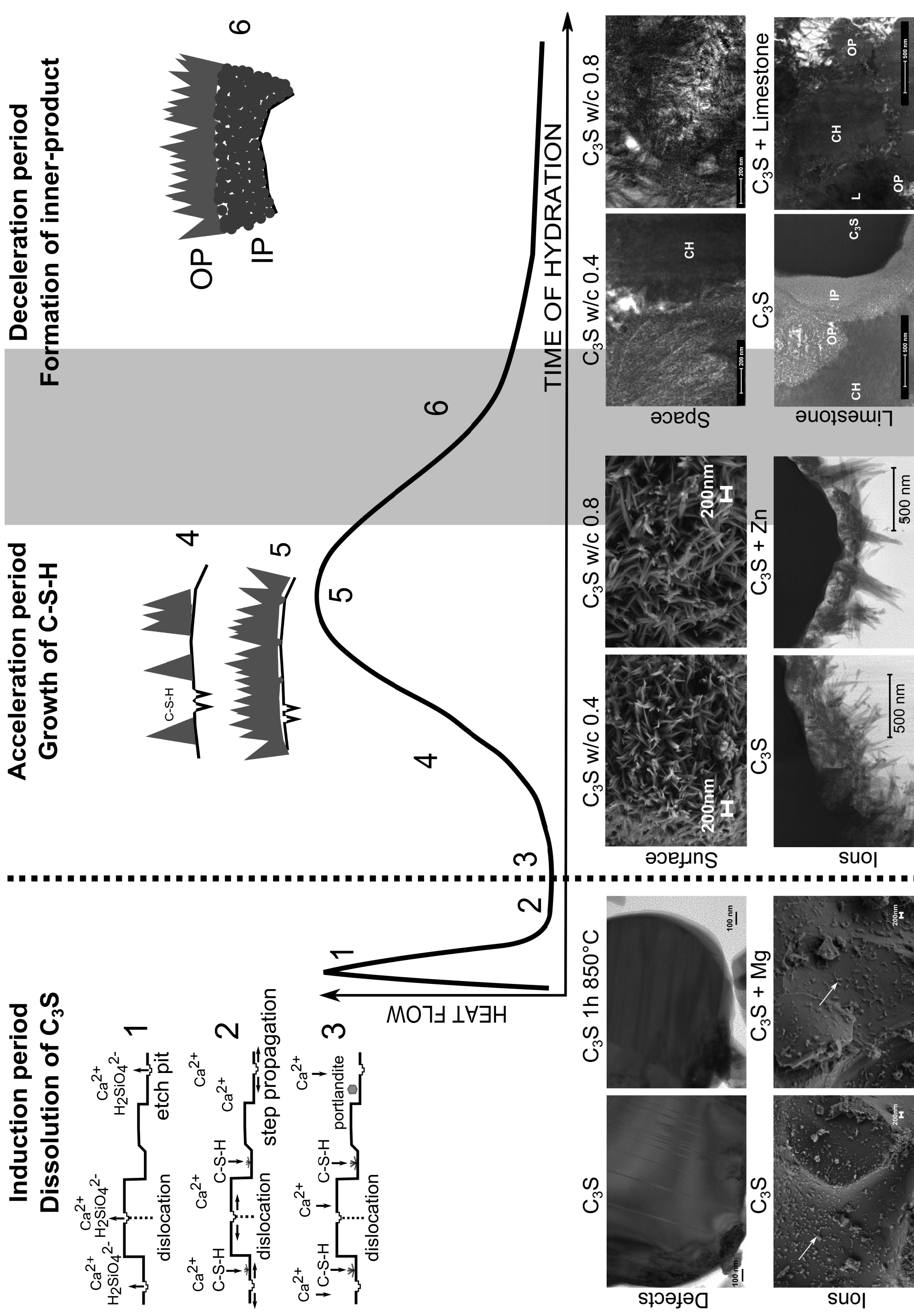
Figure 6.1: Summary of the hydration.

Bibliography

[1] H. F. W. Taylor, Cement Chemistry, Thomas Telford, 1997.

[2] E. M. Gartner, J. F. Young, D. Damidot, I. Jawed, Hydration of portland cement, in: Structure and Performance of Cements, j. bensted and p. barnes Edition, Taylor & Francis, Oxon, 2002.

[3] A. Quennoz, K. L. Scrivener, Interactions between alite and c3a-gypsum hydrations in model cements, Cement and Concrete Research 44 (2013) 46–54.

[4] K. Scrivener, The development of microstructure during the hydration of portland cement, Ph.D. thesis, University of London (1984).

[5] P. Juilland, E. Gallucci, R. Flatt, K. Scrivener, Dissolution theory applied to the induction period in alite hydration, Cement and Concrete Research 40 (6) (2010) 831–844.

[6] J. W. Bullard, H. M. Jennings, R. A. Livingston, A. Nonat, G. W. Scherer, J. S. Schweitzer, K. L. Scrivener, J. J. Thomas, Mechanisms of cement hydration, Cement and Concrete Research 41 (12) (2011) 1208–1223.

[7] J. W. Bullard, R. J. Flatt, New insights into the effect of calcium hydroxide precipitation on the kinetics of tricalcium silicate hydration, Journal of the American Ceramic Society 93 (7) (2010) 1894–1903.

[8] J. J. Thomas, J. J. Biernacki, J. W. Bullard, S. Bishnoi, J. S. Dolado, G. W. Scherer, A. Luttge, Modeling and simulation of cement hydration kinetics and microstructure development, Cement and Concrete Research 41 (12) (2011) 1257–1278.

[9] K. L. Scrivener, A. Nonat, Hydration of cementitious materials, present and future, Cement and Concrete Research 41 (7) (2011) 651–665.

[10] M. Bigaré, A. Guinier, C. Mazières, M. Regourd, N. Yannaquis, W. Eysbl, T. Hahn, E. Woermann, Polymorphism of tricalcium silicate and its solid solutions, Journal of the American Ceramic Society 50 (11) (1967) 609–619.

[11] E. Woermann, T. Hahn, W. Eysel, The substitution of alkalies in tricalcium silicate, Cement and Concrete Research 9 (6) (1979) 701–711.

Bibliography

[12] M. Courtial, M.-N. de Noirfontaine, F. Dunstetter, G. Gasecki, M. Signes-Frehel, Polymorphism of tricalcium silicate in portland cement: A fast visual identification of structure and superstructure, Powder Diffraction 18 (01) (2003) 7–15.

[13] F. Dunstetter, M.-N. de Noirfontaine, M. Courtial, Polymorphism of tricalcium silicate, the major compound of portland cement clinker: 1. structural data: review and unified analysis, Cement and Concrete Research 36 (1) (2006) 39–53.

[14] N. Golovastikov, R. Matveeva, Belov, Crystal structure of the tricalcium silicate 3caosio2 = c3s, Sovietic Physical Crystallography 20 (1975) 441–445.

[15] K. Urabe, T. Shirakami, M. Iwashima, Superstructure in a triclinic phase of tricalcium silicate, Journal of the American Ceramic Society 83 (5) (2000) 1253–1258.

[16] K. Urabe, H. Nakano, H. Morita, Structural modulations in monoclinic tricalcium silicate solid solutions doped with zinc oxide, m(i), m(II), and m(III), Journal of the American Ceramic Society 85 (2) (2002) 423–429.

[17] V. K. Peterson, A rietveld refinement investigation of a mg-stabilized triclinic tricalcium silicate using synchrotron x-ray powder diffraction data, Powder Diffraction 19 (04) (2004) 356–358.

[18] n. G. De la Torre, R. N. De Vera, A. J. Cuberos, M. A. Aranda, Crystal structure of low magnesium-content alite: Application to rietveld quantitative phase analysis, Cement and Concrete Research 38 (11) (2008) 1261–1269.

[19] I. Odler, S. Abdul-Maula, Polymorphism and hydration of tricalcium silicate doped with ZnO, Journal of the American Ceramic Society 66 (1) (1983) 1–04.

[20] G. Pellissier, S. Purdy, Stereology and quantitative metallography, American society for testing and materials, 1971.

[21] D. Stephan, S. Wistuba, Crystal structure refinement and hydration behaviour of 3cao·SiO2 solid solutions with MgO, al2o3 and fe2o3, Journal of the European Ceramic Society 26 (1–2) (2006) 141–148.

[22] D. Stephan, S. N. Dikoundou, G. Raudaschl-Sieber, Influence of combined doping of tricalcium silicate with MgO, al2o3 and fe2o3: synthesis, grindability, x-ray diffraction and 29si NMR, Materials and Structures 41 (10) (2008) 1729–1740.

[23] M.-N. De Noirfontaine, M. Courtial, F. Dunstetter, G. Gasecki, M. Signes-Frehel, Tricalcium silicate ca3sio5 superstructure analysis: A route towards the structure of the m 1 polymorph, Zeitschrift fur Kristallographie 227 (2) (2012) 102–112.

[24] F. Nishi, Y. Takeuchi, I. Maki, Tricalcium silicate ca3o[SiO4]: the monoclinic superstructure, Zeitschrift für Kristallographie 172 (1985) 297–314.

130

[25] F. Nishi, Y. Takeuchi, The rhombohedral structure of tricalcium silicate at 1200°c, Zeitschrift für Kristallographie 168 (1984) 197–212.

[26] J. Skibsted, J. Hjorth, H. J. Jakobsen, Correlation between 29si NMR chemical shifts and mean si-o bond lengths for calcium silicates, Chemical Physics Letters 172 (3–4) (1990) 279–283.

[27] J. Skibsted, H. J. Jakobsen, C. Hall, Quantification of calcium silicate phases in portland cements by 29si MAS NMR spectroscopy, Journal of the Chemical Society, Faraday Transactions 91 (24) (1995) 4423.

[28] M. Costoya Fernández, Effect of particle size on the hydration kinetics and microstructural development of tricalcium silicate, Ph.D. thesis, École polytechnique fédérale de Lausanne EPFL, Lausanne (2008).

[29] R. Snellings, A. Bazzoni, K. Scrivener, The existence of amorphous phase in portland cements: Physical factors affecting rietveld quantitative phase analysis, Cement and Concrete Research 59 (2014) 139–146.

[30] P. W. Brown, E. Franz, G. Frohnsdorff, H. Taylor, Analyses of the aqueous phase during early c3s hydration, Cement and Concrete Research 14 (2) (1984) 257–262.

[31] J. Zhang, G. W. Scherer, Comparison of methods for arresting hydration of cement, Cement and Concrete Research 41 (10) (2011) 1024–1036.

[32] J. Goldstein, D. Newbury, D. Joy, C. Lyman, P. Echlin, E. Lifshin, L. Sawyer, J. Michael, Scanning Electron Microscopy and X-ray Microanalysis: Third Edition, Springer US, 2003.

[33] D. B. Williams, C. B. Carter, Transmission Electron Microscopy: A Textbook for Materials Science, Springer, 2009.

[34] F. Company, ChemiSTEM technology a revolution in EDX analytics, Application Note ChemiSTEM Technology.

[35] A. Bazzoni, M. Cantoni, K. L. Scrivener, Impact of annealing on the early hydration of tricalcium silicate, Journal of the American Ceramic Society (2013) n/a–n/a.

[36] H. N. Stein, J. M. Stevels, Influence of silica on the hydration of 3 CaO,SiO2, Journal of Applied Chemistry 14 (8) (1964) 338–346.

[37] D. L. Kantro, S. Brunauer, C. H. Weise, Development of surface in the hydration of calcium silicates II. extension of investigation to earlier and later stages of hydration, The Journal of Physical Chemistry 66 (10) (1962) 1804–1809.

[38] D. D. Double, A. Hellawell, S. J. Perry, The hydration of portland cement, Proceedings of the Royal Society of London. A. Mathematical and Physical Sciences 359 (1699) (1978) 435 –451.

[39] J. Birchall, A. Howard, D. Double, Some general considerations of a membrane/osmosis model for portland cement hydration, Cement and Concrete Research 10 (2) (1980) 145–155.

[40] E. M. Gartner, H. M. Jennings, Thermodynamics of calcium silicate hydrates and their solutions, Journal of the American Ceramic Society 70 (10) (1987) 743–749.

[41] F. Bellmann, D. Damidot, B. Möser, J. Skibsted, Improved evidence for the existence of an intermediate phase during hydration of tricalcium silicate, Cement and Concrete Research 40 (6) (2010) 875–884.

[42] F. Bellmann, T. Sowoidnich, H.-M. Ludwig, D. Damidot, Analysis of the surface of tricalcium silicate during the induction period by x-ray photoelectron spectroscopy, Cement and Concrete Research 42 (9) (2012) 1189–1198.

[43] M. Regourd, J. Thomassin, P. Baillif, J. Touray, Study of the early hydration of ca3sio5 by x-ray photoelectron spectrometry, Cement and Concrete Research 10 (2) (1980) 223–230.

[44] S. A. Rodger, G. W. Groves, N. J. Clayden, C. M. Dobson, Hydration of tricalcium silicate followed by 29si NMR with cross-polarization, Journal of the American Ceramic Society 71 (2) (1988) 91–96.

[45] J. M. Makar, G. W. Chan, End of the induction period in ordinary portland cement as examined by high-resolution scanning electron microscopy, Journal of the American Ceramic Society 91 (4) (2008) 1292–1299.

[46] P. Barret, D. Ménétrier, Filter dissolution of c3s as a function of the lime concentration in a limited amount of lime water, Cement and Concrete Research 10 (4) (1980) 521–534.

[47] I. Odler, H. Dörr, Early hydration of tricalcium silicate i. kinetics of the hydration process and the stoichiometry of the hydration products, Cement and Concrete Research 9 (2) (1979) 239–248.

[48] M. E. Tadros, J. Skalny, R. S. Kalyoncu, Early hydration of tricalcium silicate, Journal of the American Ceramic Society 59 (7-8) (1976) 344–347.

[49] M. E. Tadros, J. Skalny, R. S. Kalyoncu, Kinetics of calcium hydroxide crystal growth from solution, Journal of Colloid and Interface Science 55 (1) (1976) 20–24.

[50] J. F. Young, H. S. Tong, R. L. Berger, Compositions of solutions in contact with hydrating tricalcium silicate pastes, Journal of the American Ceramic Society 60 (5-6) (1977) 193–198.

[51] S. Garrault, A. Nonat, Hydrated layer formation on tricalcium and dicalcium silicate surfaces: Experimental study and numerical simulations, Langmuir 17 (26) (2001) 8131–8138.

[52] S. Garrault, E. Finot, E. Lesniewska, A. Nonat, Study of c-s-h growth on c3s surface during its early hydration, Materials and Structures 38 (4) (2005) 435–442.

[53] J. Thomas, H. Jennings, J. Chen, Influence of nucleation seeding on the hydration mechanisms of tricalcium silicate and cement, Journal of Physical Chemistry C 113 (11) (2009) 4327–4334.

[54] A. C. Lasaga, A. Luttge, Variation of crystal dissolution rate based on a dissolution stepwave model, Science 291 (5512) (2001) 2400 –2404.

[55] P. M. Dove, N. Han, Kinetics of mineral dissolution and growth as reciprocal microscopic surface processes across chemical driving force, AIP Conference Proceedings 916 (1) (2007) 215–234.

[56] L. Nicoleau, A. Nonat, D. Perrey, The di- and tricalcium silicate dissolutions, Cement and Concrete Research 47 (2013) 14–30.

[57] I. Odler, J. Schüppstuhl, Early hydration of tricalcium silicate III. control of the induction period, Cement and Concrete Research 11 (5-6) (1981) 765–774.

[58] T. Sakurai, T. Sato, A. Yoshinaga, The effect of minor components on the early hydraulic activity of the major phases of portland cement clinker, Vol. 1, 1969, pp. 300–321.

[59] G. W. Groves, Portland cement clinker viewed by transmission electron microscopy, Journal of Materials Science 16 (4) (1981) 1063–1070.

[60] G. W. Groves, J. P. Skalny, L. J. Parrott, K. Kendall, T.e.m. studies of cement clinker compounds, their hydration and strong cement pastes [and discussion], Philosophical Transactions of the Royal Society of London. Series A, Mathematical and Physical Sciences 310 (1511) (1983) 79–83.

[61] K. Hudson, G. Groves, The structure of alite in portland cement clinker — TEM evidence, Cement and Concrete Research 12 (1) (1982) 61–68.

[62] E. Gartner, Discussion of the paper "dissolution theory applied to the induction period in alite hydration" by p. juilland et al., cem. concr. res. 40 (2010) 831-844, Cement and Concrete Research 41 (5) (2011) 560–562.

[63] P. Juilland, E. Gallucci, R. J. Flatt, K. L. Scrivener, Reply to the discussion by e. gartner of the paper "dissolution theory applied to the induction period in alite hydration", Cement and Concrete Research 41 (5) (2011) 563–564.

[64] J. Makar, J. Beaudoin, T. Sato, R. Alizadeh, L. Raki, Discussion of "dissolution theory applied to the induction period in alite hydration", Cement and Concrete Research 41 (5) (2011) 565–567.

[65] P. Juilland, E. Gallucci, R. J. Flatt, K. L. Scrivener, Reply to the discussion by j. makar, j.j. beaudoin, t. sato, r. alizadeh and l. raki of "dissolution theory applied to the induction period in alite hydration", Cement and Concrete Research 41 (5) (2011) 568–569.

[66] A. Lüttge, Etch pit coalescence, surface area, and overall mineral dissolution rates, American Mineralogist 90 (11-12) (2005) 1776–1783.

[67] P. Juilland, A. Kumar, E. Gallucci, R. J. Flatt, K. L. Scrivener, Effect of mixing on the early hydration of alite and OPC systems, Cement and Concrete Research 42 (9) (2012) 1175–1188.

[68] P. Juilland, Early hydration of cementitious systems, EPFL, Lausanne, 2009.

[69] R. S. Arvidson, A. Luttge, Mineral dissolution kinetics as a function of distance from equilibrium – new experimental results, Chemical Geology 269 (1–2) (2010) 79–88.

[70] J.-M. Gautier, E. H. Oelkers, J. Schott, Are quartz dissolution rates proportional to b.e.t. surface areas?, Geochimica et Cosmochimica Acta 65 (7) (2001) 1059–1070.

[71] L. Zhang, A. Lüttge, Morphological evolution of dissolving feldspar particles with anisotropic surface kinetics and implications for dissolution rate normalization and grain size dependence: A kinetic modeling study, Geochimica et Cosmochimica Acta 73 (22) (2009) 6757–6770.

[72] J. P. Hamilton, C. G. Pantano, S. L. Brantley, Dissolution of albite glass and crystal, Geochimica et Cosmochimica Acta 64 (15) (2000) 2603–2615.

[73] R. S. Arvidson, M. S. Beig, A. Luttge, Single-crystal plagioclase feldspar dissolution rates measured by vertical scanning interferometry, American Mineralogist 89 (2004) 51–56.

[74] G. R. Holdren Jr, R. A. Berner, Mechanism of feldspar weathering i. experimental studies, Geochimica et Cosmochimica Acta 43 (8) (1979) 1161–1171.

[75] J. Ferret, R. Gout, Y. Kihn, J. Sevely, The influence of grinding on the dissolution kinetics of calcite, Physics and Chemistry of Minerals 15 (2) (1987) 163–170.

[76] L. Murr, J. Hiskey, Kinetic effects of particle-size and crystal dislocation density on the dichromate leaching of chalcopyrite, Metallurgical and Materials Transactions B 12 (2) (1981) 255–267.

[77] I. N. MacInnis, S. L. Brantley, The role of dislocations and surface morphology in calcite dissolution, Geochimica et Cosmochimica Acta 56 (3) (1992) 1113–1126.

[78] K. Sangwal, S. K. Arora, The anisotropy of grinding damage, chemical polishing and etching in MgO crystals, Journal of Physics D: Applied Physics 12 (4) (1979) 645–650.

[79] R. Petrovich, Kinetics of dissolution of mechanically comminuted rock-forming oxides and silicates i. deformation and dissolution of quartz under laboratory conditions, Geochimica et Cosmochimica Acta 45 (10) (1981) 1665–1674.

[80] R. Petrovich, Kinetics of dissolution of mechanically comminuted rock-forming oxides and silicates II. deformation and dissolution of oxides and silicates in the laboratory and at the earth's surface, Geochimica et Cosmochimica Acta 45 (10) (1981) 1675–1686.

[81] D. Tromans, J. Meech, Enhanced dissolution of minerals: Microtopography and mechanical activation, Minerals Engineering 12 (6) (1999) 609–625.

[82] D. Tromans, J. Meech, Enhanced dissolution of minerals: stored energy, amorphism and mechanical activation, Minerals Engineering 14 (11) (2001) 1359–1377.

[83] D. Tromans, J. Meech, Fracture toughness and surface energies of minerals: theoretical estimates for oxides, sulphides, silicates and halides, Minerals Engineering 15 (12) (2002) 1027–1041.

[84] S. Sadrai, J. A. Meech, D. Tromans, F. Sassani, Energy efficient comminution under high velocity impact fragmentation, Minerals Engineering 24 (10) (2011) 1053–1061.

[85] A. A. Griffith, The phenomena of rupture and flow in solids, Philosophical Transactions of the Royal Society of London. Series A, Containing Papers of a Mathematical or Physical Character 221 (582-593) (1921) 163–198.

[86] K. Mori, T. Fukunaga, Y. Shiraishi, K. Iwase, Q. Xu, K. Oishi, K. Yatsuyanagi, M. Yonemura, K. Itoh, M. Sugiyama, T. Ishigaki, T. Kamiyama, M. Kawai, Structural and hydration properties of amorphous tricalcium silicate, Cement and Concrete Research 36 (11) (2006) 2033–2038.

[87] R. T. Cygan, W. H. Casey, M. B. Boslough, H. R. Westrich, M. J. Carr, G. R. Holdren Jr., Dissolution kinetics of experimentally shocked silicate minerals, Chemical Geology 78 (3-4) (1989) 229–244.

[88] P. Fierens, J. Tirlocq, J. Verhaegen, Défauts de structure et hydratation du silicate tricalcique 39 (4) (1974) 363–367.

[89] P. Fierens, Y. Kabuema, J. Tirlocq, Influence de la temperature de recuit sur la cinetique de l'hydratation du silicate tricalcique, Cement and Concrete Research 12 (4) (1982) 455–462.

[90] F. Bellmann, T. Sowoidnich, B. Möser, Formation of an intermediate phase and influence of crystallographic defects on dissolution of c3s, Madrid, 2011.

[91] R. A. Thompson, D. C. Killoh, J. A. Forrester, Crystal chemistry and reactivity of the MgO-stabilized alites, Journal of the American Ceramic Society 58 (1-2) (1975) 54–57.

[92] F. Begarin, S. Garrault, A. Nonat, L. Nicoleau, Hydration of alite containing aluminium, Advances in Applied Ceramics 110 (3) (2011) 127–130.

[93] P. Fierens, A. Verhaegen, J. Verhaegen, Microthermoluminescence, Cement and Concrete Research 4 (4) (1974) 511–518.

[94] P. Fierens, J. Verhaegen, The effect of water on pure and doped tricalcium silicate using the techniques of adsorboluminescence, Cement and Concrete Research 5 (3) (1975) 233–238.

[95] McCrone, McCrone micronizing mill, Product information.

[96] S. Amelinckx, J. Van Landuyt, Contrast effects at planar interfaces, in: Electron Microscopy in Mineralogy, h.-r. wenk Edition, Springer Verlag Berlin, Heidelberg, 1976, pp. 68–112.

[97] P. W. Brown, J. Pommersheim, G. Frohnsdorff, A kinetic model for the hydration of tricalcium silicate, Cement and Concrete Research 15 (1) (1985) 35–41.

[98] K. Velez, S. Maximilien, D. Damidot, G. Fantozzi, F. Sorrentino, Determination by nanoindentation of elastic modulus and hardness of pure constituents of portland cement clinker, Cement and Concrete Research 31 (4) (2001) 555–561.

[99] J. Schott, S. Brantley, D. Crerar, C. Guy, M. Borcsik, C. Willaime, Dissolution kinetics of strained calcite, Geochimica et Cosmochimica Acta 53 (2) (1989) 373–382.

[100] E. M. Gartner, J. M. Gaidis, Hydration Mechanisms, I in Materials science of concrete, jan skalny Edition, The American Ceramic Society, 1989.

[101] H. Jennings, Model for the microstructure of calcium silicate hydrate in cement paste, Cement and Concrete Research 30 (1) (2000) 101–116.

[102] E. M. Gartner, K. E. Kurtis, P. J. M. Monteiro, Proposed mechanism of c-s-h growth tested by soft x-ray microscopy, Cement and Concrete Research 30 (5) (2000) 817–822.

[103] E. M. Gartner, A proposed mechanism for the growth of c-s-h during the hydration of tricalcium silicate, Cement and Concrete Research 27 (5) (1997) 665–672.

[104] I. Richardson, Nature of c-s-h in hardened cements, Cement and Concrete Research 29 (8) (1999) 1131–1147.

[105] I. Richardson, The nature of the hydration products in hardened cement pastes, Cement and Concrete Composites 22 (2) (2000) 97–113.

[106] I. Richardson, Tobermorite/jennite- and tobermorite/calcium hydroxide-based models for the structure of c-s-h: applicability to hardened pastes of tricalcium silicate, b-dicalcium silicate, portland cement, and blends of portland cement with blast-furnace slag, metakaolin, or silica fume, Cement and Concrete Research 34 (9) (2004) 1733–1777.

[107] S. Bishnoi, K. L. Scrivener, Studying nucleation and growth kinetics of alite hydration using mic, Cement and Concrete Research 39 (10) (2009) 849–860.

[108] S. Garrault, T. Behr, A. Nonat, Formation of the c-s-h layer during early hydration of tricalcium silicate grains with different sizes, The Journal of Physical Chemistry B 110 (1) (2006) 270–275.

[109] W. A. Gutteridge, J. A. Dalziel, Filler cement: The effect of the secondary component on the hydration of portland cement: Part i. a fine non-hydraulic filler, Cement and Concrete Research 20 (5) (1990) 778–782.

[110] V. Ramachandran, Thermal analyses of cement components hydrated in the presence of calcium carbonate, Thermochimica Acta 127 (C) (1988) 385–394.

[111] J. Péra, S. Husson, B. Guilhot, Influence of finely ground limestone on cement hydration, Cement and Concrete Composites 21 (2) (1999) 99–105.

[112] G. Kakali, S. Tsivilis, E. Aggeli, M. Bati, Hydration products of c3a, c3s and portland cement in the presence of CaCO3, Cement and Concrete Research 30 (7) (2000) 1073–1077.

[113] J. Stark, B. Möser, F. Bellmann, Nucleation and growth of c-s-h phases on mineral admixtures, in: P. D.-I. C. U. Grosse (Ed.), Advances in Construction Materials 2007, Springer Berlin Heidelberg, 2007, pp. 531–538.

[114] T. Matschei, B. Lothenbach, F. P. Glasser, The role of calcium carbonate in cement hydration, Cement and Concrete Research 37 (4) (2007) 551–558.

[115] B. Lothenbach, G. Le Saout, E. Gallucci, K. Scrivener, Influence of limestone on the hydration of portland cements, Cement and Concrete Research 38 (6) (2008) 848–860.

[116] B. Lothenbach, T. Matschei, G. Möschner, F. P. Glasser, Thermodynamic modelling of the effect of temperature on the hydration and porosity of portland cement, Cement and Concrete Research 38 (1) (2008) 1–18.

[117] B. Lothenbach, Thermodynamic equilibrium calculations in cementitious systems, Materials and Structures 43 (10) (2010) 1413–1433.

[118] B. Lothenbach, K. Scrivener, R. Hooton, Supplementary cementitious materials, Cement and Concrete Research 41 (12) (2011) 1244–1256.

[119] I. G. Richardson, A. R. Brough, R. Brydson, G. W. Groves, C. M. Dobson, Location of aluminum in substituted calcium silicate hydrate (c-s-h) gels as determined by 29si and 27al NMR and EELS, Journal of the American Ceramic Society 76 (9) (1993) 2285–2288.

[120] P. Faucon, A. Delagrave, C. Richet, J. M. Marchand, H. Zanni, Aluminum incorporation in calcium silicate hydrates (c-s-h) depending on their ca/si ratio, The Journal of Physical Chemistry B 103 (37) (1999) 7796–7802.

[121] J. Rose, I. Moulin, A. Masion, P. M. Bertsch, M. R. Wiesner, J.-Y. Bottero, F. Mosnier, C. Haehnel, X-ray absorption spectroscopy study of immobilization processes for heavy metals in calcium silicate hydrates. 2. zinc, Langmuir 17 (12) (2001) 3658–3665.

[122] C. E. Tommaseo, M. Kersten, Aqueous solubility diagrams for cementitious waste stabilization systems. 3. mechanism of zinc immobilizaton by calcium silicate hydrate, Environmental Science & Technology 36 (13) (2002) 2919–2925.

[123] Q. Chen, C. Hills, M. Tyrer, I. Slipper, H. Shen, A. Brough, Characterisation of products of tricalcium silicate hydration in the presence of heavy metals, Journal of Hazardous Materials 147 (3) (2007) 817–825.

[124] G. Mascolo, V. Ramachandran, Hydration and strength characteristics of synthetic al-, mg- and fe alites, Materials and Structures 8 (5) (1975) 373–376.

[125] G. Valenti, V. Sabatelli, B. Marchese, Hydration kinetics of tricalcium silicate solid solutions at early ages, Cement and Concrete Research 8 (1) (1978) 61–72.

[126] R. Aldous, The hydraulic behaviour of rhombohedral alite, Cement and Concrete Research 13 (1) (1983) 89–96.

[127] H. R. Stewart, J. E. Bailey, Microstructural studies of the hydration products of three tricalcium silicate polymorphs, Journal of Materials Science 18 (12) (1983) 3686–3694.

[128] T. Stanek, P. Sulovský, The influence of the alite polymorphism on the strength of the portland cement, Cement and Concrete Research 32 (7) (2002) 1169–1175.

[129] V. K. Peterson, C. M. Brown, R. A. Livingston, Quasielastic and inelastic neutron scattering study of the hydration of monoclinic and triclinic tricalcium silicate, Chemical Physics 326 (2-3) (2006) 381–389.

[130] D. Stephan, H. Maleki, D. Knöfel, B. Eber, R. Härdtl, Influence of cr, ni, and zn on the properties of pure clinker phases: Part i. c3s, Cement and Concrete Research 29 (4) (1999) 545–552.

[131] D. Stephan, S. N. Dikoundou, G. Raudaschl-Sieber, Hydration characteristics and hydration products of tricalcium silicate doped with a combination of MgO, al2o3 and fe2o3, Thermochimica Acta 472 (1-2) (2008) 64–73.

[132] E. Gallucci, P. Mathur, K. Scrivener, Microstructural development of early age hydration shells around cement grains, Cement and Concrete Research 40 (1) (2010) 4–13.

[133] D. M. Kirby, J. J. Biernacki, The effect of water-to-cement ratio on the hydration kinetics of tricalcium silicate cements: Testing the two-step hydration hypothesis, Cement and Concrete Research 42 (8) (2012) 1147–1156.

[134] J. J. Thomas, A new approach to modeling the nucleation and growth kinetics of tricalcium silicate hydration, Journal of the American Ceramic Society 90 (10) (2007) 3282–3288.

[135] M. Avrami, Kinetics of phase change. i general theory, The Journal of Chemical Physics 7 (12) (1939) 1103–1112.

[136] M. Avrami, Kinetics of phase change. II transformation - time relations for random distribution of nuclei, The Journal of Chemical Physics 8 (2) (1940) 212–224.

[137] J. W. Cahn, The kinetics of grain boundary nucleated reactions, Acta Metallurgica 4 (5) (1956) 449–459.

[138] G. W. Scherer, J. Zhang, J. J. Thomas, Nucleation and growth models for hydration of cement, Cement and Concrete Research 42 (7) (2012) 982–993.

[139] S. Bishnoi, K. L. Scrivener, mic: A new platform for modelling the hydration of cements, Cement and Concrete Research 39 (4) (2009) 266–274.

[140] S. Bishnoi, Geometric limitations of nucleation and growth models: Revisiting the impingement assumption, Cement and Concrete Research 46 (2013) 30–40.

[141] S. Gauffinet, E. Finot, E. Lesniewska, A. Nonat, Observation directe de la croissance d'hydrosilicate de calcium sur des surfaces d'alite et de silice par microscopie a force atomique, Comptes Rendus de l'Académie des Sciences - Series IIA - Earth and Planetary Science 327 (4) (1998) 231–236.

[142] D. Damidot, A. Nonat, P. Barret, Kinetics of tricalcium silicate hydration in diluted suspensions by microcalorimetric measurements, Journal of the American Ceramic Society 73 (11) (1990) 3319–3322.

[143] D. Damidot, A. Nonat, C_3s hydration in diluted and stirred suspensions: (i) study of the two kinetic steps, Advances in Cement Research 6 (21) (1994) 27–35.

[144] P. C. Mathur, Study of cementitious materials using transmission electron microscopy, EPFL, Lausanne, 2007.

[145] E. Lachowski, S. Diamond, Investigation of the composition and morphology of individual particles of portland cement paste: 1. c-s-h gel and calcium hydroxide particles, Cement and Concrete Research 13 (2) (1983) 177–185.

[146] G. Charlot, Les réactions chimiques en solution aqueuse: et caractérisation des ions, 7th Edition, Masson, 1983.

[147] D. A. Kulik, M. Kersten, Aqueous solubility diagrams for cementitious waste stabilization systems. 4. a carbonation model for zn-doped calcium silicate hydrate by gibbs energy minimization, Environmental Science & Technology 36 (13) (2002) 2926–2931.

[148] A. Kumar, S. Bishnoi, K. L. Scrivener, Modelling early age hydration kinetics of alite, Cement and Concrete Research 42 (7) (2012) 903–918.

[149] L. C. Soare, P. Bowen, J. Lemaitre, H. Hofmann, Precipitation of nanostructured copper oxalate substructure and growth mechanism, The Journal of Physical Chemistry B 110 (36) (2006) 17763–17771.

[150] E. Berodier, Impact of additions on hydration kinetics of cementitious materials, Ph.D. thesis, Ecole Polytechnique Fédérale de Lausanne EPFL, Lausanne (2014).

[151] I. Richardson, Electron microscopy of cements, in: Structure and Performance of Cements, j. bensted and p. barnes Edition, Taylor & Francis, Oxon, 2002.

[152] R. F. Egerton, Control of radiation damage in the TEM, Ultramicroscopy 127 (2013) 100–108.

[153] I. G. Richardson, G. W. Groves, Microstructure and microanalysis of hardened ordinary portland cement pastes, Journal of Materials Science 28 (1) (1993) 265–277.

[154] C. Rössler, J. Stark, F. Steiniger, W. Tichelaar, Limited-dose electron microscopy reveals the crystallinity of fibrous c-s-h phases, Journal of the American Ceramic Society 89 (2) (2006) 627–632.

[155] I. Richardson, G. Groves, Models for the composition and structure of calcium silicate hydrate (c-s-h) gel in hardened tricalcium silicate pastes, Cement and Concrete Research 22 (6) (1992) 1001–1010.

[156] I. Richardson, J. Cabrera, The nature of c-s-h in model slag-cements, Cement and Concrete Composites 22 (4) (2000) 259–266.

[157] R. Taylor, I. G. Richardson, R. M. D. Brydson, Nature of c-s-h in 20 year old neat ordinary portland cement and 10% portland cement–90% ground granulated blast furnace slag pastes, Advances in Applied Ceramics 106 (6) (2007) 294–301.

[158] E. E. Lachowski, K. Mohan, H. F. W. Taylor, A. E. Moore, Analytical electron microscopy of cement pastes: II, pastes of portland cements and clinkers, Journal of the American Ceramic Society 63 (7-8) (1980) 447–452.

[159] D. Rayment, E. Lachowski, The analysis of OPC pastes: A comparison between analytical electron microscopy and electron probe microanalysis, Cement and Concrete Research 14 (1) (1984) 43–48.

[160] H. F. W. Taylor, K. Mohan, G. K. Moir, Analytical study of pure and extended portland cement pastes: I, pure portland cement pastes, Journal of the American Ceramic Society 68 (12) (1985) 680–685.

[161] H. F. W. Taylor, 726. hydrated calcium silicates. part i. compound formation at ordinary temperatures, Journal of the Chemical Society (Resumed) (0) (1950) 3682–3690.

[162] S. A. Greenberg, T. N. Chang, Investigation of the colloidal hydrated calcium silicates. II. solubility relationships in the calcium oxide-silica-water system at 25°, The Journal of Physical Chemistry 69 (1) (1965) 182–188.

[163] X. Cong, R. J. Kirkpatrick, 29si MAS NMR study of the structure of calcium silicate hydrate, Advanced Cement Based Materials 3 (3–4) (1996) 144–156.

[164] J. J. Chen, J. J. Thomas, H. F. Taylor, H. M. Jennings, Solubility and structure of calcium silicate hydrate, Cement and Concrete Research 34 (9) (2004) 1499–1519.

[165] E. Bonaccorsi, S. Merlino, A. R. Kampf, The crystal structure of tobermorite 14 Å (plombierite), a c-s-h phase, Journal of the American Ceramic Society 88 (3) (2005) 505–512.

[166] E. Bonaccorsi, S. Merlino, H. Taylor, The crystal structure of jennite, ca9si6o18(OH)6·8h2o, Cement and Concrete Research 34 (9) (2004) 1481–1488.

[167] I. Richardson, The calcium silicate hydrates, Cement and Concrete Research 38 (2) (2008) 137–158.

[168] H. F. Taylor, Proposed structure for calcium silicate hydrate gel, Journal of the American Ceramic Society 69 (6) (1986) 464–467.

[169] A. Nonat, X. Lecoq, The structure, Stoichiometry and Properties of C-S-H Prepared by C3S Hydration under Cntrolled Condition in: Nuclear magnetic resonance spectroscopy of cement-based materials, pierre colombet Edition, Springer, Berlin etc, 1998.

[170] S. Grangeon, F. Claret, Y. Linard, C. Chiaberge, X-ray diffraction: a powerful tool to probe and understand the structure of nanocrystalline calcium silicate hydrates, Acta Crystallographica Section B Structural Science Crystal Engineering and Materials 69 (5) (2013) 465–473.

[171] K. Garbev, G. Beuchle, M. Bornefeld, L. Black, P. Stemmermann, Cell dimensions and composition of nanocrystalline calcium silicate hydrate solid solutions. part 1: Synchrotron-based x-ray diffraction, Journal of the American Ceramic Society 91 (9) (2008) 3005–3014.

[172] K. Garbev, M. Bornefeld, G. Beuchle, P. Stemmermann, Cell dimensions and composition of nanocrystalline calcium silicate hydrate solid solutions. part 2: X-ray and thermogravimetry study, Journal of the American Ceramic Society 91 (9) (2008) 3015–3023.

[173] G. W. Groves, A. Brough, I. G. Richardson, C. M. Dobson, Progressive changes in the structure of hardened c3s cement pastes due to carbonation, Journal of the American Ceramic Society 74 (11) (1991) 2891–2896.

[174] I. Richardson, G. Groves, A. Brough, C. Dobson, The carbonation of OPC and OPC/silica fume hardened cement pastes in air under conditions of fixed humidity, Advances in Cement Research 5 (18) (1993) 81–86.

[175] H. Stade, W. Wieker, Zum aufbau schlecht geordneter calciumhydrogensilicate. i. bildung und eigenschaften einer schlecht geordneten calciumhydrogendisilicatphase, Zeitschrift für anorganische und allgemeine Chemie 466 (1) (1980) 55–70.

[176] B. Tomazic, R. Mohanty, M. Tadros, J. Estrin, Crystallization of calcium hydroxide from aqueous solution: I. preliminary study, Journal of Crystal Growth 75 (2) (1986) 329–338.

[177] B. Tomazic, R. Mohanty, M. Tadros, J. Estrin, Crystallization of calcium hydroxide from aqueous solution: II. observations of growth, morphology and secondary nucleation, Journal of Crystal Growth 75 (2) (1986) 339–347.

[178] R. Hedin, S. f. f. c. o. betong, Processes of Diffusion, Solution, and Crystallisation in System Ca(OH)2-H2O., Royal Institute of Technology, 1962.

[179] S. Galmarini, A. Aimable, N. Ruffray, P. Bowen, Changes in portlandite morphology with solvent composition: Atomistic simulations and experiment, Cement and Concrete Research 41 (12) (2011) 1330–1338.

[180] K. O. Kjellsen, H. Justnes, Revisiting the microstructure of hydrated tricalcium silicate, a comparison to portland cement, Cement and Concrete Composites 26 (8) (2004) 947–956.

[181] E. Gallucci, K. Scrivener, Crystallisation of calcium hydroxide in early age model and ordinary cementitious systems, Cement and Concrete Research 37 (4) (2007) 492–501.

[182] T. Xie, J. J. Biernacki, Growth of calcium hydroxide islands in tricalcium silicate-based cements at early age, Journal of the American Ceramic Society 95 (9) (2012) 2808–2819.

[183] R. L. Berger, J. D. McGregor, Effect of temperature and water-solid ratio on growth of ca(OH)2 crystals formed during hydration of ca3sio5, Journal of the American Ceramic Society 56 (2) (1973) 73–79.

[184] M. Zajac, A. Rossberg, G. Le Saout, B. Lothenbach, Influence of limestone and anhydrite on the hydration of portland cements, Cement and Concrete Composites 46 (2014) 99–108.

[185] A. C. A. Muller, K. L. Scrivener, A. M. Gajewicz, P. J. McDonald, Densification of c–s–h measured by 1h NMR relaxometry, The Journal of Physical Chemistry C 117 (1) (2013) 403–412.

[186] K. L. Scrivener, Backscattered electron imaging of cementitious microstructures: understanding and quantification, Cement and Concrete Composites 26 (8) (2004) 935–945.

[187] P. Barret, D. Bertrandie, Importance of the liquid to solid weight ratio in the powdered solid-liquid reactions: Example drawn from cement constituent hydration, Solid State Ionics 101-103 (PART 1) (1997) 359–365.

[188] G. Sant, B. Lothenbach, P. Juilland, G. Le Saout, J. Weiss, K. Scrivener, The origin of early age expansions induced in cementitious materials containing shrinkage reducing admixtures, Cement and Concrete Research 41 (3) (2011) 218–229.

Personal details

Amelie BAZZONI
Grammont 7
1007 Lausanne
Mobile: +41 (0)79 722 81 59
E-mail: amelie.bazzoni@gmail.com
Date of Birth 11.08.1987
Single
Swiss

Education

2010-2014	PhD in Materials Science and Engineering, Swiss federal institute of technology (EPFL)
2009	Minor in Management of Technology and Entrepreneurship (EPFL)
2008-2010	Master in Materials Science and Engineering (EPFL), Structural materials for use in transport, energy and infrastructure
2005-2008	Bachelor in Materials Science and Engineering (EPFL)

Work experience

2010-2014	**Research assistant laboratory of construction materials (LMC, EPFL) and interdisciplinary center for microscopy (CIME, EPFL)**
	Collaboration with a Chinese Post-doctorate from Nanjing Institute of Technology
	Supervision of semester project, practical work and training for microscopes
	Technical competencies
	Scanning electron microscopy (SEM), energy dispersive analysis (EDS)
	Transmission electron microscopy (TEM)
	Scanning transmission electron microscopy, energy dispersive analysis (STEM- EDS)
	Focus ion beam (FIB)
	X-Ray diffraction (XRD) phases analysis by Rietveld
2009-2010	**Laboratoire Dubois SA, La Chaux-de-Fonds (CH)**
	Evaluation of an atomic force microscope (AFM)
	Set up of a nano-indentation device

Other experiences

2004-2013	ParaBole festival (music festival of around 1500 people) - Bole (NE)
	Promotion and sponsoring co-responsible, Human resources responsible
2013	Diving, PADI Advanced Open water

Languages

French	Native language
German	Intermediate knowledge
English	Good knowledge

Bibliography

Publications

Reviewed Journal papers

Amélie Bazzoni, Marco Cantoni and Karen L. Scrivener, "Impact of Annealing on the Early Hydration of Tricalcium Silicate", Journal of the American Ceramic Society, 97 [2] 584–591 (2014)

R. Snellings, A. Bazzoni, and K. Scrivener, "The existence of amorphous phase in Portland cements: Physical factors affecting Rietveld quantitative phase analysis", Cement and Concrete Research, 59 139-46 (2014)

Amélie Bazzoni, Suhua Ma, Qianqian Wang, Xiadong Shen, Marco Cantoni and Karen L. Scrivener, " The effect of Magnesium and Zinc ions on the hydration kinetics of C_3S", Journal of the American Ceramic Society, accepted

Non-refereed conference papers with talk

Amélie Bazzoni, Marco Cantoni and Karen L. Scrivener, "Early Hydration of Tricalcium Silicate", 31st Cement and Concrete Science Conference, Imperial College London, United Kingdom, 12-13 September 2011

Amélie Bazzoni, Marco Cantoni and Karen L. Scrivener, "Impact of thermal treatment on the Early Hydration of Tricalcium Silicate", 14th Euroseminar on Microscopy Applied to Building Materials, Helsingør Denmark, 10-14 June 2013

Amélie Bazzoni, Marco Cantoni and Karen L. Scrivener, "The effect of water to cement ration on the C-S-H composition and morphology", Workshop Calcium-silicate hydrates containing aluminium: C-A-S-H, Empa Dübendorf Switzerland, 5.-6. May 2014